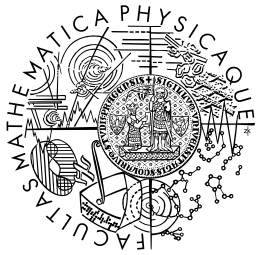

FACULTY
OF MATHEMATICS
AND PHYSICS
Charles University

DOCTORAL THESIS

Štěpán Timr

Molecules in Cell Membranes

Institute of Organic Chemistry and Biochemistry
Czech Academy of Sciences

Advisor of the doctoral thesis:	prof. Mgr. Pavel Jungwirth, CSc., DSc.
Study programme:	Physics
Study branch:	Biophysics, Chemical and Macromolecular Physics

Prague 2017

I declare that I carried out this doctoral thesis independently, and only with the cited sources, literature and other professional sources.

I understand that my work relates to the rights and obligations under the Act No. 121/2000 Sb., the Copyright Act, as amended, in particular the fact that the Charles University has the right to conclude a license agreement on the use of this work as a school work pursuant to Section 60 subsection 1 of the Copyright Act.

In Prague, 30. 6. 2017 signature of the author

Název práce: Molekuly v buněčných membránách

Autor: Mgr. Štěpán Timr

Ústav: Ústav organické chemie a biochemie Akademie věd České republiky

Vedoucí disertační práce: prof. Mgr. Pavel Jungwirth, CSc., DSc.

Abstrakt: Biologické membrány se aktivně účastní řady procesů v živých buňkách, a detailní popis jejich struktury, dynamiky a funkce je tudíž nezbytný pro porozumění živým organismům na molekulární úrovni. V této práci jsme využili vysoké časové a prostorové rozlišení poskytované počítačovými simulacemi pro výzkum chování několika druhů molekul, které se mohou vázat do membrán buněk. Kombinace klasických simulací molekulové dynamiky a *ab initio* výpočtů elektronové struktury nám dovolila charakterizovat optické vlastnosti fluorescenčních sond zanořených v membránách, a tím přispět k rozvoji dvoufotonové polarizační mikroskopie jako nástroje strukturní biologie. Simulace molekulové dynamiky nám dále umožnily popsat na atomární úrovni vratnou vazbu rekoverinu k membráně a rovněž poskytly významný vhled do mechanismu vápníkem indukovaného myristoylového přepínače tohoto proteinu, důležitého pro adaptaci zrakových buněk. Kromě toho jsme zkoumali biologickou úlohu oxidace cholesterolu a porovnali dvě metody popisu membránového napětí v simulacích molekulové dynamiky.

Klíčová slova: biologické membrány, molekulová dynamika, fluorescenční sondy, rekoverin, myristoylový přepínač.

Title: Molecules in Cell Membranes

Author: Mgr. Štěpán Timr

Institute: Institute of Organic Chemistry and Biochemistry of the Czech Academy of Sciences

Advisor: prof. Mgr. Pavel Jungwirth, CSc., DSc.

Abstract: Biological membranes are actively involved in a multitude of processes in living cells; therefore, a detailed characterization of their structure, dynamics, and function is essential for an understanding of living organisms at the molecular level. In this work, we made use of the high spatial and temporal resolution offered by computer simulations to investigate the behavior of several molecular species which associate with cellular membranes. Using a combination of classical molecular dynamics simulations and *ab initio* electronic structure calculations, we were able to characterize nonlinear optical properties of membrane-embedded fluorescent probes and thus contribute to establishing two-photon polarization microscopy as a tool of structural biology. Moreover, our molecular dynamics simulations provided an atomistic picture of the reversible membrane binding of recoverin, a neuronal calcium-sensing protein involved in vision adaptation, and they also yielded an important insight into the mechanism of its calcium-induced myristoyl switch. In addition, we examined the biological role of cholesterol oxidation and compared two methods of representing transmembrane voltage in molecular dynamics simulations.

Keywords: biological membranes, molecular dynamics, fluorescent probes, recoverin, myristoyl switch.

Acknowledgment

I thank my Ph.D. advisor Pavel Jungwirth for the amazing years that I have been able to spend in his research group, for all his guidance, support, and inspiration. I am grateful to Josef Lazar for allowing me as an undergraduate summer-school student trained in mathematical physics to join the adventure of live cell microscopy in his lab. This exciting experience and our subsequent long-term collaboration motivated my interest in biomembranes and eventually resulted in this thesis. I also thank Roman Pleskot for being my inspiring mentor and a rich source of information on molecular biology and protein modeling. I express my gratitude to Phil Mason for introducing me "hands-on" to neutron-scattering measurements. My sincere thanks go to my collaborators Jan Kadlec, Alexey Bondar, Jiří Brabec, Josef Melcr, Daniel Bonhenry, Miriam Kohagen, Aniket Magarkar, Topi Karilainen, Elise Duboué-Dijon, and Tomáš Martinek, as well as to all members of the Jungwirth group for all their help and for creating such a friendly work environment. I greatly appreciate stimulating discussions with Pavel Srb and Samuli Ollila on the comparison of simulation results with NMR data, and I thank Arnošt Mládek for providing helpful tips on the formatting of this thesis.

I am grateful to my parents for their constant support and encouragement throughout the years of my studies. Finally, I owe a deep debt of gratitude to my wife Luisa for her care, support, and understanding, especially during the last several months before my finishing of this dissertation.

Contents

Chapter 1

Introduction

Biological membranes form an essential part of every living cell. In fact, it is likely that already the earliest living organisms more than 3.5 billion years ago featured a selectively permeable envelope (Schrum et al., 2010). The primary constituents of such an envelope were amphipathic lipids, that is, molecules containing a hydrophilic and a hydrophobic part. These lipids spontaneously assembled into a bilayer which provided the primitive cell with necessary shielding from the external environment and defined a volume in which life-sustaining chemical reactions could occur. Modern biological membranes comprise many different lipid species, belonging to three main classes: phospholipids, glycolipids, and steroids. The lipid composition influences the physical properties of biological membranes, such as their fluidity, bending rigidity, or the electrostatic potential in their vicinity. In today's organisms, membranes continue to protect the cell from external factors and also serve to organize the cell interior into numerous compartments.

While the protective and volume-organizing roles of membranes have immense importance, biological membranes are not merely walls delineating the cell and its different parts. The diverse lipid species found in membranes form a lipid "sea" which is home to numerous membrane proteins with various functions (Singer and Nicolson, 1972). Some of them serve as transporters or channels, moving molecules and ions to/from the cell or between individual intracellular compartments, thereby giving rise to concentration gradients and transmembrane voltage. Other membrane proteins are receptors responsible for the communication of the cell with its surroundings. Yet others anchor the cell membrane to the cytoskeleton, helping to maintain the overall shape of the cell. Apart from integral membrane proteins, which reside permanently in the membrane, many other proteins become membrane-attached only transiently. These peripheral membrane proteins include members of numerous regulatory and cell signaling pathways. Altogether, proteins account for 20–75 % of the mass of biological membranes,

with more than half of all proteins undergoing some sort of association with a membrane (Stillwell, 2016). By restricting diffusion to two dimensions, membranes increase the chance that two membrane-bound proteins interact, leading to more efficient signal transduction and enhanced rates of enzymatic reactions (Adam and Delbruck, 1968; Schmick and Bastiaens, 2014). As a result, membranes are involved in almost all biological processes (Stillwell, 2016).

With the characteristic length scales ranging from ångströms to micrometers and the typical time scales between picoseconds and milliseconds, probing membrane-related processes presents a formidable challenge for experiments. A number of experimental methods with different spatial and temporal resolutions have been applied to study biological membranes. These methods include X-ray crystallography, cryo-electron microscopy, neutron scattering, nuclear magnetic resonance (NMR), electron paramagnetic resonance (EPR), atomic-force microscopy (AFM), as well as various methods employing fluorescent probes and labels, such as super-resolution microscopy techniques (Stone et al., 2017) or two-photon polarization microscopy (2PPM) (Lazar et al., 2011). While the ultimate goal is to obtain a complete *in vivo* picture of cellular membranes and processes associated with them, the enormous complexity of these systems often demands the use of simplified experimental models, including lipid monolayers, supported lipid bilayers, or liposomes of various sizes.

The high spatial and temporal resolution required for investigating biological membranes can be achieved in computer simulations, which employ a numerical model of the membrane and its environment to gain information on the structure and dynamics of the system. In this way, atomistic and coarse-grained classical molecular dynamics (MD) simulations can provide detailed insights into numerous biologically relevant processes and allow for addressing questions such as how interaction with different lipids affects the function of various membrane proteins. Moreover, *ab initio* quantum mechanical (QM) calculations coupled with a classical molecular mechanics description can be used to study chemical reactions and optical processes taking place in the membrane environment.

The focus of this work lies in molecular simulation of lipid membranes and membrane-associated molecules. In particular, the thesis makes contributions in two main areas: (1) modeling of nonlinear absorption properties of membrane fluorescent probes with the goal to achieve structural interpretation of 2PPM experiments, and (2) understanding the mechanism of reversible membrane binding of recoverin, which is a calcium-sensing protein that participates in a signaling pathway responsible for vision adaption. In addition, the work contributes to (3) characterization of the biological role of cholesterol oxidation and to (4) an accu-

rate representation of transmembrane voltage in MD simulations. The processes investigated in this thesis span time scales ranging from femtoseconds, as in the case of nonlinear light absorption, to microseconds or even milliseconds, as is the case of the conformational transitions of recoverin. To describe such vastly different time scales, we employ a wide range of computational methods. These include classical atomistic MD simulations, often coupled with various enhanced-sampling techniques, coarse-grained MD simulations, as well as the time-dependent density functional theory. Taken together, the results demonstrate that molecular simulations represent a powerful tool to guide the interpretation of experimental measurements as well as to complement experiments if the time- or length scales of a process cannot be directly accessed experimentally.

The thesis is organized as follows: In the chapter immediately following this introduction, we discuss computational models of biological membranes and the simulation methods employed in this work. The subsequent chapters then introduce in detail the topics (1) to (4) and present results that we have achieved using our computational tools.

Chapter 2

Modeling of membrane systems

This chapter describes computational techniques used to model lipid membranes and molecules associated with them. After briefly mentioning simplified models of a lipid bilayer, we introduce the MD method and discuss various aspects of its use in the context of membrane systems, focusing primarily on topics that are directly relevant to this work.

2.1 Simplified models of a lipid bilayer

The various models developed to represent a lipid bilayer differ greatly in their complexity. Probably the simplest one is an infinite planar dielectric slab of low permittivity ($\epsilon_\mathrm{r} \approx 2$) surrounded by a high-permittivity medium ($\epsilon_\mathrm{r} \approx 80$). The low-permittivity region corresponds to the hydrophobic environment formed by the lipid tails while the high-permittivity region represents the surrounding aqueous solution. Within such a model, the generalized Born method can be used to estimate the electrostatic free energy ΔG_el of transferring a solute molecule from water to the membrane (Im et al., 2003). The non-electrostatic contribution ΔG_np to the free energy of transfer is commonly calculated from the change ΔA_i of the solvent accessible surface area for each atom of the solute and from experimentally derived scaling coefficients σ_i:

$$\Delta G_\mathrm{np} = \sum_i \sigma_i \, \Delta A_i \tag{2.1}$$

where the sum runs over all atoms of the solute. More sophisticated variants extend the simple dielectric slab model by adding a layer of a continuously changing permitivity from 80 to 2, which corresponds to the polar region of lipid head groups (Mori et al., 2016).

If salt effects are to be included and/or if the lipid bilayer comprises charged

lipids, estimates of ΔG_{el} may be obtained by solving the Poisson–Boltzmann equation. This equation links the electrostatic potential $\varphi(\boldsymbol{r})$ to the charge distribution $\rho^f(\boldsymbol{r})$ of the solute molecule and of the lipid bilayer. The charges of both the solute and the membrane are considered as immobile while the ions in the solvent are described implicitly and subject to thermal motion. For a monovalent salt solution with a concentration equal to c_{b}, the Poisson–Boltzmann equation has the following shape:

$$\nabla \cdot (\epsilon(\boldsymbol{r}) \nabla \varphi(\boldsymbol{r})) = 2ec_{\mathrm{b}} \sinh\left(\frac{e\varphi(\boldsymbol{r})}{k_{\mathrm{B}}T}\right) - \rho^f(\boldsymbol{r}) \tag{2.2}$$

Here $\epsilon(\boldsymbol{r})$ is the permittivity at a point $\boldsymbol{r}$, e stands for the elementary charge, k_{B} denotes the Boltzmann constant, and T is the temperature. The electrostatic potential $\varphi(\boldsymbol{r})$ obtained by solving (2.2) can be used to calculate the electrostatic free energy following Murray et al. (1990):

$$G_{\mathrm{el}} = \int \left(\rho^f \varphi - k_{\mathrm{B}}Tc_{\mathrm{b}}\left[2\cosh\left(\frac{e\varphi}{k_{\mathrm{B}}T}\right) - 2\right] - \frac{\epsilon|\nabla\varphi|^2}{2}\right) \mathrm{d}V \tag{2.3}$$

where the integral runs over all space. The electrostatic free energy corresponding to the interaction with the membrane can then be calculated as the difference of electrostatic free energies when the solute molecule is near the membrane and when it is far apart:

$$\Delta G_{\mathrm{el}} = G_{\mathrm{el}}(\text{solute} + \text{membrane}) - (G_{\mathrm{el}}(\text{solute}) + G_{\mathrm{el}}(\text{membrane})) \tag{2.4}$$

A linearized version of the Poisson–Boltzmann equation together with the description of the membrane charge as being smeared uniformly over a planar membrane surface results in the classical Guoy–Chapman theory (McLaughlin, 1989). A more recent approach solves directly the nonlinear Poisson–Boltzmann equation (2.2) and utilizes atomistic models of the membrane lipids (Murray et al., 2002). This approach has been used to characterize ΔG_{el} for membrane association of various peripheral membrane proteins and charged peptides, successfully reproducing experimental trends in their binding affinities upon varying the concentration of ions or charges on both the protein and the membrane (Murray et al., 1997, 2002). Unfortunately, the solution of the non-linear Poisson–Boltzmann equation becomes computationally very demanding for larger systems. Moreover, when the protein and the membrane are in close proximity and desolvation effects start to play a role, the obtained free energy values tend to become sensitive to the definition of the molecular surface and also cannot account for specific interactions of

the ions with the protein and the membrane (Ren et al., 2012). Importantly, this approach only provides a static picture of the membrane–protein interaction, as the geometries of both the protein and the membrane are fixed in the calculation.

2.2 Molecular dynamics

In contrast to the modeling approaches outlined in the previous section, the MD method has the capability to provide both a dynamic and atomistically-resolved picture of a lipid bilayer. Classical atomistic MD simulates motions of molecules by numerically solving Newton's equations of motion for each atom of the system. The atoms move on an empirical potential energy surface which is a sum of bonded and non-bonded terms, corresponding to different types of inter-atomic interaction. Most biomolecular MD simulations do not explicitly include electronic polarizability effects; a typical form of the potential energy function then reads

$$\begin{aligned} U = &\sum_{\text{bonds}} U_{\text{bond}}(r_{ij}) + \sum_{\text{angles}} U_{\text{ang}}(\theta_{ijk}) + \sum_{\text{dihedrals}} U_{\text{dih}}(\phi_{ijkl}) + \\ &+ \sum_{i,j} U_{\text{elstat}}(r_{ij}) + \sum_{i,j} U_{\text{vdW}}(r_{ij}) + U_{\text{restraint}} \end{aligned} \tag{2.5}$$

The first three terms describe bonded interactions, namely covalent-bond stretching, angle bending, and proper and improper dihedral torsions. Bond stretching is commonly modeled with a harmonic potential

$$U_{\text{bond}}(r_{ij}) = \frac{1}{2} k_{ij} (r_{ij} - r_{ij}^{(0)})^2 \tag{2.6}$$

A harmonic potential is also employed to describe angle bending

$$U_{\text{ang}}(\theta_{ijk}) = \frac{1}{2} k_{ijk} (\theta_{ijk} - \theta_{ijk}^{(0)})^2 \tag{2.7}$$

and it is sometimes complemented by the harmonic Urey–Bradley potential between the atoms i and k on the opposite sides of the angle. Proper dihedral torsions are typically parameterized by several terms of a cosine potential

$$U_{\text{dih}}(\phi_{ijkl}) = \sum_{n} k_{ijkl}^{(n)} (1 + \cos(n\phi_{ijkl} - \phi_{ijkl}^{(n)})) \tag{2.8}$$

or, alternatively, by the Ryckaert–Bellemans function

$$U_{\text{dih}}(\phi_{ijkl}) = \sum_{n=0}^{5} C_{ijkl}^{(n)} (\cos(\phi_{ijkl} - \phi_{ijkl}^{(n)}))^n \tag{2.9}$$

Improper dihedral potentials, which serve to maintain planarity of (typically aromatic) groups of atoms, are mostly used in the form of a harmonic potential or the cosine potential (2.8). The following two terms in 2.5 are non-bonded ones, which include the electrostatic interaction, represented by the Coulomb potential

$$U_{\mathrm{elstat}}(r_{ij}) = \frac{1}{4\pi\epsilon_0\epsilon_r}\frac{q_i q_j}{r_{ij}} \tag{2.10}$$

and the van der Waals interaction, modeled typically using the Lennard-Jones potential

$$U_{\mathrm{vdW}}(r_{ij}) = \left(\frac{C_{12}^{(ij)}}{r_{ij}}\right)^{12} - \left(\frac{C_{6}^{(ij)}}{r_{ij}}\right)^{6} \tag{2.11}$$

Finally, various restraint potentials can be used to restrain positions, angles, dihedrals, and distances of atoms or groups of atoms. The functional forms of all the potential energy terms together with the corresponding parameters constitute a force field. At each time step, i.e., typically every 1–2 fs, instantaneous forces are calculated from the gradients of the potential energy, and updated positions of each atom are evaluated using algorithms such as the Verlet propagator (Verlet, 1967) or the leap-frog propagator (Hockney et al., 1974). Temperature and pressure coupling algorithms, such as the Berendsen algorithm (Berendsen et al., 1984) or extended-ensemble algorithms (Hoover, 1985; Parrinello and Rahman, 1981), allow for sampling of a chosen statistical ensemble, e.g., the isothermal (NVT) or isothermal–isobaric (NpT) ensembles, during a simulation. Since the introduction of the MD method in the late 1950's (Alder and Wainwright, 1957, 1959), a lot of effort went into the development of algorithms ensuring numerical accuracy and computational efficiency of the MD method, and their technical details have been extensively reviewed in the literature (Allen and Tildesley, 1989; Frenkel and Smith, 2002; Rapaport, 2004). Nowadays, classical MD simulations find plentiful applications in very diverse areas ranging from materials science to computational biology (Frenkel and Smith, 2002; Rapaport, 2004).

When MD is applied to studies of biological membranes, the simulation system typically comprises a membrane patch placed in a prismatic box (see Fig. 2.1), optionally together with a protein or other molecules of interest. The rest of the box is filled with water molecules and ions mimicking the ionic composition of the intracellular or extracellular fluids. The system is replicated in all three dimensions, and periodic boundary conditions are used to treat molecules crossing the boundaries of the simulation box. Long-range electrostatic interactions, including those originating from all periodic replicas of the system, are calculated using the particle–mesh Ewald summation (Darden et al., 1993). When simula-

tions are performed in the NpT ensemble, a semi-isotropic pressure coupling is typically employed, controlling the system pressure independently in the plane of the bilayer (xy-plane) and in the perpendicular direction (z-axis). The pressure coupling results in fluctuating dimensions of the unit cell.

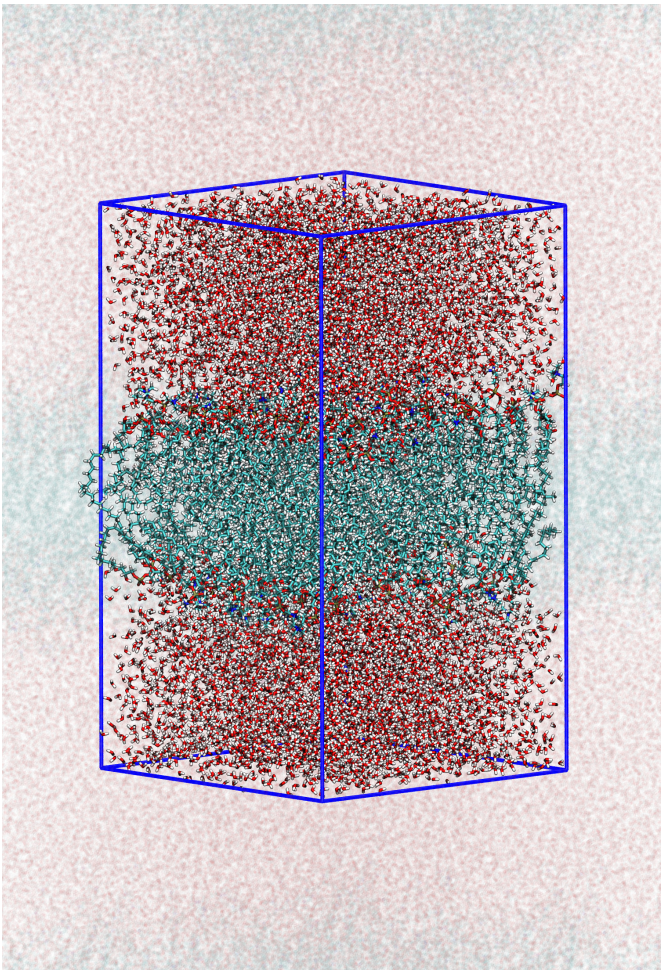

Figure 2.1: A MD simulation of a biological membrane: Example of a unit cell (6.5 × 6.5 × 11 nm) containing a phospholipid bilayer formed by 128 lipids hydrated by ~10,000 water molecules. The box is replicated in all three dimensions using three-dimensional periodic boundary conditions. Color coding: cyan, carbon; red, oxygen; white, hydrogen; blue, nitrogen; and tan, phosphorus.

2.3 Challenges of atomistic MD

Classical MD simulations of biomolecular systems face two major challenges: developing accurate force fields and reaching trajectory lengths sufficient for describing biologically important processes such as conformational transitions in proteins or their association with biological membranes. Regarding force field development, initial sets of parameters, typically obtained from experimental measurements and

ab initio quantum chemistry calculations on small molecules, are further refined to reproduce various structural or thermodynamic observables. These include, e.g., NMR order parameters, electron densitites from X-ray crystallography, and area per lipid from scattering experiments. Currently, there are several major families of biolomolecular force fields, such as AMBER (Lindorff-Larsen et al., 2010), CHARMM (Klauda et al., 2010), GROMOS (Oostenbrink et al., 2004), or OPLS (Kaminski and Friesner, 2001), all possessing modules developed specifically for the description of proteins and lipid membranes. Collaborative efforts such as the NMRlipids project (Botan et al., 2015) have been established to benchmark the performance of different force fields, leading to refinements thereof.

The time scales accessible to atomistic MD have been greatly expanded by the exponentially increasing computer performance in recent decades, allowing to routinely achieve µs trajectory lengths for many systems. In addition, techniques employing constraints (Hess et al., 1997), virtual sites, or an increased mass of hydrogen atoms (Feenstra et al., 1999) have been devised to increase the time step of MD simulations, thus pushing the accessible trajectory lengths even further. Still, in many cases, sampling of all relevant states of a biomolecular system poses a formidable challenge to present-day MD simulations. This is because typical biomolecular systems, such as lipid membranes and proteins, contain an enormous number of degrees of freedom, some of which may be associated with significant barriers in potential energy. As a result, the diffusion of a biomolecular system through its configuration space can be extremely slow so that all relevant states cannot be visited at the typical time scale of a MD simulation. Processes for which such sampling difficulties are often encountered include lipid diffusion and domain formation in heterogeneous lipid bilayers (Huang and Garcia, 2014), membrane insertion and permeation of various molecules (Neale et al., 2013), or large-scale conformational transitions in both soluble and membrane-associated proteins (Moradi and Tajkhorshid, 2014).

In general, there are two distinct strategies to overcome the sampling limitations of atomistic MD. The first of these strategies, coarse-graining, reduces the number of degrees of freedom in a simulation by treating predefined groups of atoms collectively as a single particle. To further decrease the number of degrees of freedom, water molecules and lipids are sometimes modeled implicitly as a continuum (Mori et al., 2016), in line with approaches mentioned in Section 2.1. Not only does the overall reduction of the number of particles lower the computational cost of a simulation, but discarding fast degrees of freedom due to motions of individual atoms also permits the use of significantly longer time steps, exceeding those regularly employed in atomistic MD by about an order

of magnitude. However, the coarse-graining approach may come at the cost of losing a substantial part of the atomistic detail. Coarse-grained force fields for membranes and proteins are discussed in Section 2.4. The second strategy relies on enhanced-sampling algorithms used together with atomistic MD. These algorithms seek to faster overcome potential-energy barriers and thus sample the configurational space more efficiently than direct MD simulations. To reach this goal, these methods typically utilize artificial biasing potentials, potential energy rescaling, or additional simulations performed at an elevated temperature or with modified Hamiltonians. Popular enhanced-sampling techniques include umbrella sampling (Roux, 1995), replica exchange (Sugita and Okamoto, 1999), metadynamics (Barducci et al., 2011), and accelerated MD (Markwick and McCammon, 2011). The first two of these techniques are described in more detail in Sections 2.5 and 2.6.

2.4 Coarse-grain models of lipids and proteins

Compared to an atomistic description, coarse-grained models sacrifice a certain level of molecular accuracy for improved computational efficiency. The level of coarse-graining varies between models, ranging from united-atom force fields, which treat hydrogen and carbon atoms in methyl and methylene groups together as a single particle (Chandrasekhar et al., 2003; Berger et al., 1997), to models describing the whole protein as a simple geometric object, such as a sphere or a cylinder (Kabelka and Vacha, 2016).

There are multiple approaches to construct and parameterize a coarse-grained force field. Some force fields adopt a *top-down* approach, matching the force-field parameters to global thermodynamic quantities, while others follow a *bottom-up* strategy, deriving force-field parameters from atomistic MD trajectories. A third class of approaches, often used for proteins, constructs potential-energy functions based on large sets of native structures deposited in databases such as the Protein Data Bank (RCSB PDB Database; Berman et al., 2000). On the other hand, methods exist that allow converting a coarse-grained model into a corresponding atomistic model (Wassenaar et al., 2014).

Coarse-grained models available for lipids include MARTINI (Marrink et al., 2007), SDK (Shinoda et al., 2010) ELBA (Orsi and Essex, 2011), the Highly Coarse-Grained (HCG) model (Srivastava and Voth, 2013, 2014), and others (Ingólfsson et al., 2014; Cascella and Vanni, 2015). Even more coarse-grained force fields have been developed for proteins and detailed reviews thereof are available in the literature (Noid, 2013; Ingólfsson et al., 2014). To name a few examples,

well-established coarse-grained protein force fields include MARTINI (Monticelli et al., 2008; de Jong et al., 2013), OPEP (Sterpone et al., 2014), UNRES (Krupa et al., 2013), SIRAH (Darré et al., 2015), or the Multiscale Coarse-Graining (MS-CG) approach (Zhou et al., 2007).

For applications to systems comprising both membranes and proteins, it is essential that the coarse-grained lipid model is compatible with the protein model. This is one of the reasons for the popularity of the MARTINI force field, which provides parameters both for a number of lipid species as well as for all standard amino acid residues. In general, the MARTINI model uses one bead to represent roughly four heavy atoms. The beads can differ in their Lennard-Jones parameters, and some of them carry a positive or a negative unit charge. For example, phosphatidylcholine lipids in MARTINI comprise four beads describing the polar head group, including one positively- and one negatively charged bead, and their alkyl chains contain one non-charged bead for each four to five carbon atoms. For amino-acid residues in proteins, MARTINI uses a single bead to represent all backbone atoms and zero to four beads to describe the side chain. Owing to its low-resolution description of the protein backbone, MARTINI is not suitable for modeling of processes such as protein folding (Ingólfsson et al., 2014). To keep a protein structure in its native state and to prevent undesired changes in protein conformation during a MARTINI simulation, the MARTINI force field can be complemented with an elastic network (Periole et al., 2009), which is a set of harmonic bonds interconnecting backbone beads. As for water, MARTINI employs a single bead to collectively describe four water molecules. In the most widely used standard MARTINI implementation, water particles carry no dipole moment, and polarization effects are included only partially by explicitly setting the relative permitivity to $\epsilon_r = 15$. However, a polarizable version of the MARTINI force field also exists for proteins, accounting for the orientational polarizability of water molecules and of the side chains of polar and charged amino acid residues (Yesylevskyy et al., 2010). In contrast, a recently developed "dry" version of MARTINI lipids (Arnarez et al., 2015) moved toward an implicit description of the aqueous solvent. Because of smoothened coarse-grained potentials, effective time scales sampled in MARTINI simulations were found to exceed the actual simulation time by a factor of 3–8 (Monticelli et al., 2008). As a result, a scaling factor of 4 is typically used to estimate realistic duration of processes captured in MARTINI trajectories (Monticelli et al., 2008).

2.5 Umbrella sampling

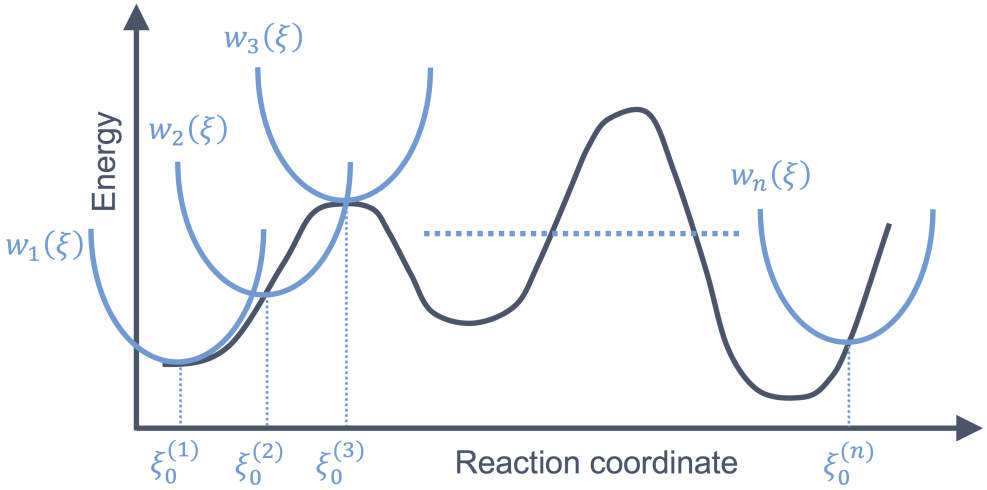

Figure 2.2: Umbrella sampling.

Umbrella sampling is an enhanced-sampling technique that allows calculating the free-energy profile $G(\xi)$ along a chosen reaction coordinate ξ. The free-energy profile is defined as

$$G(\xi) = -k_{\mathrm{B}}T \ln \langle \rho(\xi) \rangle + C \tag{2.12}$$

where $\langle \rho(\xi) \rangle$ is the average distribution function along ξ and C is an arbitrary constant. The average distribution function $\langle \rho(\xi) \rangle$ arises from the Boltzmann distribution function after averaging out all degrees of freedom but ξ

$$\langle \rho(\xi) \rangle = \frac{\int \mathrm{d}\boldsymbol{R}\, \delta(\xi'[\boldsymbol{R}] - \xi)\, e^{\frac{-U(\boldsymbol{R})}{k_{\mathrm{B}}T}}}{\int \mathrm{d}\boldsymbol{R}\, e^{\frac{-U(\boldsymbol{R})}{k_{\mathrm{B}}T}}} \tag{2.13}$$

Here $U(\boldsymbol{R})$ is the total potential energy of the system expressed as a function of the coordinates $\boldsymbol{R}$, and $\xi'[\boldsymbol{R}]$ is the value of the reaction coordinate in a microstate characterized by $\boldsymbol{R}$.

In principle, it is possible to obtain $\langle \rho(\xi) \rangle$ directly from a MD trajectory, relying on the ergodicity of sampling. However, if high energetic barriers are present along ξ, such a direct calculation may become practically impossible since the system may stay trapped in a minimum along ξ, failing to visit the entire range of ξ during a trajectory. To overcome this problem, umbrella sampling uses a biasing potential to confine the system to a limited region of ξ, called an umbrella window, thereby ensuring that the region is properly sampled. Typically, a number of independent simulations are performed with harmonic biasing potentials

$$w_i(\xi) = \frac{1}{2}k(\xi - \xi_0^{(i)})^2 \tag{2.14}$$

centered at successive values $\xi_0^{(i)}$ spanning the reaction coordinate (Fig. 2.2). This yields a biased average distribution function $\langle\rho(\xi)\rangle_{(i)}$ for each umbrella window. Providing that there is sufficiently large overlap between the biased distributions of all neighboring umbrella windows, the desired overall $\langle\rho(\xi)\rangle$ can be recovered from these distributions using the weighted histogram analysis method (WHAM) (Roux, 1995). The method is based on a self-consistent solution of the equation

$$\langle\rho(\xi)\rangle = \frac{\sum_i n_i \langle\rho(\xi)\rangle_{(i)}}{\sum_j n_j e^{-(w_j(\xi)-F_j)/k_\mathrm{B}T}} \tag{2.15}$$

where n_i denotes the number of independent data points in each umbrella window and the constants F_i are calculated from a previous estimate for $\langle\rho(\xi)\rangle$ as

$$e^{-F_i/k_\mathrm{B}T} = \int \mathrm{d}\xi \, e^{-w_i(\xi)/k_\mathrm{B}T} \langle\rho(\xi)\rangle \tag{2.16}$$

The WHAM approach can be readily extended to multidimensional reaction coordinates.

The effectiveness of umbrella sampling critically depends on the choice of the reaction coordinate. For calculations of the difference in free energy between two states, it is essential that the reaction coordinate clearly separates the two states. Moreover, a good reaction coordinate should span over all significant energy barriers. In contrast, if a substantial energy barrier is present in a degree of freedom orthogonal to the reaction coordinate, sampling along this degree of freedom will not be enhanced by the umbrella sampling technique. As a consequence, the resulting free-energy profile may not be converged, but it may rather exhibit dependence on the choice of initial geometries and be subject to hysteresis. Modifications of umbrella sampling have been devised to facilitate the sampling of such "slow" orthogonal degrees of freedom. Replica exchange umbrella sampling (REUS) (Sugita et al., 2000), which is such an algorithm ensuring continuity of states along the reaction coordinate, is described in Section 2.8.

2.6 Replica exchange

Enhanced-sampling techniques based on the replica-exchange algorithm avoid the often tedious search for a good reaction coordinate. Replica-exchange molecular dynamics (REMD) (Sugita and Okamoto, 1999) seeks to accelerate the crossing of energy barriers using additional simulations performed concurrently at higher

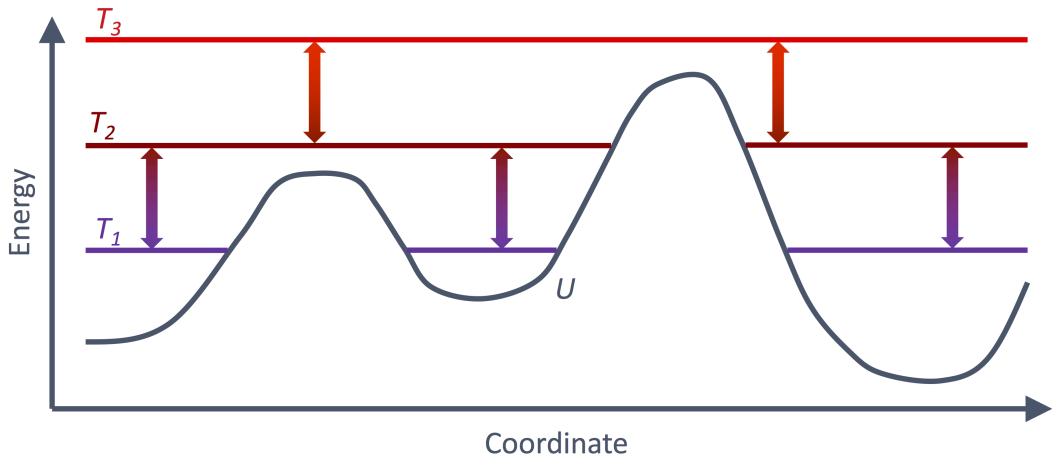

Figure 2.3: Temperature replica-exchange molecular dynamics.

temperatures and/or with modified potential-energy functions. This gives rise to a generalized ensemble $X = (\boldsymbol{R}_1, \ldots, \boldsymbol{R}_M)$ of M non-interacting replicas of the system, each running at a different temperature and/or with a different potential energy function. At regular time intervals, exchanges are attempted which swap replica geometries between neighboring temperatures and/or potential energy functions:

$$X = (\boldsymbol{R}_1, \ldots, \boldsymbol{R}_i, \boldsymbol{R}_{i+1}, \ldots, \boldsymbol{R}_M) \rightarrow X' = (\boldsymbol{R}_1, \ldots, \boldsymbol{R}_{i+1}, \boldsymbol{R}_i, \ldots, \boldsymbol{R}_M) \quad (2.17)$$

Whether an exchange is allowed or not depends on the transition probability which is calculated from an exchange criterion. This criterion ensures that the detailed balance condition is fulfilled:

$$P(X)\, p(X \rightarrow X') = P(X')\, p(X' \rightarrow X) \quad (2.18)$$

Here $P(X)$ is the probability of the state X in the generalized ensemble, given as the product of Boltzmann probabilities for all the replicas, and $p(X \rightarrow X')$ represents the transition probability between the generalized states X and X'. In a general variant of the replica-exchange algorithm (Sugita et al., 2000), where both the temperatures and the potential-energy functions are varied, the detailed balance condition implies that

$$\frac{p(X \rightarrow X')}{p(X' \rightarrow X)} = \exp(-\Delta) \quad (2.19)$$

where

$$\Delta = \frac{1}{k_\mathrm{B}T_i}\left[U_i(\boldsymbol{R}_{i+1}) - U_i(\boldsymbol{R}_i)\right] - \frac{1}{k_\mathrm{B}T_{i+1}}\left[U_{i+1}(\boldsymbol{R}_{i+1}) - U_{i+1}(\boldsymbol{R}_i)\right] \tag{2.20}$$

In this expression, T_i, T_{i+1} and $U_i(\boldsymbol{R}_i)$, $U_{i+1}(\boldsymbol{R}_{i+1})$ are the temperatures and potential energies of the i-th and the $(i+1)$-th replica before the exchange is attempted, while $U_i(\boldsymbol{R}_{i+1})$ and $U_{i+1}(\boldsymbol{R}_i)$ are the respective potential-energy functions evaluated for the two swapped sets of coordinates.

The detailed balance condition (2.18) guarantees that the exchange process converges toward an equilibrium distribution. It is satisfied, for example, by transition probabilities calculated using the Metropolis criterion:

$$p(X \to X') = \begin{cases} 1, & \text{if } \Delta \leq 0, \\ \exp(-\Delta), & \text{if } \Delta > 0. \end{cases} \tag{2.21}$$

Most commonly, only the temperature is varied, which constitutes the temperature replica-exchange (T-REMD) method (Sugita and Okamoto, 1999). In T-REMD, the Δ in eqs. (2.19) and (2.21) reduces to

$$\Delta = \left(\frac{1}{k_\mathrm{B}T_i} - \frac{1}{k_\mathrm{B}T_{i+1}}\right)\left[U(\boldsymbol{R}_{i+1}) - U(\boldsymbol{R}_i)\right] \tag{2.22}$$

By "climbing on a temperature ladder", replicas can cross energy barriers more easily (see Fig. 2.3). Thus, when the replicas return to the lowest temperature, which is typically the one of interest, they enrich the conformational ensemble with conformations that would otherwise take too long to be sampled were it not for the additional temperature levels.

For T-REMD to be effective, the transition rates between the simulations at different temperatures must be sufficiently high. This limits the spacing between the temperature levels since, on average, Δ increases with the temperature spacing, lowering the transition probability. To exemplify this, let $T_{i+1} = (1+\varepsilon)\,T_i$. Then the average potential energies at the temperatures T_i and T_{i+1} are $\langle U\rangle_i = \frac{c}{2}N_\mathrm{df}k_\mathrm{B}T_i$ and $\langle U\rangle_{i+1} = \frac{c}{2}N_\mathrm{df}k_\mathrm{B}T_i(1+\varepsilon)$, where N_df is the total number of degrees of freedom and c is a constant approximately equal to 2 for proteins (Abraham et al., 2016). The average Δ then becomes

$$\langle\Delta\rangle = \frac{\varepsilon^2}{2(1+\varepsilon)}cN_\mathrm{df} \approx \frac{1}{2}\varepsilon^2 cN_\mathrm{df} \tag{2.23}$$

Thus, to ensure that the average transition probability is at least p, the spacing ε between the temperatures must be smaller than $\varepsilon \approx \sqrt{2\ln(1/p)/cN_\mathrm{df}}$. This also

demonstrates that the maximum possible spacing is inversely proportional to the square root of the number of degrees of freedom. As a consequence, the number of replicas needed to reach a desired temperature also grows with $\sqrt{N_{\mathrm{df}}}$.

Other variants of the replica-exchange method include the Hamiltonian replica exchange (H-REMD) (Okamoto, 2004) or the surface-tension REMD (Mori et al., 2013). The H-REMD method varies the potential-energy functions while keeping the temperature constant, and the exchange criterion becomes

$$\Delta = \frac{1}{k_{\mathrm{B}}T}\left[U_i(\boldsymbol{R}_{i+1}) - U_i(\boldsymbol{R}_i) - U_{i+1}(\boldsymbol{R}_{i+1}) + U_{i+1}(\boldsymbol{R}_i)\right] \tag{2.24}$$

In surface-tension REMD, replicas move between different values of surface tension. This method was designed specifically to enhance the lateral diffusion of lipids in lipid bilayers, contributing also to an improved sampling of the membrane embedding of transmembrane peptides (Mori et al., 2013).

2.7 Replica exchange with solute tempering

The scaling of the number of replicas with $\sqrt{N_{\mathrm{df}}}$ makes T-REMD computationally very expensive when the method is applied to large biomolecular systems. To alleviate this problem, replica exchange with solute tempering (REST) (Liu et al., 2005) only heats up a most relevant part of the system, i.e., the "solute", while the rest of the system, i.e., the "solvent", is kept at the original temperature.

In practice, REST is implemented as a special case of H-REMD, achieving the heating-up effectively by scaling the potential-energy terms corresponding to solute–solute and solute–solvent interactions. In its most recent version (REST2) (Wang et al., 2011), the potential-energy function for the i-th "temperature" is given by

$$U_i(\boldsymbol{R}) = \frac{T_0}{T_i}U_{\mathrm{pp}}(\boldsymbol{R}) + \sqrt{\frac{T_0}{T_i}}U_{\mathrm{pw}}(\boldsymbol{R}) + U_{\mathrm{ww}}(\boldsymbol{R}) \tag{2.25}$$

where $U_{\mathrm{pp}}(\boldsymbol{R})$, $U_{\mathrm{pw}}(\boldsymbol{R})$, and $U_{\mathrm{ww}}(\boldsymbol{R})$ are terms corresponding to solute–solute, solute–solvent, and solvent–solvent interactions, respectively. The benefit of potential energies in the form (2.25) lies in the fact that the $U_{\mathrm{ww}}(\boldsymbol{R})$ term is canceled out in the formula (2.24) for the transition probability.

The REST approach has been used, e.g, to study folding of peptides (Wang et al., 2011) or protein thermostability (Stirnemann and Sterpone, 2015), and it has also been applied to simulations of a mixed lipid bilayer (Huang and Garcia, 2014).

2.8 Replica-exchange umbrella sampling

As described in Section 2.5, hidden barriers in degrees of freedom orthogonal to the reaction coordinate can cause poor convergence of umbrella sampling simulations. The convergence of free-energy profiles can be accelerated by coupling the umbrella windows using a H-REMD scheme. This approach, termed replica-exchange umbrella sampling (REUS) (Sugita and Okamoto, 1999), consists in periodic exchanges of geometries between neighboring umbrella windows. The exchange probabilities are evaluated using the Metropolis criterion (2.21) with Δ calculated according to (2.24) as

$$\Delta = \frac{1}{k_\mathrm{B}T}\left[w_i(\xi_{i+1}) - w_i(\xi_i) - w_{i+1}(\xi_{i+1}) + w_{i+1}(\xi_i)\right] \tag{2.26}$$

where ξ_i and ξ_{i+1} are values of the collective variable in the i-th and $(i+1)$-th umbrella window, respectively, and w_i and w_{i+1} are the biasing potentials in these two windows.

Exchanges of geometries between umbrella windows prevent the unfavorable situation that geometries in two neighboring umbrella windows remain trapped in two different minima of an orthogonal degree of freedom. In this way, REUS ensures continuity of sampling along the reaction coordinate. Moreover, since each umbrella window is visited by multiple geometries started from different initial conditions, the sampling of orthogonal degrees of freedom can be significantly enhanced (Neale et al., 2013). A disadvantage of REUS as compared to traditional umbrella sampling is the requirement that all umbrella windows must be simulated at the same time, which may become computationally rather demanding for large systems.

Chapter 3

Membrane fluorescent probes

This chapter introduces the work presented in paper I, which describes a combined effort based on MD simulations, TD-DFT calculations, and polarization microscopy to gain an insight into molecular orientation in lipid membranes. After setting the stage by introducing measurements of molecular orientations using polarization microscopy, we discuss the underlying concepts of the anisotropy of light absorption by fluorescent molecules. We then show that MD simulations coupled with TD-DFT calculations are not only able to reproduce experimental results, but that they also provide a solid basis for a quantitative interpretation of polarization microscopy experiments.

3.1 Orientation of membrane fluorescent probes

Molecules embedded in biological membranes or peripherally attached to them typically display some sort of orientational order relative to the membrane surface In fact, this applies as well to lipids constituting the lipid bilayer and also to integral and peripheral membrane proteins (Kress et al., 2011). The physiological functionality of these diverse molecules is often closely related to their orientation with respect to the membrane (Czogalla et al., 2014; Dowhan and Bogdanov, 2009), and many cellular processes involve changes in orientation of membrane-associated molecules (Bondar and Lazar, 2014).

Fluorescence techniques based on light polarization have been used to probe orientations of various membrane-associated fluorescent probes and labels (Axelrod, 1979; Benninger et al., 2005; Farkas and Webb, 2010). These techniques, including measurements of linear dichroism or fluorescence anisotropy (Lakowicz, 2006), rely on the anisotropic nature of light absorption and/or emission by fluorescent molecules. In particular, the 2PPM technique, developed by Lazar et al. (2011), measures fluorescence-detected linear dichroism (FDLD), i.e., the

dependence of light absorption, reported by changes in fluorescence intensity, on the orientation of incident linearly polarized light. FDLD is expressed by means of the dichroic ratio

$$r = \frac{I_h}{I_v}, \tag{3.1}$$

which compares intensities of fluorescence elicited by illuminating the sample with two perpendicular directions of light polarization (Fig. 3.1). Thus, the dichroic ratio is a measure of the anisotropy of light absorption by fluorescent molecules present in the sample.

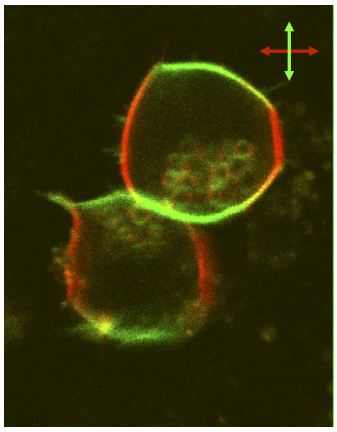

Figure 3.1: A 2PPM image of cells expressing a genetically-encoded fluorescent protein construct, predominantly bound in the plasma membrane. The picture is a composite of a red and a green image, each capturing fluorescence elicited by light polarized along the direction indicated by the respective arrow.

A previous publication (Lazar et al., 2011), co-authored by the author of this thesis, showed that numerous genetically-encoded fluorescent protein constructs exhibit FDLD when bound to cell membranes. Moreover, it demonstrated that FDLD measurement can be used to detect processes occurring in living cells, such as changes in calcium concentration. The 2PPM technique developed for such measurements utilizes the nonlinear process of two-photon (2P) absorption to excite fluorescent molecules, a process in which two photons are absorbed quasi-simultaneously by a molecule. The use of 2P absorption offers several advantages, such as a deeper penetration into a living tissue, restriction of fluorescence to a small volume around the focal point, or less photobleaching (Brasselet, 2011). To quantify FDLD in 2PPM images of living cells, we devised a computational procedure that allows for characterization of the cell outline and for calculation of the dichroic ratio at different points along the membrane (Lazar et al., 2011).

The dichroic ratio contains information on the distribution of orientations of membrane-bound fluorescent molecules with respect to the membrane (Fig. 3.2). However, structural interpretation of the dichroic ratio requires assump-

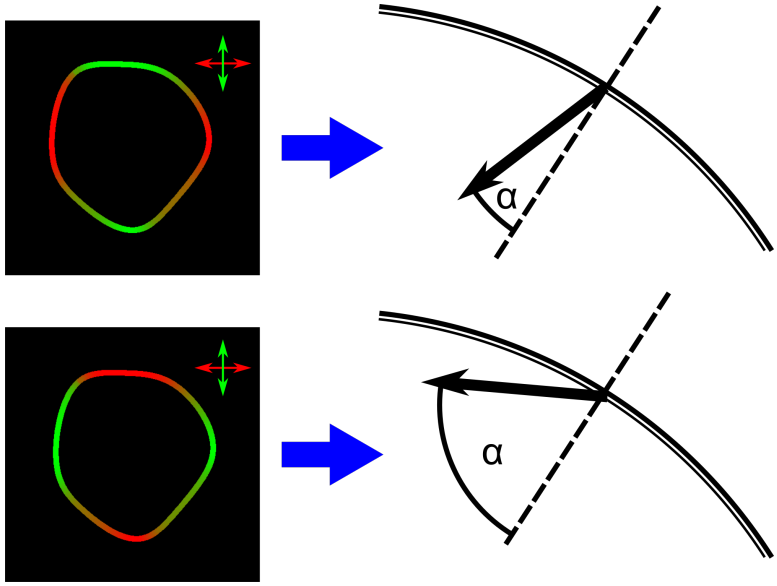

Figure 3.2: The dichroic ratio contains information on molecular orientation with respect to the plasma membrane.

tions on the functional form of the orientational distribution and, importantly, the knowledge of absorption properties of the fluorophore (Timr, 2013). Of particular importance is to know how the absorption cross section depends on the direction of light polarization with respect to the molecular geometry of the fluorophore. In the case of one-photon (1P) absorption, the geometric dependence of the absorption cross section is given by a single vector, the transition dipole moment (TDM) (see Section 3.2). In contrast, for multi-photon absorption, such as the 2P absorption, the absorption cross section becomes generally more complex (Section 3.2). In a previous article (Timr et al., 2014), we investigated a model system of a hydroxyflavone dye (F2N12S, see Fig. 3.3) embedded in a phospholipid membrane. By comparing a combination of 1P and 2P FDLD measurements on fluorescence-labeled giant unilamellar vesicles (GUVs) with a combination of MD simulations and TD-DFT calculations, we demonstrated that the orientational distribution recovered from experimental data was in good agreement with the computational prediction. However, our study was limited to a single membrane fluorescent probe, and our analysis of the 2P data relied on a simplified vectorial description of the 2P absorption cross section using the TDM. In the present work, we examined in detail the behavior of the 2P absorption cross section in the membrane environment and we tested whether its shape allows for determining the orientations of membrane fluorescent probes. To this end, we continued using plain phospholipid bilayers as simplified models of the plasma membrane, but we also considered an additional membrane fluorescent probe, the carbocyanine dye DiI (see Fig. 3.3), chemically and optically different from F2N12S.

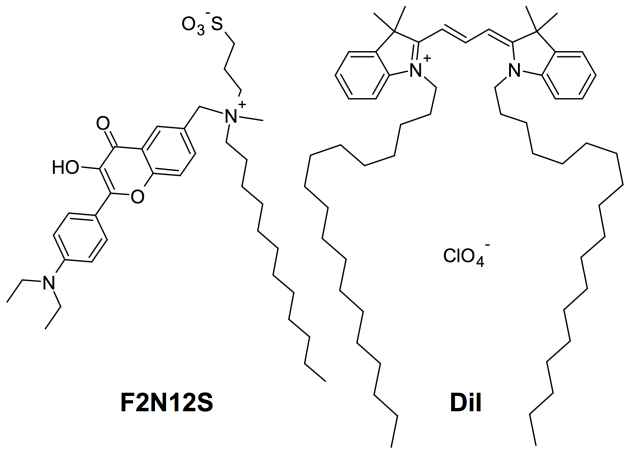

Figure 3.3: Membrane fluorescent probes investigated in this work.

3.2 Anisotropy of 1P and 2P absorption

The anisotropy of 1P absorption has a directional, "antenna-like" character. The probability that a molecule absorbs an incident linearly polarized photon and becomes excited from the ground state g to a higher-energy state f is given by the 1P absorption cross section (Boyd, 2008)

$$\sigma_{gf}^{1\mathrm{P}} = A^{1\mathrm{P}} \left|\boldsymbol{\mu}_{gf} \cdot \boldsymbol{e}\right|^2 2\pi g(\omega) \tag{3.2}$$

In this expression, $\boldsymbol{\mu}_{gf}$ is the TDM corresponding to the transition between the states g and f, $\boldsymbol{e}$ is the direction of the polarization of the incoming photon, ω stands for its angular frequency, $g(\omega)$ is a normalized line shape function, and the prefactor $A^{1\mathrm{P}}$ equals

$$A^{1\mathrm{P}} = \frac{2\omega}{\hbar n \epsilon_0 c} \tag{3.3}$$

where $\hbar$ is the Planck constant, n is the refractive index of the environment, and c is the speed of light in vacuum. The TDM is a nondiagonal matrix element of the molecular dipole operator $\hat{\boldsymbol{\mu}}$,

$$\boldsymbol{\mu}_{gf} = \langle f|\hat{\boldsymbol{\mu}}|g\rangle \tag{3.4}$$

The molecular dipole operator $\hat{\boldsymbol{\mu}}$ consists of a nuclear part $\hat{\boldsymbol{\mu}}^{(\mathrm{n})}$ and an electronic part $\hat{\boldsymbol{\mu}}^{(\mathrm{e})}$,

$$\hat{\boldsymbol{\mu}} = \hat{\boldsymbol{\mu}}^{(\mathrm{n})} + \hat{\boldsymbol{\mu}}^{(\mathrm{e})} = \sum_J q_J \hat{\boldsymbol{R}}_J - \sum_j e\hat{\boldsymbol{r}}_j \tag{3.5}$$

where q_J and $\boldsymbol{R}_J$ are the charges and the positions of the nuclei, e is the elementary charge, and $\boldsymbol{r}_j$ denotes the positions of the electrons. In the realm of

the Franck–Condon approximation, the direction of the TDM is determined only by the electronic part of $\hat{\boldsymbol{\mu}}$ (Timr, 2013); therefore, in the following we focus exclusively on electronic transitions, and we evaluate the TDM only for transitions between electronic states. From (3.2), assuming that the elements of the TDM are real, it follows that

$$\sigma_{gf}^{\mathrm{1P}} \propto \cos^2 \beta \tag{3.6}$$

where β is the angle between the TDM and the direction of light polarization. Thus, the dependence of the 1P absorption cross section on the direction of light polarization has a simple geometric form which can be visualized as a surface shown in Fig. 3.4. The fact that the 1P absorption cross section has only a single direction of maximum absorption, coinciding with the TDM, allows for determination of molecular orientation by illuminating the molecule with light polarized in different directions, as is the case in FDLD measurements.

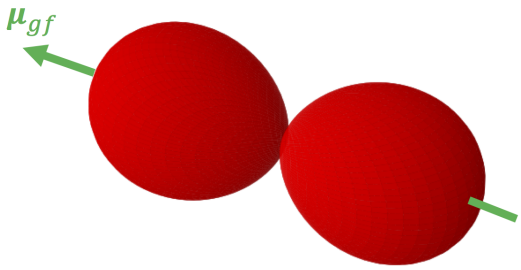

Figure 3.4: The directional, "antenna-like" shape of the 1P absorption cross section, which is given by $\cos^2$ of the angle between the TDM and the direction of light polarization.

Owing to the nonlinear nature of 2P absorption, the general formula for the 2P absorption cross section is more complicated than it is in the 1P case. It reads (Boyd, 2008)

$$\sigma_{gf}^{\mathrm{2P}} = A^{\mathrm{2P}} \left| \sum_m \frac{(\boldsymbol{\mu}_{gm} \cdot \boldsymbol{e})(\boldsymbol{\mu}_{mf} \cdot \boldsymbol{e})}{(\omega_{gm} - \omega)} \right|^2 2\pi g(2\omega) \tag{3.7}$$

where

$$A^{\mathrm{2P}} = \frac{8\omega^2}{\hbar^2 n^2 \epsilon_0^2 c^2} \tag{3.8}$$

The sum in expression (3.7) runs over all states of the molecule, including the ground state g and the final excited state f, and it can be written as

$$\sum_m \frac{(\boldsymbol{\mu}_{gm} \cdot \boldsymbol{e})(\boldsymbol{\mu}_{mf} \cdot \boldsymbol{e})}{(\omega_{gm} - \omega)} = \frac{1}{2} \boldsymbol{e}^T \, \mathbf{S}_{gf} \, \boldsymbol{e} \tag{3.9}$$

where $\mathbf{S}_{gf}$ is the 2P transition tensor with elements (Steindal et al., 2012)

$$(\mathrm{S}_{gf})_{kl} = \sum_m \left[\frac{(\mu_{gm})_k \, (\mu_{mf})_l}{(\omega_{gm} - \omega)} + \frac{(\mu_{gm})_l \, (\mu_{mf})_k}{(\omega_{gm} - \omega)} \right] \tag{3.10}$$

forming a 3×3 symmetric matrix. Assuming that this matrix has real elements, we can diagonalize it and write the product in (3.9) as

$$\boldsymbol{e}^T \, \mathbf{S}_{gf} \, \boldsymbol{e} = s_1 \, (\boldsymbol{v}_1 \cdot \boldsymbol{e})^2 + s_2 \, (\boldsymbol{v}_2 \cdot \boldsymbol{e})^2 + s_3 \, (\boldsymbol{v}_3 \cdot \boldsymbol{e})^2 \tag{3.11}$$

where s_i and $\boldsymbol{v}_i$ are the three eigenvalues and eigenvectors of the $\mathbf{S}_{gf}$ tensor. Depending on the eigenvalues of $\mathbf{S}_{gf}$, the 2P absorption cross sections can have very different geometric shapes (Fig. 3.5). If the tensor only has a single dominant eigenvalue s_1, the 2P absorption cross section becomes

$$\sigma_{gf}^{\mathrm{2P}} \approx \frac{A^{\mathrm{2P}} s_1^2}{4} \, (\boldsymbol{v}_1 \cdot \boldsymbol{e})^4 \, 2\pi g(2\omega) \propto \cos^4 \beta \tag{3.12}$$

where β is the angle between the direction of light polarization and the eigenvector corresponding to the single non-zero eigenvalue. Thus the tensorial description of the 2P absorption anisotropy can be replaced by a simplified vectorial description, analogous to the 1P case. In contrast, with more dominant eigenvalues, the 2P absorption cross section becomes progressively less directional (Fig. 3.5), which may preclude the determination of orientation by FDLD measurements.

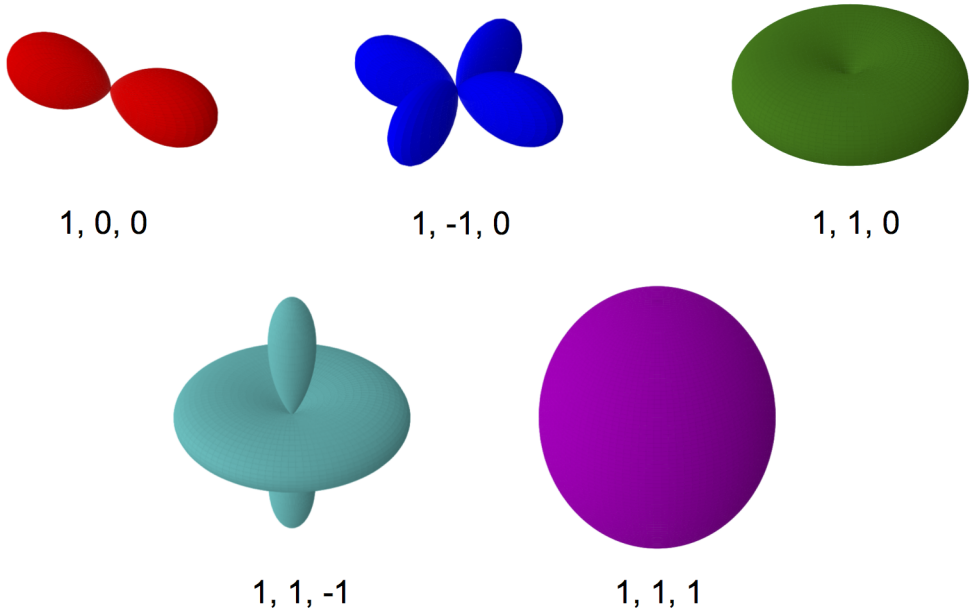

Figure 3.5: Anisotropy of the 2P absorption cross section depends on the eigenvalues of the 2P transition tensor.

A particular example of the "vector-like" behavior of the 2P transition tensor occurs if the TDM $\boldsymbol{\mu}_{gf}$ is approximately parallel to the change $\Delta\boldsymbol{\mu}_{gf}$ in the molecular dipole moment upon excitation from g to f and, at the same time, if $\Delta\boldsymbol{\mu}_{gf}$ is large. This is because the sum in (3.7) can be divided into a pair of contributions (Drobizhev et al., 2006; Karotki, 2003),

$$\sum_m \frac{(\boldsymbol{\mu}_{gm}\cdot\boldsymbol{e})(\boldsymbol{\mu}_{mf}\cdot\boldsymbol{e})}{(\omega_{gm}-\omega)} = \sum_{m\neq g,f} \frac{(\boldsymbol{\mu}_{gm}\cdot\boldsymbol{e})(\boldsymbol{\mu}_{mf}\cdot\boldsymbol{e})}{(\omega_{gm}-\omega)} + \frac{1}{\omega}(\boldsymbol{\mu}_{gf}\cdot\boldsymbol{e})(\Delta\boldsymbol{\mu}_{gf}\cdot\boldsymbol{e}) \quad (3.13)$$

The first term accounts for transitions via all possible intermediate states while the second term corresponds to a direct transition from the ground state g to the final excited state f. If the second term dominates over the first one and if the vectors $\boldsymbol{\mu}_{gf}$ and $\Delta\boldsymbol{\mu}_{gf}$ are close to parallel, the 2P absorption cross section becomes proportional to the angle β between $\boldsymbol{\mu}_{gf}$ and the direction of light polarization,

$$\sigma_{gf}^{\mathrm{2P}} \propto |(\boldsymbol{\mu}_{gf}\cdot\boldsymbol{e})(\Delta\boldsymbol{\mu}_{gf}\cdot\boldsymbol{e})|^2 \propto (\boldsymbol{\mu}_{gf}\cdot\boldsymbol{e})^4 \propto \cos^4\beta \quad (3.14)$$

3.3 Computational approach

To examine the behavior of 1P and 2P absorption cross sections in the membrane environment, we performed classical MD simulations coupled with linear-response and quadratic-response TD-DFT calculations.

We had already done MD simulations of the F2N12S probe in a 1-palmitoyl-2-oleoylphosphatidylcholine (POPC) bilayer in our previous study (Timr et al., 2014). In the present work, we conducted a similar MD simulation for the second probe, DiI (Fig. 3.3). The simulation box contained a lipid bilayer formed by 128 POPC lipids. This lipid bilayer was surrounded by ∼5000 water molecules containing one Cl^- anion to neutralize the positive charge of the DiI fluorophore. Before, the start of the simulation, we inserted a DiI molecule into bulk water far from the membrane surface.

To be consistent with our previous work, we used the same sets of force field parameters to describe the system. Namely, we employed the united-atom Berger lipid force field (Berger et al., 1997) to parameterize the POPC molecules and the SPC model (Berendsen et al., 1981) to describe water. The DiI probe was parameterized using the GROMOS-87 force field (van Gunsteren and Berendsen, 1987) with corrections as detailed in (van Buuren et al., 1993; Mark et al., 1994) (originally referred to as the GROMACS force field), and its methyl, methanediyl, and methine groups were described using the corresponding atom types taken

from the Berger lipid force field. Finally, the partial charges of the fluorophore were obtained from a Merz–Kollman–Singh ESP fit (Singh and Kollman, 1984) for a structure geometry-optimized using the CAM-B3LYP functional (Yanai et al., 2004) in the cc-pVDZ basis set (Dunning, 1989).

The MD simulation was performed using the GROMACS package (Hess et al., 2008). Newton's equations of motion were integrated with a time step of 2 fs by employing the leap-frog algorithm (Hockney et al., 1974). Long-range electrostatic interactions were accounted for by using the particle mesh Ewald summation (Darden et al., 1993). The temperature of the system was kept at 310 K by the Nosé-Hoover thermostat (Hoover, 1985), and the Parrinello–Rahman barostat (Parrinello and Rahman, 1981) was utilized for semi-isotropic pressure coupling with a reference pressure of 1.01 bar. After an energy-minimization and a 100 ns equilibration, during which the probe spontaneously moved to the membrane interior, we simulated the system for 1.5 µs.

From the resulting DiI trajectory, as well as from trajectories obtained previously for F2N12S, we randomly selected a set of snapshots (more than 60 in each case). For each of the geometries we calculated the 1P and 2P absorption anisotropy of the fluorescent probe in the membrane environment, focusing on the $S_0 \rightarrow S_1$ transition probed in experiments. For this purpose, we utilized the linear-response and quadratic-response TD-DFT. By evaluating the electronic density response to an external potential, these methods allow calculating the components of $\boldsymbol{\mu}_{gf}$ and $\mathbf{S}_{gf}$ from linear and quadratic response functions (Olsen and Jorgensen, 1985; Frediani et al., 2005; Salek et al., 2003) as

$$|(\mu_{gf})_j|^2 = \lim_{\omega \to \omega_{gf}} (\omega - \omega_{gf}) \langle\langle \hat{\mu}_j; \hat{\mu}_j \rangle\rangle_\omega \tag{3.15}$$

$$(\mathrm{S}_{gf})_{jk} = - \lim_{\omega \to \omega_{gf}} (\omega - \omega_{gf}) \langle\langle \hat{\mu}_j; \hat{\mu}_k, \hat{\mu}_l \rangle\rangle_{\omega_{gf}/2,\omega} / (\mu_{gf})_l \tag{3.16}$$

where $\langle\langle \hat{\mu}_j; \hat{\mu}_j \rangle\rangle_\omega$ and $\langle\langle \hat{\mu}_j; \hat{\mu}_k, \hat{\mu}_l \rangle\rangle_{\omega_{gf}/2,\omega}$ are the linear and quadratic frequency-dependent response functions for the components of the dipole operator $\hat{\boldsymbol{\mu}}$. We used an implementation of the linear-response and quadratic-response TD-DFT in the DALTON 2013 program (Aidas et al., 2014; http://daltonprogram.org, 2013), and we performed our 1P and 2P calculations using the B3LYP functional (Becke, 1993) and the cc-pVDZ basis set (Dunning, 1989). We also verified the consistency of the results with respect to the choice of the functional and the basis set. To account for the effects of the membrane environment, we included the surrounding lipid and water molecules into our calculations as point charges.

3.4 Structural interpretation of experiments

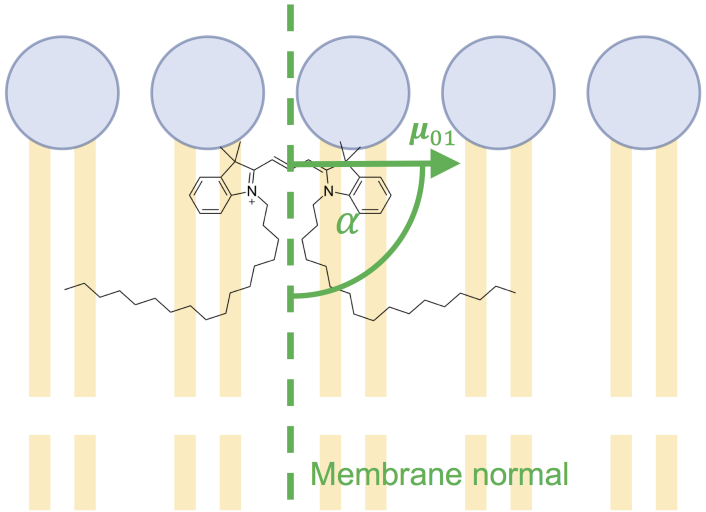

Figure 3.6: Structural interpretation of FDLD measurements.

1P FDLD measurements supply $\langle \cos^2 \alpha \rangle$, i.e., the expectation value of $\cos^2$ of the angle between the TDM and the membrane normal (Fig. 3.6, see Appendix A for more details). Providing that the 2P absorption cross section is directional and can be described with a vector, 2P FDLD measurements give information on $\langle \cos^2 \alpha' \rangle$ and $\langle \cos^4 \alpha' \rangle$, where α' is the angle between such a vector and the membrane normal. Moreover, if this dominant eigenvector of the 2P transition tensor coincides with the TDM, a combination of 2P and 1P measurements can be utilized to obtain more accurate values of $\langle \cos^2 \alpha \rangle$.

The expectation values $\langle \cos^2 \alpha \rangle$ and $\langle \cos^4 \alpha \rangle$ contain information on the distribution of orientations of the TDM relative to the membrane normal. The orientational distribution, however, is not uniquely defined by these two parameters; therefore, determination of the distribution of orientations requires assumptions on its functional form. Commonly assumed functions include a Gaussian-shaped distribution, an entropy-maximizing distribution, a truncated expansion into Legendre polynomials, or a truncated Fourier expansion. An overview of these different distribution functions is given in Appendix A.

We analyzed a combination of 1P and 2P FDLD data collected from fluorescence labeled POPC GUVs with the assumption that the 2P absorption cross section can be described with the TDM vector. Our goal was to compare the orientational distribution functions constructed from experimental data with those from a combination of MD simulations and TD-DFT calculations. A good agreement between such distributions would provide further justification for the simplified vectorial description of 2P absorption anisotropy using the TDM.

3.5 Results

Our initial calculations of the 2P absorption cross section for optimized geometries in vacuum yielded two markedly different results (Fig. 3.7). For F2N12S, the change $\Delta\boldsymbol{\mu}_{01}$ in the permanent dipole was large (11.5 Debye) and approximately parallel to the TDM $\boldsymbol{\mu}_{01}$. As a result, the 2P transition tensor had only a single dominant eigenvalue, and the 2P absorption cross section could be described with the dominant eigenvector $\boldsymbol{v}_1$. For DiI, in contrast, the change $\Delta\boldsymbol{\mu}_{01}$ in the permanent dipole was more than ten times smaller than for F2N12S, and it pointed in a direction perpendicular to the TDM. As a consequence, the 2P absorption tensor had two dominant eigenvalues of the same magnitude, and the 2P absorption cross section could not be described with a single vector.

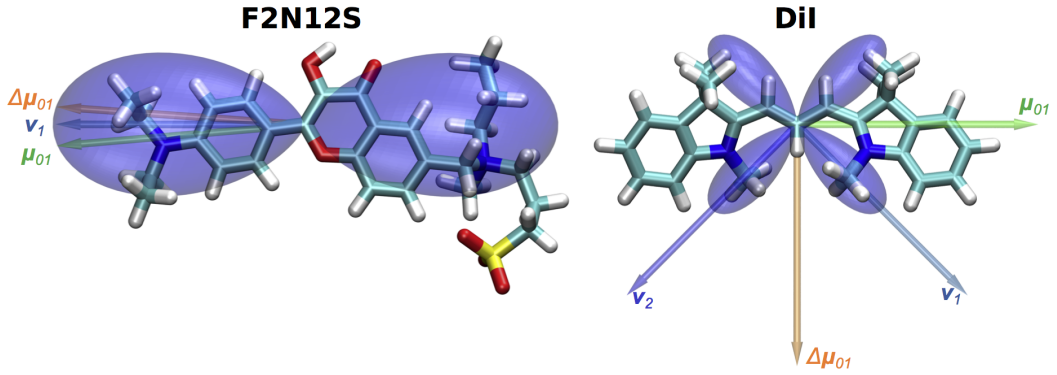

Figure 3.7: 2P absorption cross section of energy-optimized geometries.

To obtain a more dynamic picture of the two probes, we performed MD simulations of their behavior in the membrane environment. The results of a trajectory analysis for F2N12S were already described in (Timr et al., 2014). For DiI, we likewise observed a relatively fast spontaneous translocation of the probe from the bulk solution to the membrane interior. The chromophore of DiI became accommodated somewhat below the head group region while the two 18-carbon alkyl chains of the probe penetrated deep into the hydrophobic core of the bilayer (Fig. 3.8A,B). The long axis of the chromophore adopted a relatively wide range of orientations with respect to the membrane normal, with the average orientation being parallel to the membrane surface (Fig. 3.8C). We also observed twisting motions ($\sim 30°$) of the two pairs of rings along the conjugated bridge as well as bending and slight puckering of these two ring systems.

Our calculation of 1P and 2P optical properties on an ensemble of geometries extracted from MD showed essentially no difference for F2N12S when compared to the optimized geometry. The change $\Delta\boldsymbol{\mu}_{01}$ in the permanent dipole continued pointing approximately in the direction of the TDM $\boldsymbol{\mu}_{01}$ (Fig. 3.9), and the 2P

transition tensor still had a single dominant eigenvalue. For many snapshots of DiI, in contrast, the calculated properties deviated significantly from those obtained for the optimized geometry, owing to the fact that the original symmetry of the chromophore was broken by thermal motions of the membrane-embedded probe. In particular, the change $\Delta\boldsymbol{\mu}_{01}$ in the permanent dipole, which was perpendicular to the TDM in the optimized geometry, adopted a broad range of angles with respect to the TDM, which remained parallel with the long axis of the chromophore. Moreover, the magnitude of $\Delta\boldsymbol{\mu}_{01}$ became up to four times higher for some snapshots than for the optimized geometry. Importantly, the magnitude of $\Delta\boldsymbol{\mu}_{01}$ tended to be the largest for geometries in which $\Delta\boldsymbol{\mu}_{01}$ became roughly parallel with the TDM and thus also approximately parallel with the conjugated bridge of the chromophore (see Fig. 3.10 for an illustration). Since the 2P absorption cross section depends quadratically on the magnitude of $\Delta\boldsymbol{\mu}_{01}$, those were also the snapshots that contributed the most to the overall effective 2P cross section. As a result, the effective 2P cross section became directional (Fig. 3.11), with the direction of the maximum absorption coinciding with the TDM. Thus, we found that the vectorial description of the 2P absorption cross section is applicable to both fluorescent probes, even if initial calculations on an energy-minimized geometry suggested the opposite for DiI.

This finding was further supported by a good agreement between the orientational distributions of the TDM obtained from MD trajectories and those gained by fitting the experimental data (see Fig. 3.12). It is also notable that all the four different functional forms used for the fitting of experimental data (i.e., a Gaussian-shaped distribution, an entropy-maximizing distribution, a fourth-order expansion into Legendre polynomials, and a fourth-order Fourier expansion) resulted in robustly consistent orientational distributions (Fig. 3.12).

Altogether, the combination of our computational results and the experimental data indicates that the vectorial description of the 2P absorption section is likely applicable to a wide range of fluorescent probes, especially if they have a rod-like shape, causing an alignment of the change in the molecular dipole and the TDM. The directionality of 2P absorption anisotropy preconditions its use for probing molecular orientations, and the ability to describe the 2P absorption cross section with a vector greatly simplifies the analysis of experimental data. Therefore, our findings provide a solid basis for the use of FDLD measurements to determine orientations of fluorescent molecules associated with biological membranes.

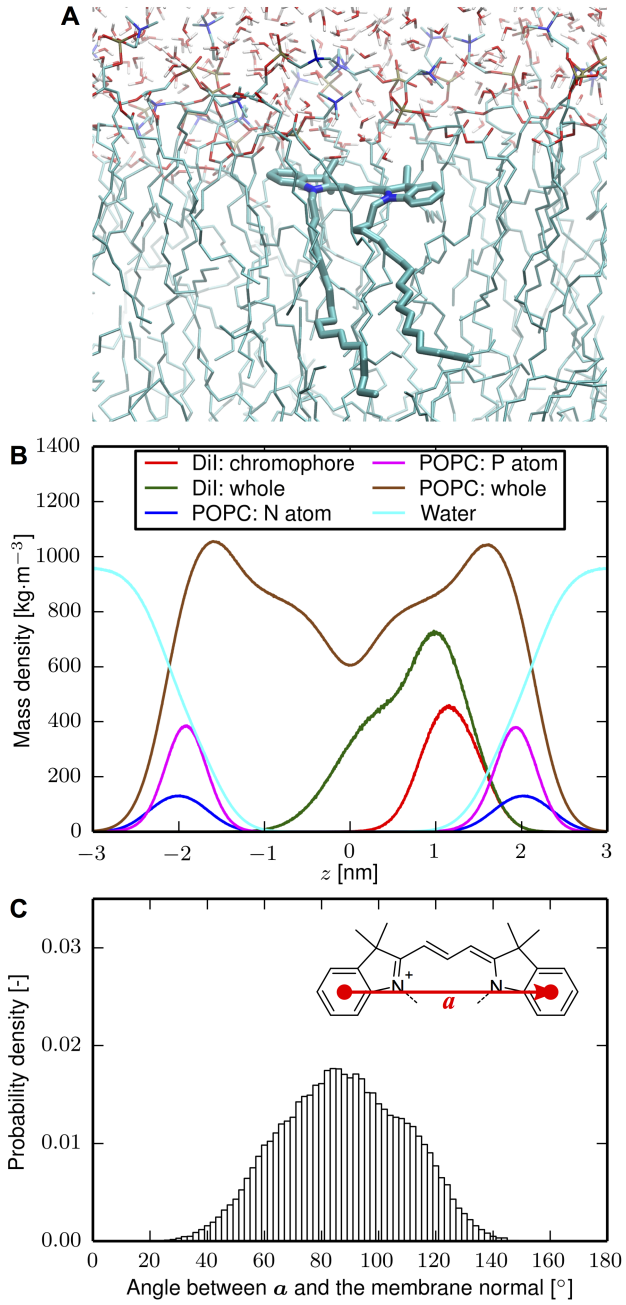

Figure 3.8: Results from a MD trajectory of DiI in a POPC bilayer. **(A)** A typical snapshot from MD. **(B)** Position of the fluorescent probe in the bilayer. **(C)** Orientational distribution of the long axis of the chromophore.

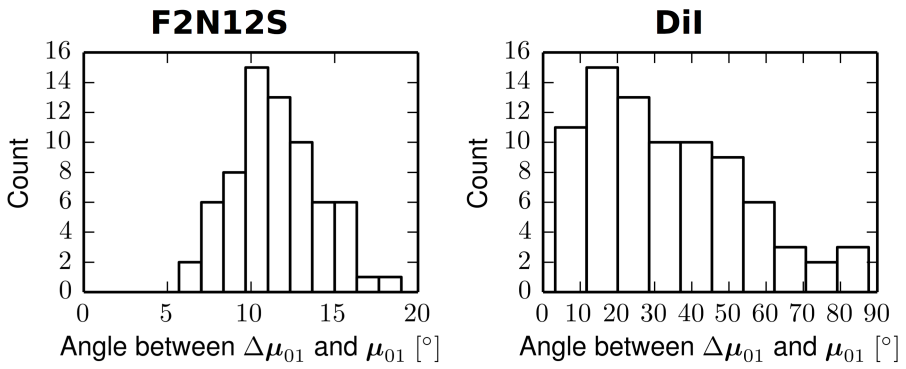

Figure 3.9: Histograms of the angle between the TDM and the change in the permanent dipole for ensembles of geometries obtained from MD.

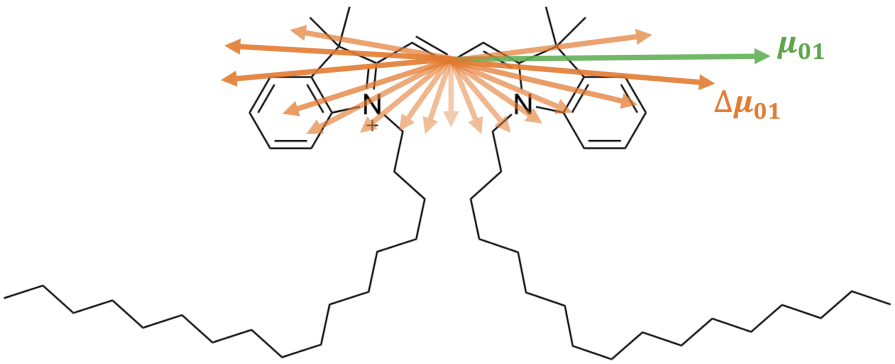

Figure 3.10: Change in the permanent dipole tends to be the largest along the conjugated bridge of DiI.

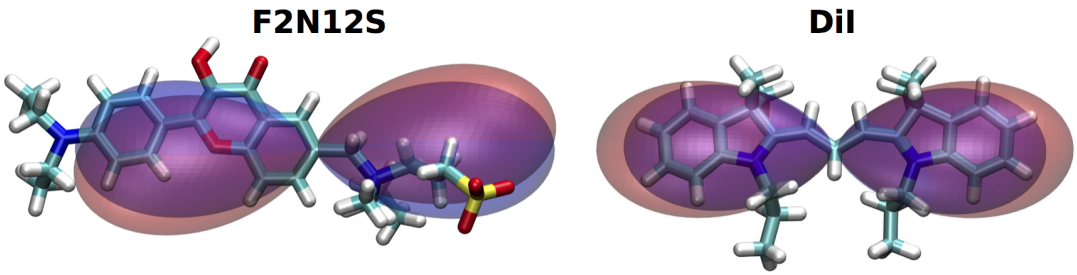

Figure 3.11: Effective 2P absorption cross sections for ensembles of geometries from MD (blue surfaces), compared with a simplified vectorial description using the TDM (red surfaces).

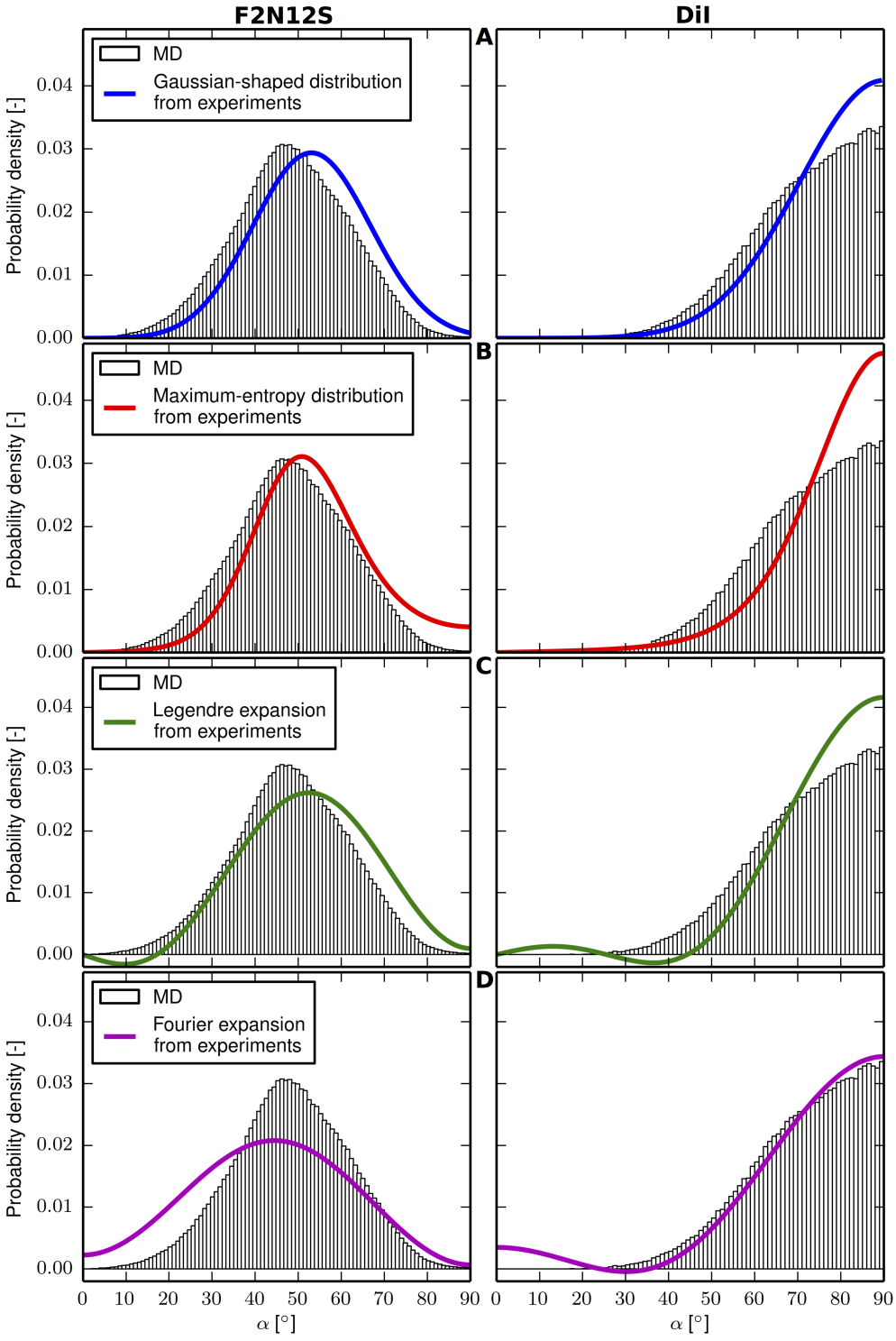

Figure 3.12: Orientational distributions of the TDM relative to the membrane normal for F2N12S **(left)** and DiI **(right)**. Histograms from MD are compared with orientational distributions derived from a combination of 1P and 2P FDLD measurements. Different assumptions on the functional form of these microscopy-derived distributions are used: **(A)** single Gaussian peak, **(B)** entropy maximizing distribution, **(C)** fourth-order expansion into Legendre polynomials, and **(D)** fourth-order Fourier expansion. The data for F2N12S come from (Timr et al., 2014).

Chapter 4

Membrane binding of recoverin

The previous chapter discussed the orientations of synthetic fluorescent probes, which were found to readily translocate into phospholipid bilayers. Here we shift the focus toward the peripheral membrane binding of biological calcium sensors. More specifically, this chapter provides an introduction to paper II, which deals with the reversible membrane binding of the calcium-sensing protein recoverin. First, we briefly introduce the family of proteins equipped with a myristoyl switch and describe the structure and the biological significance of recoverin. We then continue by outlining our simulation approach and summarizing the results of our atomistic and coarse-grained MD simulations. Using these simulations, we managed to capture the membrane insertion of the myristoyl moiety and reveal the role of protein–membrane electrostatic interactions in the membrane association.

4.1 Myristoyl switches

In living organisms, numerous proteins associate peripherally with cellular membranes, which allows these proteins to interact with their substrates, effectors, and binding partners (Stillwell, 2016; Murray et al., 2002). The peripheral membrane binding can be accomplished by specific or nonspecific interactions. Specific interactions typically involve binding of a specialized protein domain to a particular lipid species, such as the binding of the pleckstrin homology (PH) domain of phosholipase C-δ to phosphatidylinositol 4,5-bisphosphate (PIP_2). In contrast, nonspecific interactions arise from the embedding of a nonpolar part of the protein in the hydrophobic membrane interior and from the electrostatic potential felt by charged protein residues in the vicinity of the lipid bilayer.

Hydrophobic nonspecific interactions are often due to the presence of fatty acids covalently attached to the protein. The two most common acylation motifs are myristate, a 14-carbon saturated fatty acid (Fig. 4.1) and palmitate, a 16-

carbon saturated fatty acid. One or more of such acyl chains become attached to the protein during or after translation. Specifically, myristoylation occurs co-translationally and is catalyzed by *N*-myristoyl transferase, which links the myristoyl moiety to the N-terminal glycine via an amide bond (Resh, 1999).

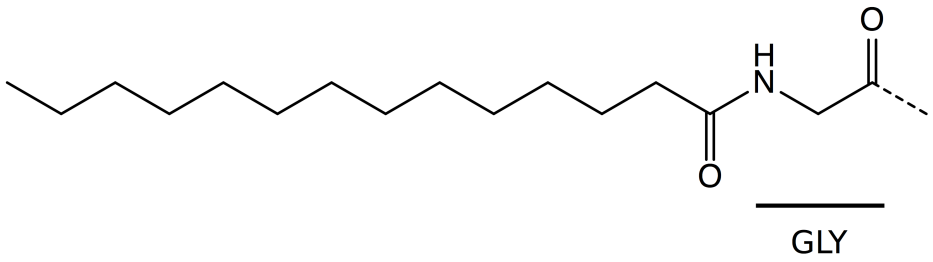

Figure 4.1: N-myristoylation

To achieve reversible membrane binding, some palmitoylated proteins undergo regulated cycles of palmitoylation and depalmitoylation. In contrast, the myristoyl group is not cleaved off during the lifetime of a protein. Instead, a number of N-myristoylated proteins are equipped with a myristoyl switch, a mechanism, usually triggered by ligand binding, that allows the myristoyl moiety to alternate between being hidden inside the protein and being exposed at the protein surface. Thus, by modulating the exposure of the myristoyl moiety, the myristoyl switch regulates the affinity of the protein for membranes. Proteins featuring a ligand-induced myristoyl switch include the Arf protein, the catalytic subunit of protein kinase A, and various calcium sensor proteins such as recoverin, hippocalcin, visinin-like proteins, neurocalcins, or frequenin (Resh, 2006).

Experimental evidence indicates that a single myristoyl group is not sufficient to bind a protein stably to a membrane (Peitzsch and McLaughlin, 1993). Therefore, the "two-signal" hypothesis was proposed, according to which stable membrane anchoring requires an additional factor (Sigal et al., 1994). This can be an extra acylation motif or a patch of positively charged amino-acid residues interacting with the head groups of negatively charged lipids (Fig. 4.2). Supported also by calculations using the non-linear Poisson–Boltzmann equation (see Section 2.1), experiments varying membrane lipid composition found that protein–membrane electrostatic interactions play an important role in the membrane association of several myristoylated proteins, such as Src (Sigal et al., 1994), MARCKS (Murray et al., 2002), or retroviral Gag proteins (Nanda et al., 2010; Barros et al., 2016).

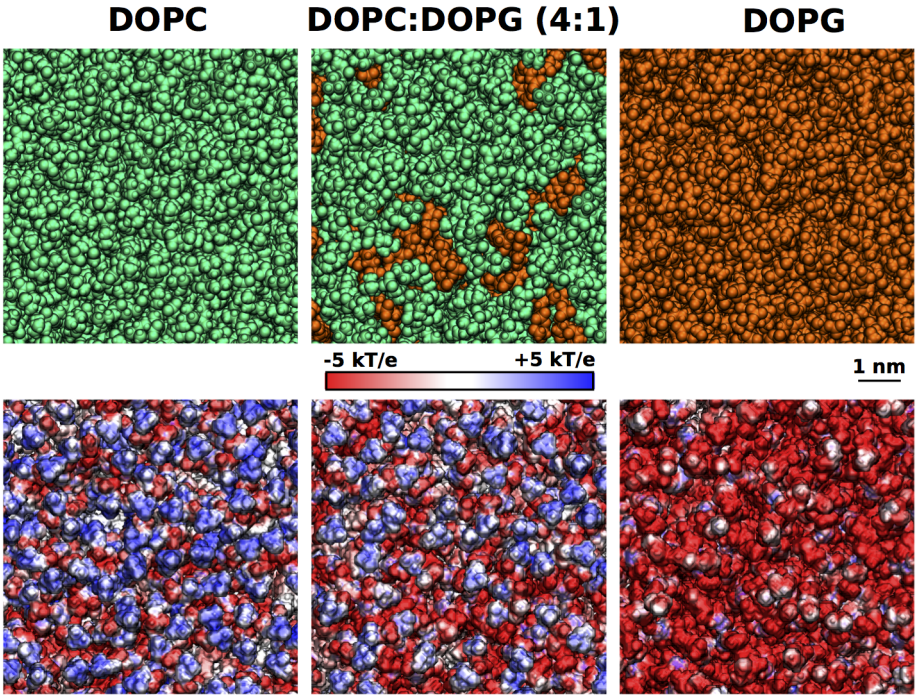

Figure 4.2: Electrostatic potential in the head group region of a lipid bilayer as a function of the concentration of negatively charged lipids. **(Top)** Views of the lipid head groups from above, with neutral di-oleoylphosphatidylcholine (DOPC) molecules depicted in green and negatively charged di-oleoylphoshatidylglycerol (DOPG) shown in orange. **(Bottom)** The corresponding electrostatic potentials on the membrane surface, evaluated by means of the Poisson-Boltzmann theory (see Section 2.1) in a 150 mM implicitly described monovalent salt solution using the APBS software (Baker et al., 2001).

4.2 Recoverin and its biological significance

Recoverin is a globular 23 kDa protein featuring a calcium-induced myristoyl switch. It belongs to the family of neuronal calcium sensors (NCS), which are calcium-sensing proteins expressed in neuronal cells (Burgoyne et al., 2004; Burgoyne, 2007). Recoverin, in particular, is found in the photoreceptor cells of the vertebrate retina and is involved in vision adaptation (Ames and Lim, 2012).

In rod photoreceptors, calcium-activated recoverin associates with rod outer-segment (ROS) disk membranes and inhibits the enzyme rhodopsin kinase. The role of this enzyme is to phosphorylate rhodopsin, the light-sensitive receptor protein found in high amounts in ROS membranes. After absorbing a photon, rhodopsin triggers the visual phototransduction pathway, leading ultimately to the closure of Na^+ and Ca^{2+} channels. This prevents Na^+ and Ca^{2+} from entering the rod cell, and the decreasing Ca^{2+} concentration reduces the release of the neurotransmitter glutamate by the cell, which gives rise to the neural signal. In order to terminate this visual signal or to adapt to a persistent stimulus,

the illuminated rhodopsin molecules must be deactivated and recycled, which involves their phosphorylation by rhodopsin kinase. Mutations in this enzyme cause Oguchi disease (Online Mendelian Inheritance in Man, accessed June 4, 2017), a form of night blindness characterized by abnormally slow dark adaptation. In dark conditions, the intracellular Ca^{2+} concentration increases, and the phosphorylation activity of rhodopsin kinase is inhibited by recoverin, which leads to a prolongation of the lifetime of photoactivated rhodopsin. Thus, recoverin is involved in a calcium-dependent feedback loop modulating the amount of response to a visual stimulus.

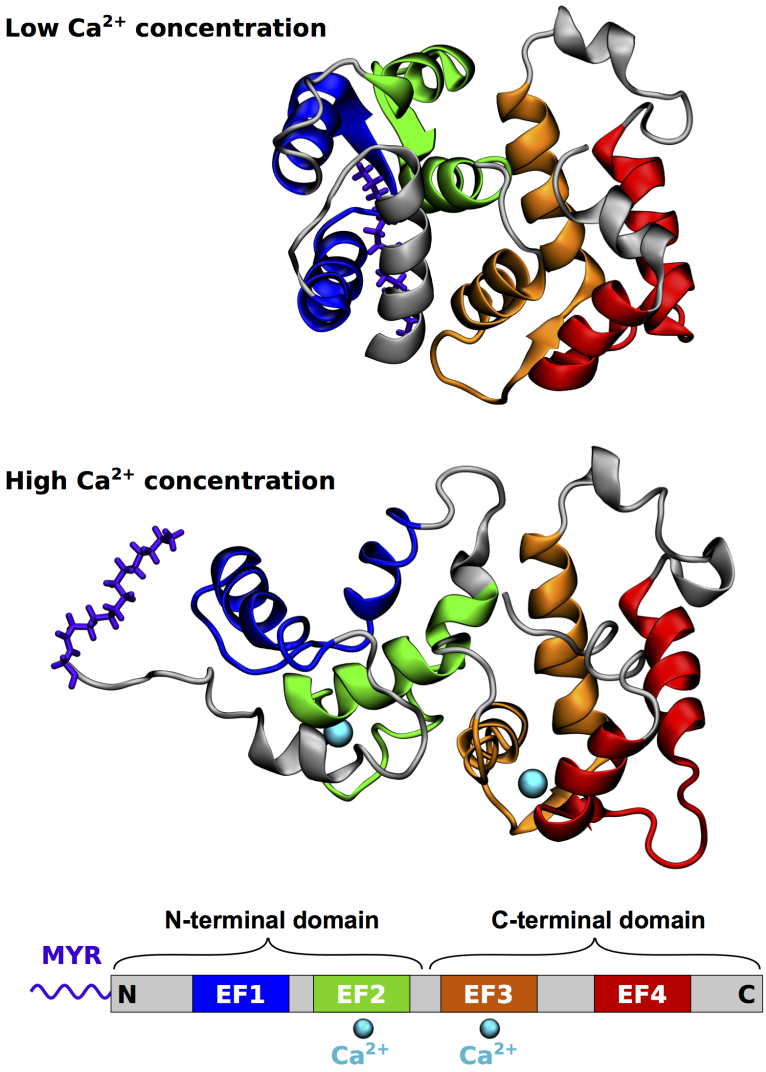

Figure 4.3: Structures of recoverin as obtained from solution NMR measurements. **(Top)** Closed state with no calcium bound (geometry no. 1 of PDB ID 1IKU) (Tanaka et al., 1995). **(Bottom)** Open state with two calcium ions bound (geometry no. 1 of PDB ID 1JSA) (Ames et al., 1997).

The structure of recoverin consists of two domains connected via a flexible linker (Fig. 4.3). Both domains contain two EF hands, evolutionarily-conserved helix–loop–helix motifs shared with the other members of the NCS family. In recoverin, the second and the third EF hand can bind calcium, whereas calcium binding to the remaining two EF hands is blocked owing to inactivating substitutions in their loops. At low intracellular Ca^{2+} concentrations, the two binding sites for calcium are empty, and the myristoyl group of recoverin is sequestered inside the N-terminal domain of the protein, in a cavity formed by five α-helices (Fig. 4.3, top) (Tanaka et al., 1995). When the cytoplasmic Ca^{2+} concentration increases, binding of two Ca^{2+} ions results in a structural rearrangement of the two domains and in the exposure of the myristoyl group to the cytosol (Fig. 4.3, bottom) (Ames et al., 1995, 1997). Moreover, the conformational transition connected with myristoyl extrusion from the hydrophobic core of the protein creates a binding pocket for rhodopsin kinase in the N-terminal domain (Fig. 4.4) (Ames et al., 1997, 2006).

Although recoverin has been the subject of numerous experimental studies, many aspects of its structure and function still remain unclear. Solution NMR structures of myristoylated recoverin were determined both in the closed calcium-free state as well as in the open state with two Ca^{2+} bound (Fig. 4.3) (Tanaka et al., 1995; Ames et al., 1997). However, the exact transition pathway connecting these two end states is not known. Moreover, the structure of the open state was obtained using a more polar oxidized myristoyl analog rather than the true highly nonpolar myristoyl moiety, and the conformation of the last 13 C-terminal amino acid residues was not resolved in the NMR structures (Ames et al., 1997). As for the membrane association of recoverin, binding assays performed both on phospholipid bilayers and monolayers established the importance of the myristoyl moiety for the membrane anchoring (Desmeules et al., 2002; Desbat et al., 2007). However, the membrane insertion of the myristoyl group was inferred only indirectly from NMR order parameters (Valentine et al., 2003). A solid-state NMR study (Valentine et al., 2003) also addressed the orientation of recoverin on a lipid bilayer consisting of 80% di-oleoylphosphatidylcholine (DOPC) and 20% di-oleoylphoshatidylglycerol (DOPG) lipids, concluding that recoverin predominantly adopts a tilted orientation relative to the membrane and suggesting that a patch of positively charged residues near the N-terminus (Fig. 4.4) helps to stabilize the membrane orientation of the protein. A possible modulatory function of the positively charged C-terminus (Fig. 4.4) in the membrane association was also discussed in the literature (Matsuda et al., 1999; Weiergraber et al., 2006; Senin et al., 2007). Altogether, the role of electrostatic interactions in the reversible

membrane binding of recoverin has not been fully resolved yet, with a recent experimental study (Calvez et al., 2016) reporting that the calcium-induced association of recoverin to lipid monolayers requires the presence of negatively charged phosphatidylserine (PS) lipids in the membrane. Finally, it is not clear whether calcium-activated recoverin binds to rhodopsin kinase only after associating with the ROS membrane, or already in the cytoplasm (Ames and Lim, 2012), and whether dimerization of recoverin, reported for high concentrations of the protein ($> 100\,\mu M$) (Myers et al., 2013), affects its membrane binding in *in vivo* conditions.

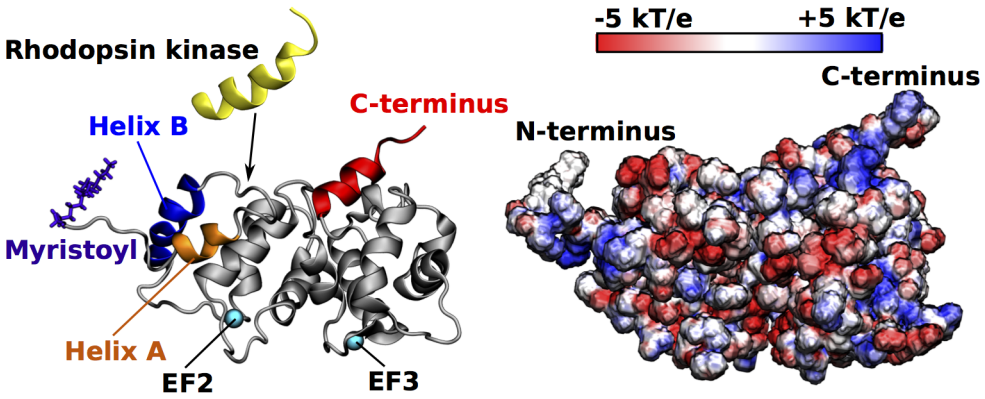

Figure 4.4: Structure and electrostatics of calcium-activated recoverin. **(Left)** Open state binding two Ca^{2+} (geometry no. 1 of PDB ID 1JSA) (Ames et al., 1997). The binding site for rhodopsin kinase (only a 16-residue N-terminal fragment shown) is indicated by a black arrow. The geometry of the last 13 C-terminal residues was transferred from an X-ray crystal structure of non-myristoylated recoverin (PDB ID 1OMR) (Weiergraber et al., 2003). **(Right)** Electrostatic potential mapped on the solvent-accessible surface of the protein, showing patches of positively charged residues at both the N- and C-terminus. The electrostatic potential was calculated for calcium-loaded recoverin immersed in a 150 mM monovalent salt solution, treated implicitly using the nonlinear Poisson-Boltzmann equation (see Section 2.1) in the APBS software (Baker et al., 2001).

4.3 Simulation approach

To elucidate the atomistic details of the membrane binding of calcium-loaded recoverin, we performed a series of all-atom MD simulations of a recoverin molecule in the proximity of a phospholipid bilayer. Moreover, we conducted additional coarse-grained simulations with three different membrane lipid compositions to examine how the membrane association of recoverin is affected by the membrane charge. By using a coarse-grained model, we were able to reach simulation times needed for the sampling of all possible membrane orientations of recoverin, at the

expense of sacrificing atomistic details and the possibility to explore changes in the protein structure.

In our all-atom MD simulations, the simulation box contained a lipid bilayer comprising 190 phospholipids. We chose the same membrane lipid composition as was used in the previous solid-state NMR study (Valentine et al., 2003), i.e., 80% electroneutral DOPC and 20% negatively charged DOPG. This lipid composition, which mimics the charge distribution found in ROS membranes (Fliesler and Anderson, 1983; Wu and Hubbell, 1993), allowed us to directly compare our results with those from experiments. The lipid bilayer was immersed in a 150 mM KCl solution, which served as an approximate model of the intracellular salt solution. We inserted a recoverin molecule to the proximity of the lipid bilayer so that the N-terminal domain was initially facing the membrane surface. We ensured that there was no direct contact between the protein and the lipids in the starting geometry, with the minimum protein–membrane distance being 1 nm. In total, the recoverin–membrane–solvent system consisted of ∼90,000 atoms, and the average size of the unit cell was $8 \times 8 \times 14$ nm.

We obtained the structure of calcium-loaded recoverin from an ensemble of 24 NMR structures of myristoylated bovine recoverin binding two Ca^{2+} (PDB ID 1JSA, structures no. 1 and 8) (Ames et al., 1997). Since the conformation of the last 13 C-terminal residues was not determined by the NMR measurements, we transferred the C-terminal segment (residues 185–202) from an X-ray crystal structure of non-myristoylated recoverin (PDB ID 1OMR) (Weiergraber et al., 2003). Prior to inserting recoverin to the vicinity of the bilayer, we pre-equilibrated the structures of both the protein and the membrane separately in aqueous solutions.

To ensure that our results were robust with respect to the choice of the force field, we performed our atomistic MD simulations using two distinct sets of force-field parameters: CHARMM and AMBER/Slipids. In the former case, we used the CHARMM36 force field (Klauda et al., 2010) to parameterize the lipids and CHARMM22/CMAP (MacKerell et al., 1998, 2004) to describe the protein. In the latter case, we utilized the AMBER ff99SB-ILDN force field (Lindorff-Larsen et al., 2010) for the protein, while the lipids were described with the AMBER-compatible Slipids force field (Jambeck and Lyubartsev, 2012a,b, 2013). In all simulations, water molecules were described with the TIP3P model (Jorgensen et al., 1983), and charges of all K^+, Cl^-, and Ca^{2+} ions were scaled by a factor of 0.75 to account for the electronic polarizability of the surrounding water molecules. This approach, termed the Electronic Continuum Correction (ECC) (Leontyev and Stuchebrukhov, 2011), was shown to reproduce more accurately

the structures of mono- and divalent salt solutions (Kohagen et al., 2014b, 2015) as well as the free energies of calcium binding to the EF hands of another calcium sensor, calmodulin (Kohagen et al., 2014a). In order to avoid affecting the recoverin–membrane interaction by altering the net charge of the calcium-loaded EF loops (EF2 and EF3), we evenly distributed the excess charge of +0.5 e among 10 (or 8) oxygen atoms potentially coordinating the calcium ion in each loop.

The trajectory lengths of our atomistic simulations ranged from several hundreds of ns to two µs. Newton's equations of motion were integrated by employing the leap-frog algorithm (Hockney et al., 1974) with a time step of 2 fs. Long-range electrostatics was calculated with the use of the particle mesh Ewald method (Darden et al., 1993). The temperature of the system was maintained at 310 K using the velocity rescaling thermostat with a stochastic term (Bussi et al., 2007) and the Parrinello–Rahman barostat (Parrinello and Rahman, 1981) was utilized for semi-isotropic pressure coupling with a reference pressure of 1.01 bar.

The coarse-grained system was similar in size to the atomistic system; however, the total number of particles was reduced roughly tenfold owing to the coarse-grained description. We simulated phospholipid bilayers with three different lipid compositions: (1) pure DOPC, (2) 80% DOPC and 20% DOPG, and (3) pure DOPG (see also Fig. 4.2). The whole system was parameterized using the MARTINI force field (Marrink et al., 2007; Monticelli et al., 2008; de Jong et al., 2013; Ingolfsson et al., 2014). To prevent undesired changes in protein structure, we fixed the structure of recoverin using an elastic network model (Periole et al., 2009). The trajectory lengths were 5 µs, which roughly corresponds to 20 µs of realistic time (Monticelli et al., 2008).

Both all-atom and coarse-grained MD simulations were performed using the GROMACS package (Hess et al., 2008; Abraham et al., 2015), and we utilized the VMD program (Humphrey et al., 1996) to visualize the system as well as to prepare figures.

4.4 Results

Our all-atom simulations captured several events of a spontaneous membrane insertion of the myristoyl moiety. In all these cases, after initial reorientation, recoverin approached the lipid bilayer with its N-terminal domain before myristoyl insertion. Once the methyl end of the myristoyl chain reached a suitable gap between lipid head groups, it penetrated the carbonyl region of the bilayer and became accommodated among the acyl chains of the surrounding phospholipids (Fig. 4.5). This process of membrane penetration took 2–9 ns in the individual

runs. Once inserted, the myristoyl group remained membrane-embedded for the 1 µs duration of the simulations.

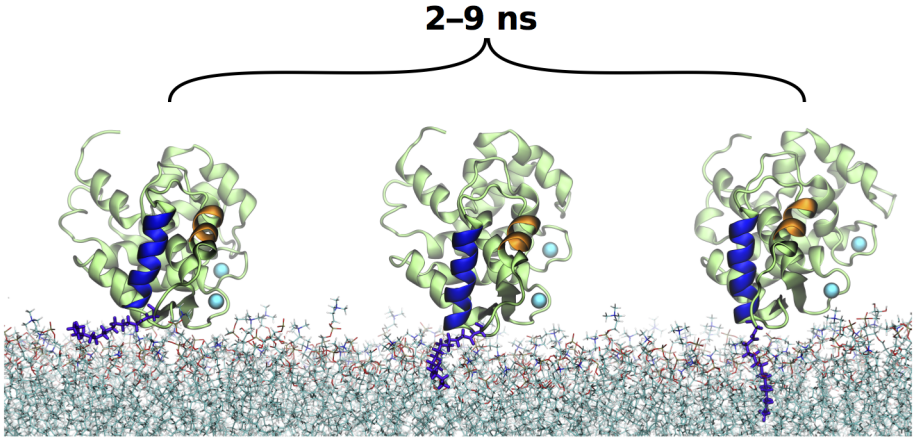

Figure 4.5: Membrane insertion of the myristoyl moiety.

Our simulations also confirmed a critical role of the myristoyl moiety in the membrane association of recoverin. We found that deletion of the myristoyl group from a membrane-anchored geometry of recoverin destabilized the orientation of the protein, ultimately resulting in its complete detachment from the membrane surface. This was further corroborated by our umbrella sampling simulations which revealed that the free-energy preference of the myristoyl moiety for the membrane over the aqueous phase (10 kcal mol^{-1}) is significantly higher than the binding free energy of the unmyristoylated protein (4 kcal mol^{-1}).

In general, we observed that myristoyl insertion occurred providing that two conditions were fulfilled: (1) a favorable orientation of recoverin relative to the membrane and (2) exposure of the myristoyl group to the aqueous environment. In fact, in a number of trajectories, membrane insertion of the myristoyl moiety did not occur. This was either because recoverin approached the lipid bilayer with an unfavorable orientation, interacting with lipid head groups via its positively charged C-terminus, or because the hydrophobic myristoyl moiety moved in-between the amino acid side chains and became shielded from the polar water environment. This move of the myristoyl group was accompanied by structural changes in the N-terminal domain, affecting the conformation of the two N-terminal helices A and B (Fig. 4.7). In particular, the length of helix A changed as well as the angle between helices A and B, and helix B became shifted towards the center of the protein, narrowing the binding pocket for rhodopsin. In contrast, in trajectories featuring myristoyl insertion, a close-to-perpendicular relative orientation of helices A and B kept the myristoyl moiety away from hydrophobic protein residues and maintained the exposure of the myristoyl anchor to the polar aqueous environment. Thus, the conformation of these two helices has to be

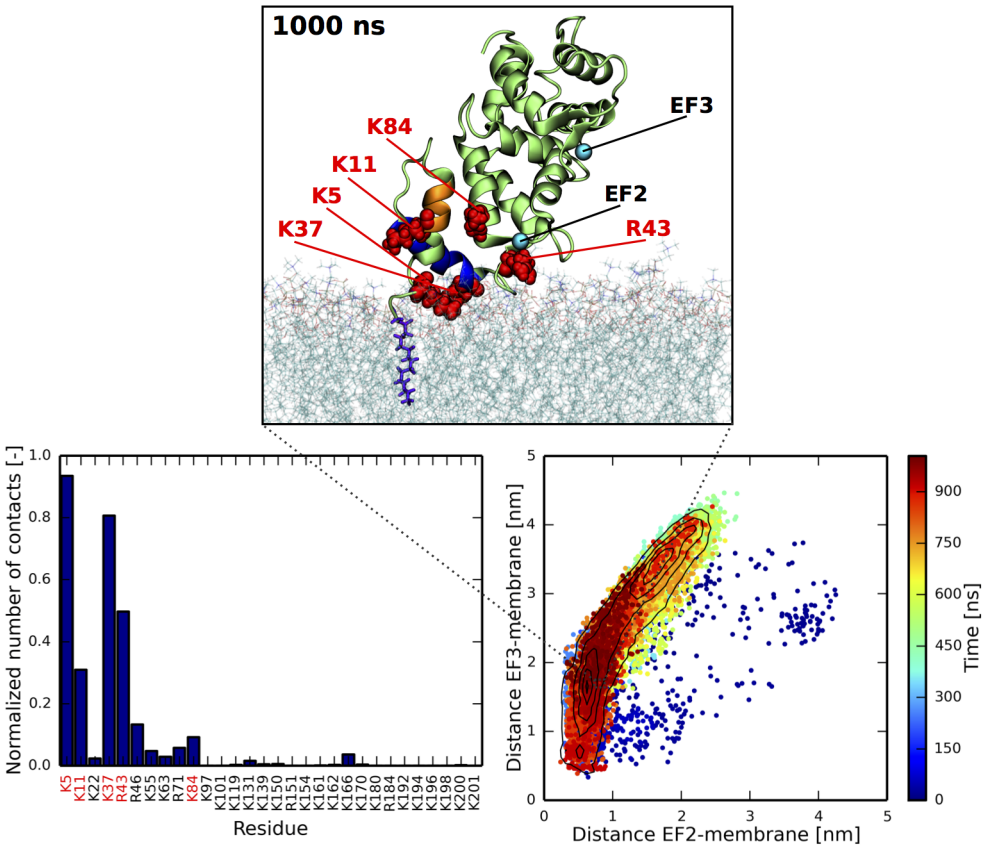

Figure 4.6: Membrane-anchored recoverin in all-atom simulations. **(Top)** A snapshot obtained at the end of a 1 µs trajectory, showing the membrane-embedded myristoyl group (violet) and five positively charged residues (red) reported by previous NMR measurements (Valentine et al., 2003) to be in contact with the membrane. **(Bottom left)** Relative proportions of simulation time that each of the basic residues of recoverin spent in contact with the membrane, i.e., at a distance < 0.6 nm. **(Bottom right)** Membrane orientation of recoverin during a 1 µs trajectory described in terms of the distances of the two calcium ions from the membrane.

stable enough to prevent the hydrophobic myristoyl anchor from returning to the hydrophobic core of recoverin. At the same time, the two helices, forming an important part of the myristoyl switch, have to be sufficiently flexible to allow for the motion of the myristoyl moiety out of the protein core during the calcium-driven conformational transition. Therefore, our simulations indicate that this subtle balance between stability and flexibility is a critical feature determining the efficacy of the calcium–myristoyl switch.

Since the binding pocket for rhodopsin kinase is located in the N-terminal domain and is partially formed by helix B (Fig. 4.4), the presence of a ligand in this binding site could enhance the stability of the N-terminus and, in turn, promote myristoyl exposure. Indeed, our simulation with a 16-residue N-terminal fragment

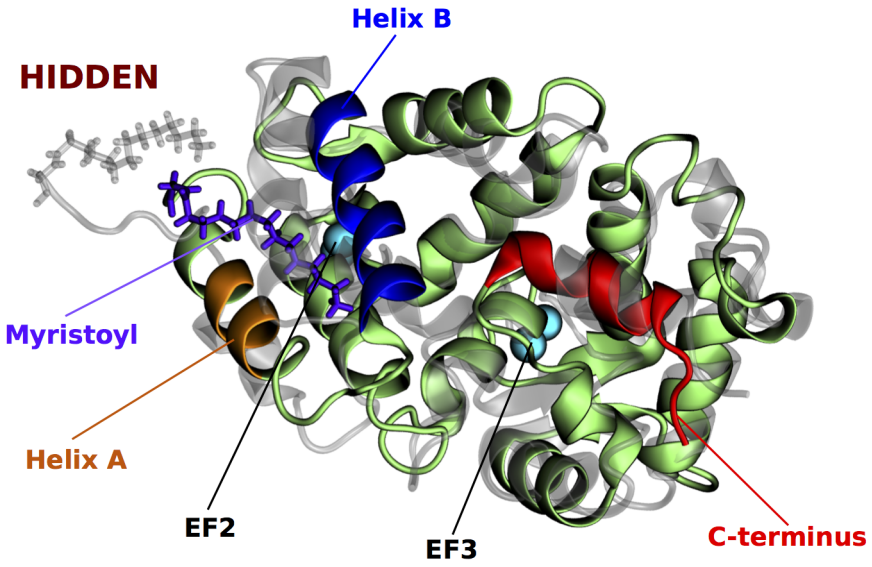

Figure 4.7: An example structure showing the tendency of the hydrophobic myristoyl anchor to move in-between nonpolar side chains. In a number of trajectories, this tendency was accompanied by conformational changes in the N-terminal domain. The initial structure is shown in gray.

of rhodopsin kinase in the binding pocket exhibited an improved stability of the N-terminal domain. Consequently, the myristoyl group remained extruded to the aqueous environment, and it spontaneously became membrane-embedded. This result suggests that the cytoplasmic pre-binding of rhodopsin kinase accelerates the subsequent membrane association of the recoverin–rhodopsin kinase complex. Alternatively, the N-terminal domain could also be transiently stabilized by some more unstructured conformations of the C-terminus, which was reported to be disordered in the solution NMR structures (Tanaka et al., 1995; Ames et al., 1997)

In terms of the orientation of recoverin relative to the membrane, our MD simulations provided a more dynamic picture than the previous solid-state NMR measurements (Valentine et al., 2003). While we found that the tilted orientation of the protein, inferred from the NMR experiments, was indeed prominent (Fig. 4.6); we also observed more parallel orientations of the protein relative to the bilayer, with both calcium-loaded EF hands interacting with lipid head groups. Importantly, we confirmed that the positively charged residues K5, K11, K37, R43, and K84 identified by NMR were in frequent contact with the bilayer during the simulations (Fig. 4.6) and that the binding site for rhodopsin kinase was not blocked by the lipids.

Finally, our coarse-grained MD simulations revealed that the orientation of recoverin toward the membrane markedly depends on the membrane charge (see

Fig. 4.8). While the orientation of recoverin was found to be rather disordered on a DOPC-only membrane, with the binding site for rhodopsin kinase often becoming blocked by the lipids, the presence of a negative charge in the bilayer stabilized a tilted orientation of the protein (Fig. 4.8). Such an orientation, exposing the binding pocket for rhodopsin kinase, agreed with results obtained from atomistic simulations (Fig. 4.6) as well as from the previous solid-state NMR experiments (Valentine et al., 2003). In addition, we occasionally observed an interaction of the C-terminal part with DOPG molecules (Fig. 4.8) of the highly negatively charged membrane, but this interaction had only a transient character. This finding supports the hypothesis that the geometry resulting from interactions mediated by the positively charged C-terminus represents only a local minimum. Taken together, the results of our coarse-grained MD simulations indicate an active role of negatively charged phospholipids in the fine-tuning of the orientation of recoverin toward the membrane. Lipid composition thus may play a significant role in regulating the physiological action of recoverin, i.e., binding of rhodopsin kinase.

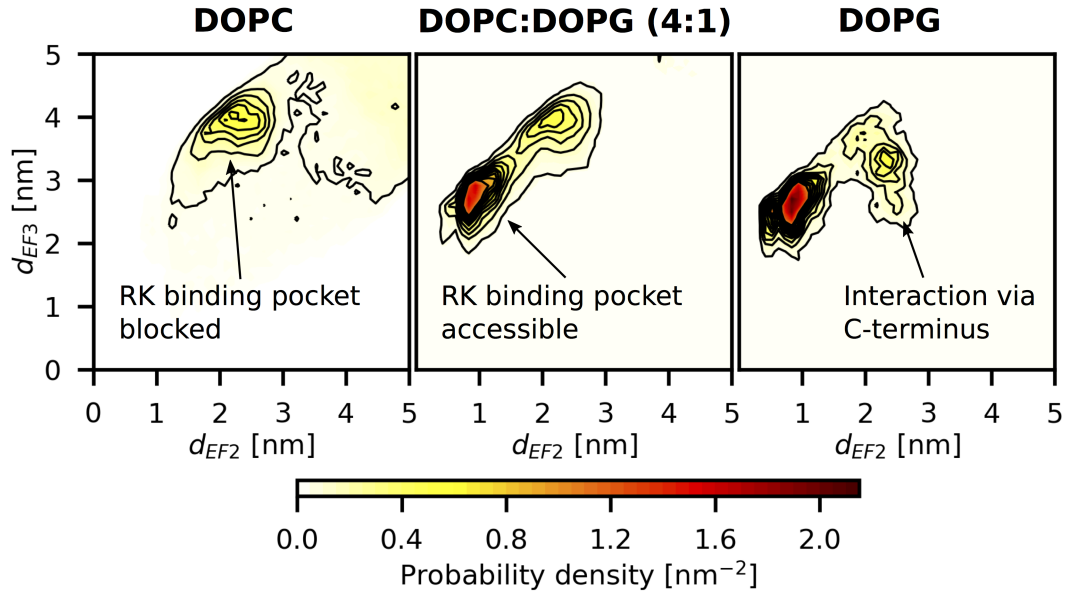

Figure 4.8: Membrane orientation of recoverin as a function of the membrane charge: Probability densities from coarse-grained MD simulations for three different lipid compositions, ranging from the neutral DOPC to the highly negatively charged DOPG. The orientation is expressed in terms of the distances of the two calcium ions from the membrane. Each plot represents an average of three 5 µs coarse-grained MD trajectories.

Chapter 5

Mechanism of the myristoyl switch in recoverin

Calcium-loaded recoverin binds to ROS disk membranes of photoreceptor cells, and we examined atomistic details of its membrane binding in the previous chapter. Here we investigate the process that preconditions the membrane association, i.e., the conformational transition of the myristoyl switch accompanied by calcium binding. We present unpublished results of our MD simulations that provide insights into the structure of an NMR-detected intermediate state (Xu et al., 2011), suggested to be the one to which calcium binds during the conformational transition.

5.1 Conformational transition of recoverin and the role of calcium binding

The extrusion of the myristoyl moiety from a cavity inside the N-terminal domain of recoverin is accompanied by a large-scale conformational change and by the binding of two Ca^{2+} ions to the EF hands 2 and 3. The initial structure of recoverin with no Ca^{2+} bound (called the T state) as well as the final structure binding two Ca^{2+} ions (denoted as the R state) have been determined by solution NMR (Tanaka et al., 1995; Ames et al., 1997) (see Fig. 4.3). These two structures reveal the main features of the conformational transition, in particular, a $\sim 45^{\circ}$ relative rotation of the two domains and structural changes in the N-terminal domain. The domain rotation, characterized by a swiveling motion along the interdomain linker, alters the angle between the exiting helix of EF2 (helix E, see Fig. 5.1 for a definition) and the entering helix of EF3 (helix F), bringing the two Ca^{2+}-binding loops closer to each other. In the N-terminal domain, the

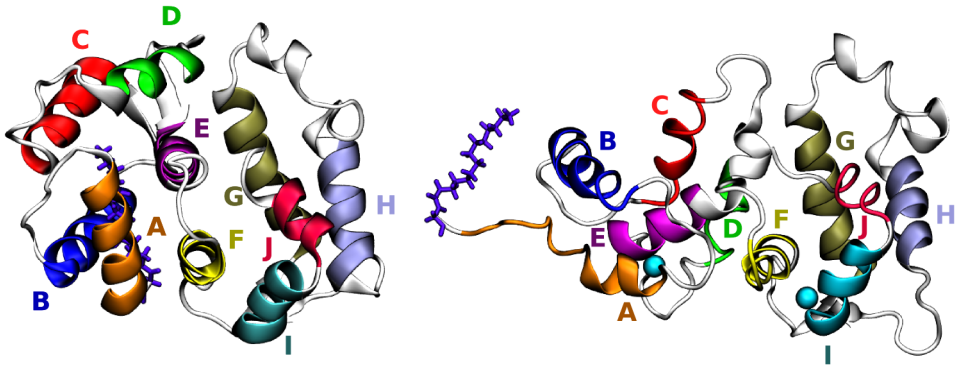

Figure 5.1: The helices of recoverin shown for the closed structure (Tanaka et al., 1995) **(left)** and for the open state (Ames et al., 1997) **(right)**.

entering helix of EF1 (helix B) becomes more perpendicular to the exiting helix (helix C). This, together with a shortening of the N-terminal helix (helix A), promotes the extrusion of of the myristoyl moiety and the formation of a binding pocket for rhodopsin kinase. Another notable feature is the conformational change induced in EF2 and EF3 by calcium binding. Namely, the presence of a Ca^{2+} ion alters the shape of the EF loop and makes the two helices of the EF hand more perpendicular relative to each other (Fig. 5.2).

While the two available NMR structures provide important information on the conformational transition from the closed, myristoyl-sequestering T state to the open, myristoyl-exposing R state, the actual transition pathway is not known. A key question is the exact points along the transition path at which the two Ca^{2+} ions bind to the protein. It was established that EF3 has a higher affinity for calcium than EF2 (with their dissociation constants being 0.11 µM and 6.9 µM, respectively) and that Ca^{2+} binding is cooperative in myristoylated recoverin (Ames et al., 1995; Baldwin and Ames, 1998; Permyakov et al., 2000). As a result, it was proposed that a Ca^{2+} ion first binds to EF3, inducing a conformational transition which in turn facilitates subsequent Ca^{2+} binding to EF2 (Permyakov et al., 2000).

This hypothesis of a structural intermediate was supported by a solution NMR structure (PDB ID 1LA3) (Ames et al., 2002), which has a mutation in the EF2 loop (glutamate 85 replaced with a glutamine), preventing it from Ca^{2+} binding. As a consequence, the NMR structure, obtained at a high concentration of Ca^{2+}, only contains a single Ca^{2+} ion, which is bound to EF3. The two domains of this mutant structure (see Fig. 5.3) are rotated similarly to those of the fully Ca^{2+}-loaded structure (Fig. 4.3); however, the myristoyl moiety is still hidden inside

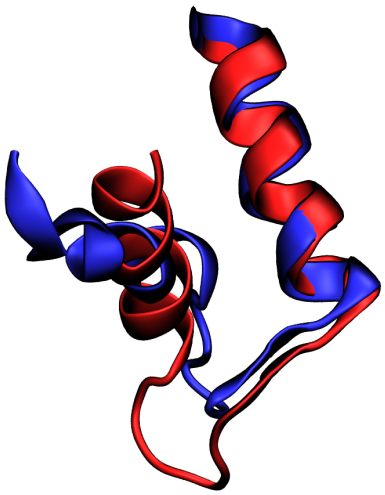

Figure 5.2: Overlaid structures of EF3 without (red) and with calcium (blue). The Ca^{2+}-free structure comes from PDB ID 1IKU (structure no. 1) (Tanaka et al., 1995), and the Ca^{2+}-binding structure originates from PDB ID 1JSA (structure no. 1) (Ames et al., 1997).

the N-terminal domain, which resembles that of Ca^{2+}-free recoverin. Therefore, this E85Q mutant loaded with a single Ca^{2+} ion was suggested to represent a structural intermediate of the transition pathway (Ames et al., 2002).

More recent measurements of ^{15}N NMR relaxation dispersion (Xu et al., 2011) revealed that recoverin undergoes millisecond conformational dynamics even in the absence of Ca^{2+} in the solution. The relaxation dispersion measurements pointed to the existence of a minor population of structures (> 1 %) distinct from the T state and coexisting with T even in a Ca^{2+}-free solution. The signal from this minor species became stronger when a trace amount of Ca^{2+} was added, indicating that the species represents an intermediate state (I) along the myristoyl-switch pathway. This led Xu et al. (2011) to the formulation of a three-state model involving states T, I, and R (Fig. 5.4). By considering also the results of previous NMR experiments and Ca^{2+}-binding assays, Xu et al. (2011) concluded that the most likely transition pathway starts with a conformational transition from T to I, which is followed by the binding of two Ca^{2+} ions to I. Finally, after these two Ca^{2+}-binding events, recoverin loaded with two Ca^{2+} ions proceeds from I to R. Thus, the I state, despite being short-lived, forms a crucial element of the transition pathway, and the knowledge of its structure is critical for understanding the mechanism of the Ca^{2+}-induced myristoyl switch.

The exact structure of the I state could not be determined from the NMR measurements owing to its short-lived nature. Nevertheless, the positioning of residues undergoing chemical exchange (Fig. 5.5) strongly suggests that the T $\rightarrow$ I

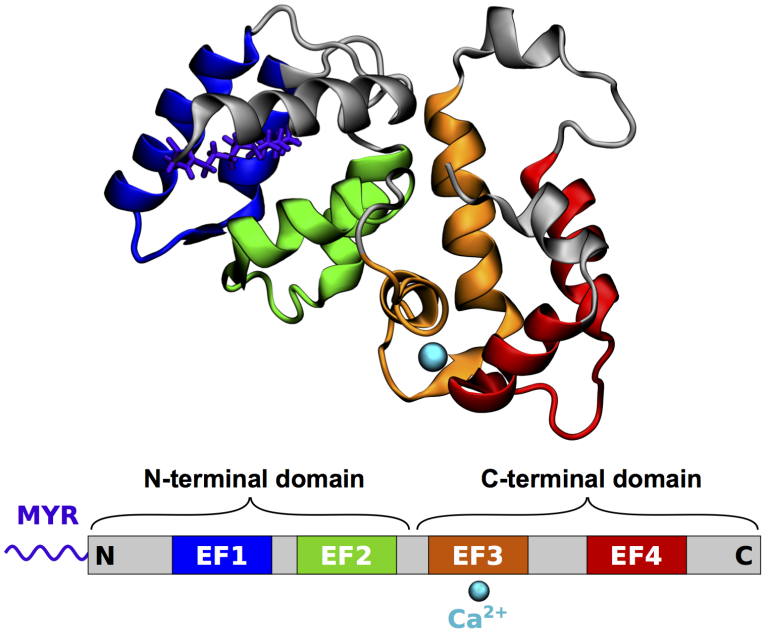

Figure 5.3: Structure of the E85Q recoverin mutant containing a single Ca^{2+} ion (Ames et al., 2002).

transition involves some rotation of the two protein domains. On the other hand, the myristoyl group in the I state still appears to be hidden inside the N-terminal domain (Xu et al., 2011). Therefore, the I state may be similar to the E85Q mutant.

The three-state model of Xu et al. (2011) assumes that Ca^{2+} binding to T, I, and R only tilts the relative energetics of those states but does not significantly perturb their structures. This assumption may be over-simplified, and while the structure of the E85Q mutant may faithfully represent I^1, i.e., the intermediate state containing one Ca^{2+} ion, it might not necessarily correspond to the I^0 state with no calcium. Here our goal was to shed more light on the conformation of the I^0 state, which is supposed to co-exist in a fast conformational equilibrium with T^0 and which should be the primary target for calcium binding upon an increase in the cytoplasmic Ca^{2+} concentration. To this end, we performed direct MD and REST2 simulations of a semi-open Ca^{2+}-free structure derived from the E85Q mutant. For a comparison, we first conducted MD simulations of a semi-open Ca^{2+}-containing state based on the E85Q structure and of the closed Ca^{2+}-free state structurally characterized by NMR (Tanaka et al., 1995).

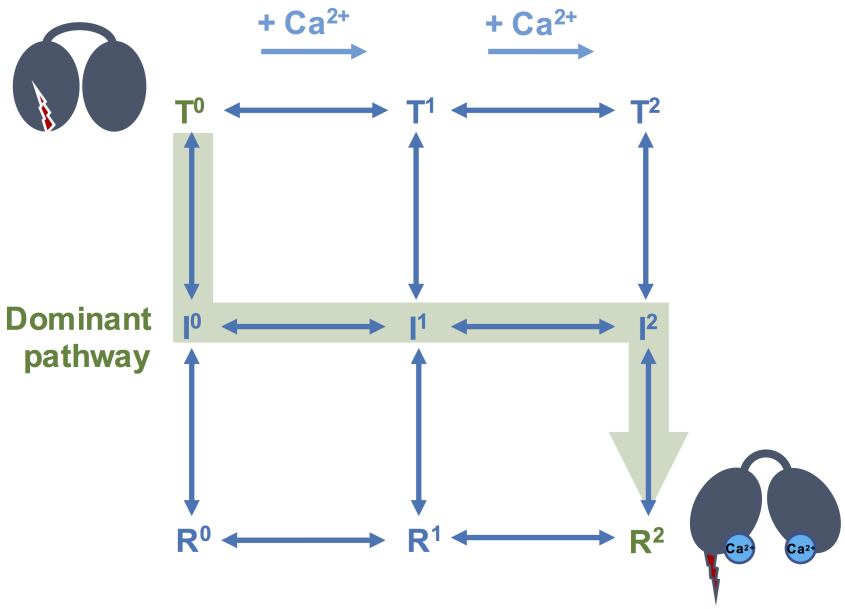

Figure 5.4: A three-state model of the Ca^{2+}-induced myristoyl switch of recoverin, involving the closed T state, the intermediate I state, and the open R state. The superscript indicates the number of Ca^{2+} ions bound to the respective state. According to Xu et al. (2011), Ca^{2+} binding occurs predominantly in I, which undergoes millisecond exchange with T even at 0% Ca^{2+} concentration.

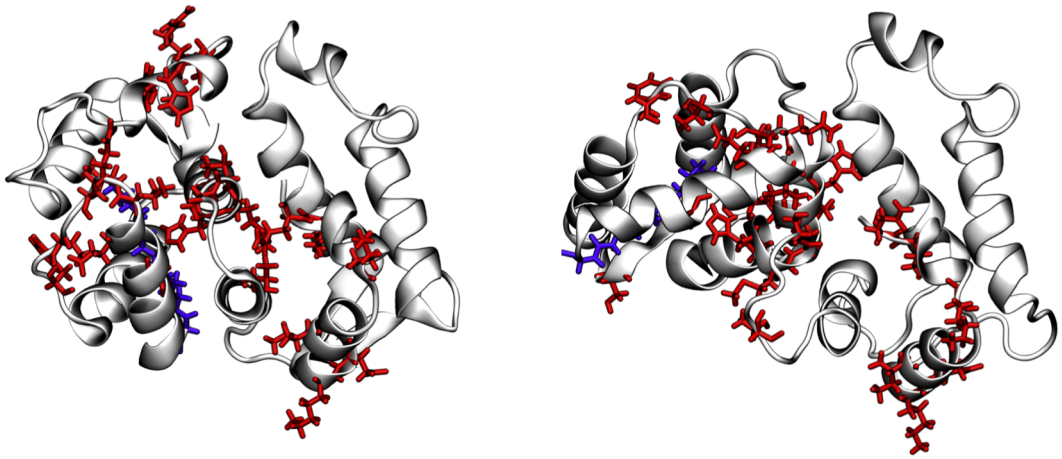

S10, E15, L17, Q18, L19, T21, F23, S41, H68, F70, R71, A75, D78, H91, M92, T93, S94, T98, K170, E171, I173, K180, I186, Q187

Figure 5.5: Residues of recoverin exhibiting relaxation dispersion at 0% Ca^{2+} concentration (Xu et al., 2011), shown for the closed structure (Tanaka et al., 1995) **(left)** and for the semi-open E85Q mutant (Ames et al., 2002) **(right)**. Relaxation dispersion is indicative of conformational exchange on the millisecond time scale, and the positioning of the residues suggests that this exchange involves domain rotation.

5.2 Simulation approach

We used a solution NMR structure of the E85Q mutant (PDB ID 1LA3, structure no. 1) (Ames et al., 2002) after a backmutation as a starting point for our simulations of the semi-open state. The additional simulation of the closed Ca^{2+}-free state was started from a structure obtained from NMR measurements at zero Ca^{2+} concentration (PDB ID 1IKU, structure no. 1) (Tanaka et al., 1995). It should be noted that neither of these NMR structures contained the C-terminal segment (residues 190–202) as its conformation was not resolved in the NMR experiments. However, the absence of the C-terminal segment should not have any substantial impact on the mechanism of the conformational transition since the Ca^{2+}-induced myristoyl switch was shown experimentally to be functional even for a C-terminally truncated recoverin construct (Weiergraber et al., 2006). Therefore, considering the likely disordered state of the C-terminal segment and the resulting uncertainty in its position and conformation, we decided to omit it from the present simulations. We placed each of the protein structures in a cubic box with a size of ∼8.5 nm, and we filled the box with a 150 mM KCl solution containing ∼18,400 water molecules and including additional K^+ ions to neutralize the system. In total, both systems each contained ∼58,000 atoms.

Analogously to some of our recoverin–membrane simulations, we described the protein with the AMBER ff99SB-ILDN force field (Lindorff-Larsen et al., 2010) and water molecules with the TIP3P model (Jorgensen et al., 1983). In the same way as in the recoverin–membrane simulations, we also treated charges of all K^+, Cl^-, and Ca^{2+} ions via the ECC scheme (Leontyev and Stuchebrukhov, 2011; Kohagen et al., 2014b, 2015).

The MD simulations were performed using the GROMACS 5.1.2 package (Abraham et al., 2015). Newton's equations of motion were integrated by employing the leap-frog algorithm (Hockney et al., 1974) with a time step of 2 fs. The trajectory frames were recorded every 2 ps. A cutoff of 1.2 nm was applied to short-range electrostatic interactions while long-range electrostatics was calculated using the particle mesh Ewald method (Darden et al., 1993). Van der Waals interactions were truncated at 1.2 nm. Covalent bonds containing hydrogen atoms were constrained by the LINCS algorithm (Hess et al., 1997), and water molecules were held rigid by the SETTLE algorithm (Miyamoto and Kollman, 1992). The temperature of the system was maintained at 310 K by the velocity rescaling thermostat with a stochastic term (Bussi et al., 2007), and the Parrinello–Rahman barostat (Parrinello and Rahman, 1981) was used with a time constant of 10 ps to keep the system pressure at 1.01 bar. Before the actual production simulations,

the maximum forces were decreased below 1000 kJ mol nm^{-1} using the steepest-descent algorithm, and a sequence of three relaxation runs was performed: (1) a 100 ps simulation with all heavy atoms of the protein restrained and a time step of 1 fs, (2) a 1 ns run with all heavy atoms of the protein restrained and with a 2 fs time step, and (3) a 25 ns run with restraints placed on the Cα atoms of the protein backbone and with a 2 fs time step. In all three relaxation steps, the force constant of the harmonic restraints was 1000 kJ mol nm^{-2}, and the Berendsen barostat (Berendsen et al., 1984) with a coupling constant of 1 ps was used. The first 100 ns of the production trajectories were not used for structure analysis.

Apart from the direct MD simulations, we also conducted a REST2 simulation (Wang et al., 2011) of the semi-open state lacking Ca^{2+}, with the EF3 loop (residues 110–121) forming the solute, i.e., the effectively heated part of the system. The REST2 simulation was performed in the GROMACS 5.1.4 software (Abraham et al., 2015) patched with the PLUMED 2.3.0 package (Tribello et al., 2014). The simulation was started from the same structure as the production run of the Ca^{2+}-binding semi-open state, but with the Ca^{2+} cation deleted from EF3. A total of 13 replicas of the system were simulated at 310 K with effective solute temperatures ranging from 310 K to 900 K (see Table 5.1) and with exchanges of replicas being attempted every 2 ps. Results were analyzed for the lowest effective solute temperature, sampling the statistical ensemble of interest. The first 100 ns of the production trajectory were not used for the analysis.

T_0	T_1	T_2	T_3	T_4	T_5	T_6	T_7	T_8	T_9	T_{10}	T_{11}	T_{12}
310	339	370	405	442	483	528	577	631	689	754	824	900

Table 5.1: Solute temperatures [K] used in the REST2 simulation of recoverin.

5.3 MD of semi-open and closed states

Our microsecond trajectories of the semi-open state binding a Ca^{2+} ion as well as of the Ca^{2+}-free closed state revealed no dramatic changes in the overall protein structure. For both states, the root-mean-square deviation (RMSD) of the Cα backbone atoms from the initial structure stabilized around 0.4 nm (Fig. 5.6). This somewhat higher value may be due to the rather low quality of the two starting NMR structures, as determined by the wwPDB validation (Berman et al., 2003), or due to the absence of the last 13 C-terminal residues, which may have a stabilizing effect on the protein structure. Nevertheless, in both trajectories, recoverin retained its overall conformation, as was also documented by

a generally good agreement between calculated and experimentally-determined chemical shifts (see Figs. B.1 and B.2 in Appendix B).

In both simulations, the N-terminal domain, sequestering the myristoyl group, appeared less stable than the C-terminal domain. In particular, in the semi-open state, the N-terminal helix A became significantly shorter in the course of the trajectory as compared to the initial structure and also in comparison to the closed state (see Fig. 5.7). While this destabilization may have been partly overestimated by the particular force-field description, the result clearly demonstrates that the domain rotation lowers the stability of the N-terminus, facilitating the extrusion of the myristoyl moiety, as predicted by Ames et al. (2002). In addition, within tens of nanoseconds after the start of the simulation of the semi-open state, the flexible interdomain linker changed its conformation, becoming more S-shaped. Similarly, helix D in the closed-state structure became temporarily destabilized during the initial 100 ns, and it also moved farther away from the C-terminal domain. Such a motion of helix D and potentially also its partial unfolding may accompany the rotation of the two domains and allow this helix to avoid clashing with helix G of the C-domain (see Fig. 5.1).

Not surprisingly, the two simulations also differed in the conformation of the EF3 loop, which contained a Ca^{2+} ion in the semi-open state. The presence of the cation made the EF3 loop significantly more compact, as expressed by the average radius of gyration of its atoms, which equaled 0.65 nm (standard deviation = 0.02 nm) for the semi-open state and 0.83 nm (standard deviation = 0.04 nm) for the Ca^{2+}-free state.

To test the effect of Ca^{2+} on the conformation of the semi-open state, we repeated the corresponding simulation after deleting the Ca^{2+} ion from EF3. We found that the removal of the cation resulted in a restructuring of the EF3 loop, which translated into a conformational change of the whole EF hand, and ultimately, into a substantial relative rotation of the two protein domains (see Figs. 5.8 and 5.9). The domain rotation was mediated by the interaction of the EF2 and EF3 loops, with the more disordered EF3 loop pushing against the neighboring EF2 loop. Taken together, this MD trajectory indicates that the conformation of the EF3 loop, altered by the presence or absence of a Ca^{2+} ion, has a considerable effect on the overall structure of the intermediate state.

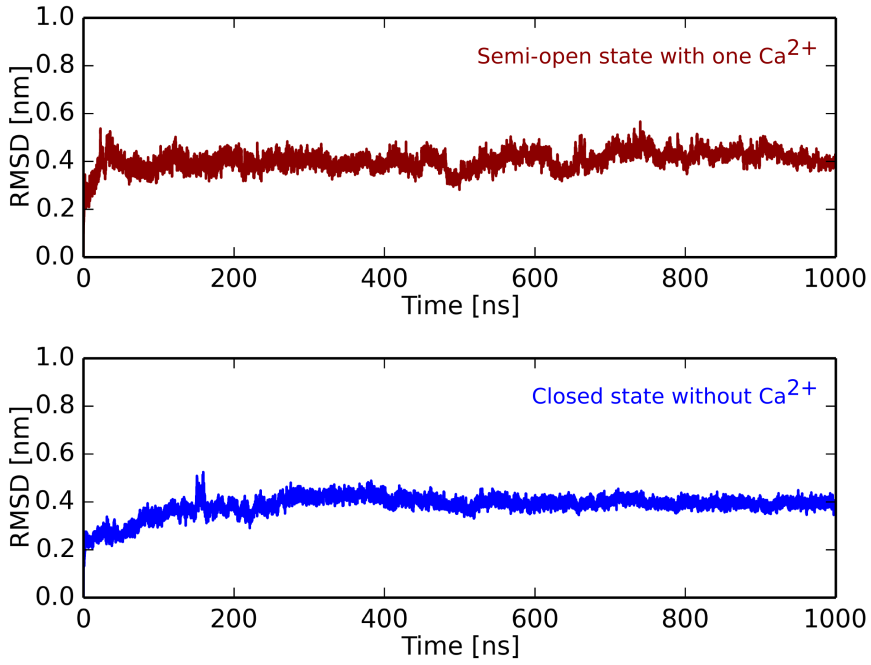

Figure 5.6: Cα RMSD from the initial structure during a 1 µs trajectory of the semi-open state loaded with one Ca^{2+} ion and during a 1 µs trajectory of the closed state without Ca^{2+}.

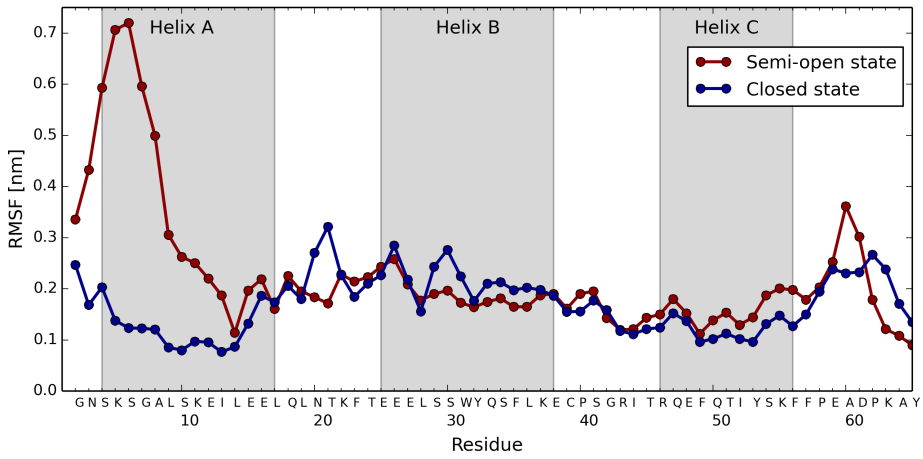

Figure 5.7: The N-terminus becomes destabilized owing to the domain rotation. A comparison of the root-mean-square fluctuations (RMSF) of Cα atoms in a 1 µs trajectory of the semi-open state binding one Ca^{2+} ion and in a 1 µs trajectory of the closed Ca^{2+}-free state of recoverin. RMSF values for all recoverin residues can be found in Appendix B (Fig. B.3).

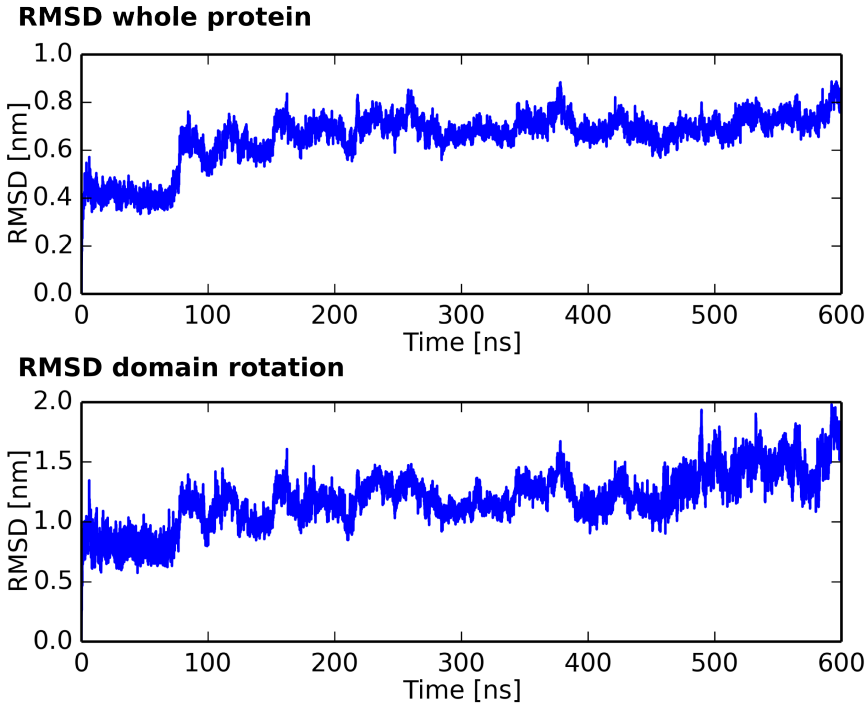

Figure 5.8: Cα RMSD of the semi-open state after removing the Ca^{2+} ion bound in EF3. **(Top)** Cα RMSD calculated for the whole protein after its alignment to the starting structure, **(bottom)** Cα RMSD evaluated for the N-terminal domain (residues 2–91) after an alignment of the C-terminal domain (more specifically, residues 122–189) to the initial structure.

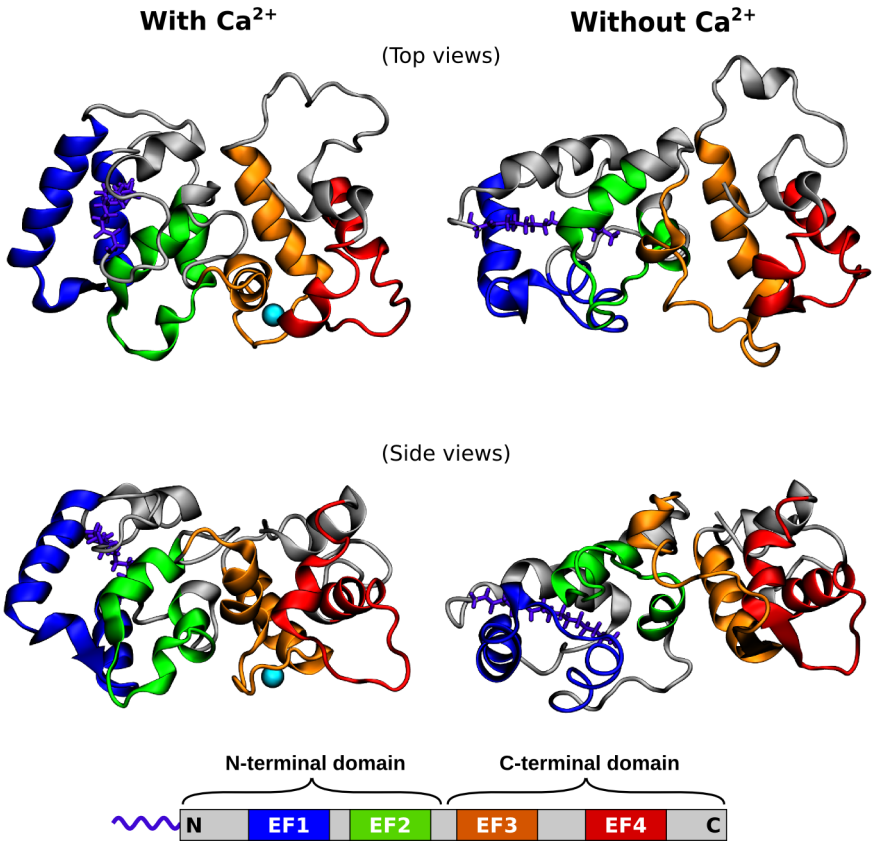

Figure 5.9: Effect of Ca^{2+} removal on the structure of the semi-open state. A comparison of a recoverin structure at the end of a 1 µs trajectory with a Ca^{2+} ion bound in EF3 **(left)** and at the end of a 600 ns trajectory without Ca^{2+} **(right)**. The C-domain residues 122–189 are superimposed for both structures.

5.4 REST2 simulation of the semi-open state without calcium

To further explore the allosteric effect of the EF3 loop on the structure of the protein, we performed a REST2 simulation selectively heating up the atoms of the EF3 loop with the goal to enhance the sampling of its conformations. The average transition probabilities during the 560 ns simulation ranged from 0.21 to 0.36 for the neighboring pairs of effective solute temperatures. Importantly, the lowest effective solute temperature was frequently visited by replica geometries that had spent portions of their time in the high temperature range (see Fig. 5.10).

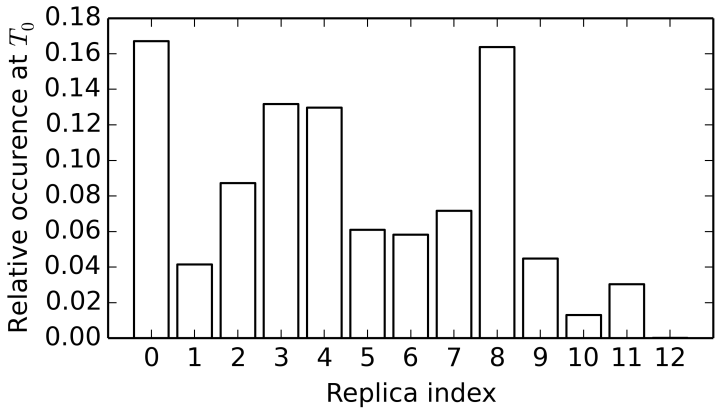

Figure 5.10: Occurrence of replicas at the lowest temperature T_0.

We found that the absence of a Ca^{2+} ion from EF3 expanded the structure of the EF3 loop, as measured by its radius of gyration, which was equal on average to 0.76 nm with a standard deviation of 0.06 nm. Thus, the average radius of gyration moved toward values typical of the Ca^{2+}-free closed state of the protein (see Section 5.3). Moreover, without Ca^{2+}, recoverin displayed significantly increased structural variation as compared to the simulation with Ca^{2+}. This effect was particularly pronounced in the region of the EF hands 3 and 2, as well as in the interdomain linker (see Fig. 5.11).

The increased structural variation of the semi-open state lacking Ca^{2+} was also reflected by a significantly extended range of relative orientations of the two protein domains (Fig. 5.12). While some structures resembled those sampled with a Ca^{2+} ion bound in EF3, others featured markedly different conformations of the EF hand 3 and, in turn, different rotations of the two domains (see Fig. 5.13). This also affected the position and conformation of the EF2 loop, which became displaced owing to its interactions with the disordered neighboring EF3 loop.

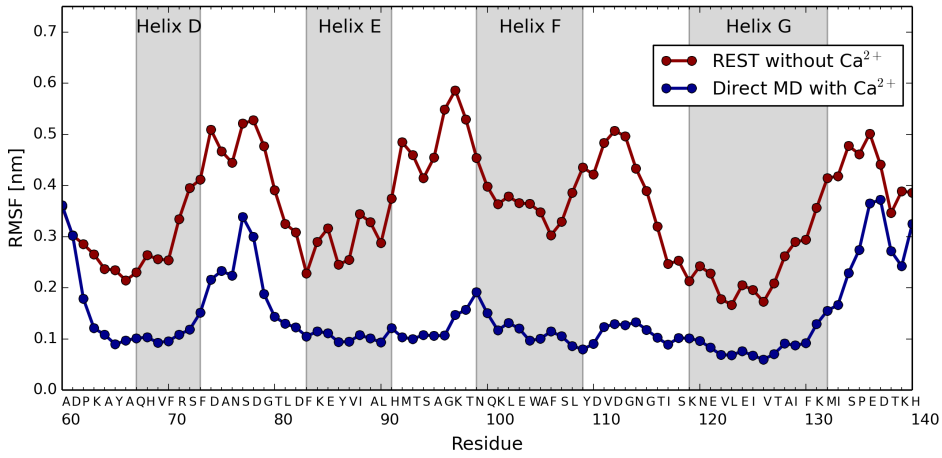

Figure 5.11: The REST2 simulation shows increased structural variation in the semi-open state of recoverin without Ca^{2+}. A comparison of the Cα RMSF values for the lowest temperature of a 560 ns REST2 simulation and for a 1 µs trajectory of the semi-open state binding one Ca^{2+} ion. RMSF values for all recoverin residues can be found in Appendix B (Fig. B.4).

Thus, the present results, in combination with the available NMR data and the results of Ca^{2+} binding assays, offer a more detailed picture of the Ca^{2+}-induced myristoyl switch: Even at low Ca^{2+} concentrations, recoverin oscillates between its closed state and a semi-open state. This state, however, is not structurally uniform, but rather, it exhibits a relatively broad range of domain orientations and conformations of the EF hands 3 and 2. Calcium binding to EF3 stabilizes a compact conformation of EF3, thereby making also the relative orientation of the two protein domains more stable and allowing the adjacent EF2 loop to adopt a position and conformation favorable to Ca^{2+} binding. The binding of this second Ca^{2+} ion promotes a conformational change in the N-terminal domain which ultimately leads to an extrusion of the myristoyl moiety from inside the protein.

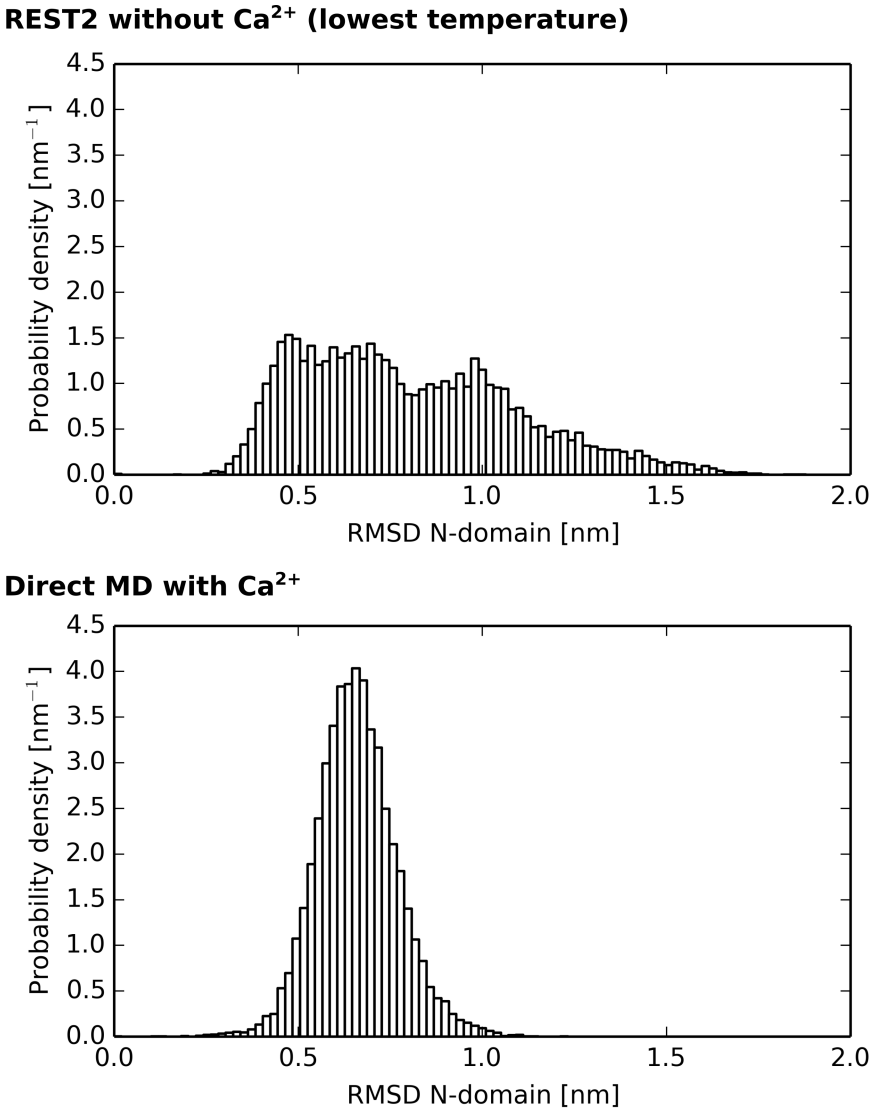

Figure 5.12: The absence of Ca^{2+} from EF3 translates into domain rotation. Histograms of Cα RMSD in the REST2 simulation without Ca^{2+} **(top)** and in direct MD with Ca^{2+} **(bottom)**, calculated for the N-terminal domain (residues 2–91) after an alignment of the C-terminal domain (residues 122–189) to the initial structure.

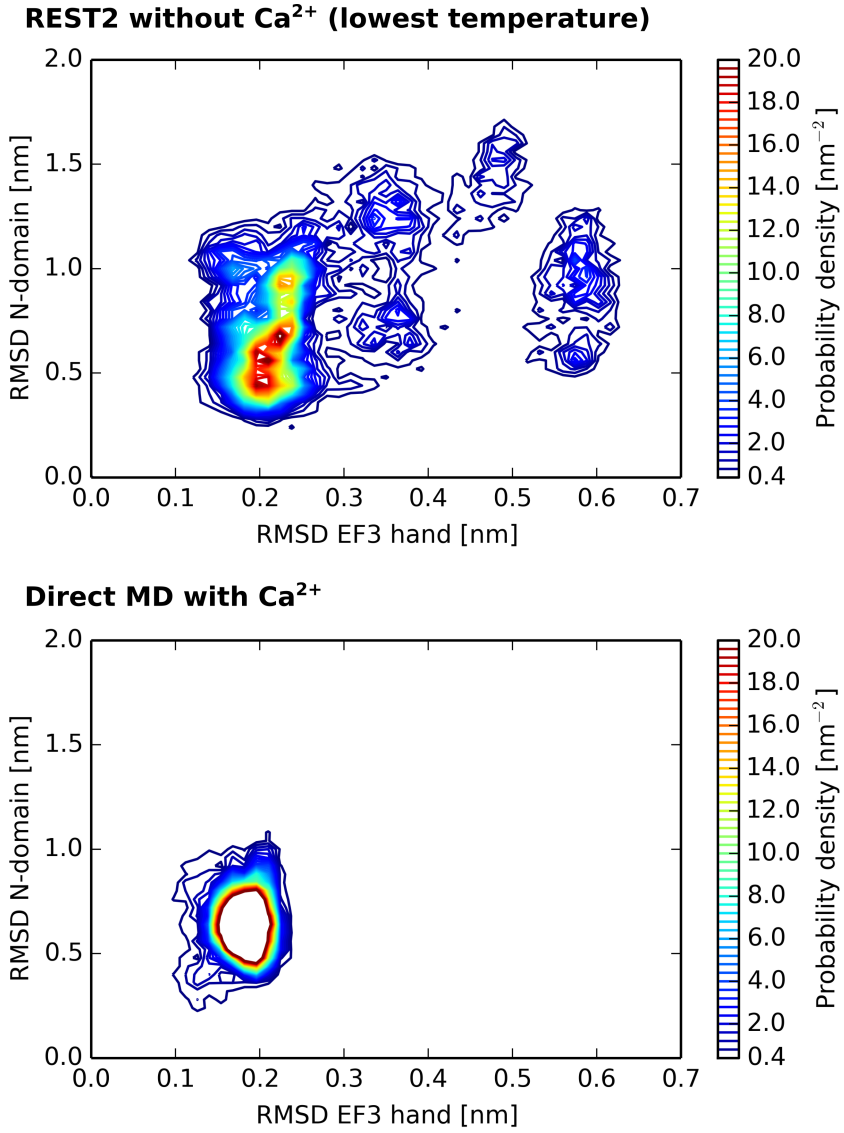

Figure 5.13: Without Ca^{2+} in EF3, the semi-open state of recoverin samples a broad range of EF3 hand conformations and domain orientations. 2D histograms showing the correlation between the Cα RMSD of the EF hand 3 (residues 99–132) from its initial structure and the Cα RMSD of the N-terminal domain (residues 2–91) after an alignment of the C-terminal domain (residues 122–189) to the initial structure. A comparison of results from the REST2 simulation without Ca^{2+} **(top)** and from direct MD with Ca^{2+} **(bottom)**.

5.5 A side note: Description of calcium binding

A full computational characterization of the calcium-induced myristoyl switch will require further simulations of the transition pathway and calculations of the associated free energies. Moreover, accurate calculations of the Ca^{2+} binding free energies are needed for an evaluation of how conformational changes in the protein modulate its affinity for Ca^{2+}. This necessitates a faithful description of the interaction between calcium and the amino acid residues comprising the EF loops. In particular, a proper description of the interaction of Ca^{2+} with the carboxylic groups of aspartate and glutamate is essential since these negatively charged residues are especially important for the coordination of Ca^{2+} in the EF loop.

Being a divalent cation, Ca^{2+} can strongly polarize surrounding molecules. This electronic polarization is not explicitly accounted for in classical nonpolarizable MD, which can lead to significant overestimation of Ca^{2+} binding energies. As a remedy, the ECC scheme was proposed (Leontyev and Stuchebrukhov, 2011). This approach consists in rescaling ionic charges by the inverse square-root of the electronic part of the solvent relative permittivity, i.e., by a factor of approximately 0.75 for water. For a concentrated aqueous solution of calcium chloride, a comparison of MD simulations with results of neutron scattering experiments showed that the ECC scheme correctly describes the structure of the solution, in stark contrast with the full-charge approach (Kohagen et al., 2014b).

We made a similar comparison of MD simulations and neutron scattering measurements for a 1 molal solution of calcium acetate, serving as a proxy for examining the interaction of Ca^{2+} with the carboxylic groups of aspartate and glutamate. The simulation box contained 81 calcium ions, 162 acetate ions, and 4581 water molecules. We parameterized the acetate anion using the AMBER ff99 force field (Wang et al., 2000), with partial charges obtained from a RESP fit (Wang et al., 2000) to the electrostatic potential of an optimized geometry of acetate. We employed the Hartree-Fock method with the 6-31G* basis set (Petersson and Allaham, 1991) in the Gaussian 09 program (Frisch et al., 2009) for geometry optimization as well as for electrostatic potential calculation. The resulting RESP charges are listed in Table 5.2. Calcium was described using a parameter set involving the ECC correction (Kohagen et al., 2014b), and, for a comparison, also using a full-charge parameterization (Oostenbrink et al., 2004). Finally, water molecules were described with the SPC/E model (Berendsen et al., 1987). Newton's equations of motion were integrated using the leap frog algorithm (Hockney et al., 1974) with a time step of 1 fs. Bonds with hydrogen atoms of

acetate molecules were held fixed by the LINCS algorithm (Hess et al., 1997), while the geometries of water molecules were kept rigid using the SETTLE algorithm (Miyamoto and Kollman, 1992). Short-range electrostatic and van der Waals interactions were truncated at 12 Å, and long-range electrostatic interactions were calculated by employing the particle mesh Ewald method (Darden et al., 1993). The system was coupled to a velocity rescaling thermostat with a stochastic term (Bussi et al., 2007), maintaining a constant temperature of 300 K with a coupling constant of 0.5 ps. After initial energy minimization and a 1 ns pre-equilibration run performed in the NpT ensemble with the pressure kept at 1 bar by the Berendsen barostat (Berendsen et al., 1984), a 100 ns production run was performed in the same ensemble and with the same reference pressure utilizing the Parrinello-Rahman barostat (Parrinello and Rahman, 1981). In both cases, the coupling constant of the barostat was set to 1 ps. The final 25 ns of the production trajectory were used for structure analysis.

Atom	Atom type	RESP charge [e]	RESP charge (scaled) [e]
C1	C	0.886	0.665
O1	O2	-0.841	-0.631
O2	O2	-0.841	-0.631
C2	CT	-0.222	-0.167
H1	HC	0.006	0.005
H2	HC	0.006	0.005
H3	HC	0.006	0.005

Table 5.2: Partial charges on acetate.

The results of the MD simulations were compared with experimental data obtained, with the assistance of the author of this thesis, from neutron diffraction with hydrogen/deuterium isotopic substitution. Briefly, scattering patterns were measured for a total of four structurally-identical 1 molal calcium acetate solutions: $Ca(CH_3COO)_2$ in H_2O, $Ca(CD_3COO)_2$ in H_2O, $Ca(CH_3COO)_2$ in D_2O, and $Ca(CD_3COO)_2$ in D_2O. By subtracting first the scattering patterns for each pair of solutions sharing the same solvent and then calculating the difference of the two results, a second-order difference $\Delta\Delta S(Q)$ was obtained. This second-order difference contains information on the correlation between hydrogen atoms of methyl groups and exchangeable hydrogen atoms of water molecules. Since the structure of water around an acetate anion is affected by the presence or absence of Ca^{2+}, $\Delta\Delta S(Q)$ can sensitively report on ion pairing. When Fourier-transformed to real space as $\Delta\Delta G(r)$, the second-order difference is proportional

to the pair correlation function $g_{\mathrm{HsubHex}}(r)$ of exchangeable and non-exchangeable hydrogen atoms (i.e., those in water molecules versus those in methyl groups) as (Neilson et al., 2001)

$$\Delta\Delta G(r) = 43.17\, g_{\mathrm{HsubHex}}(r) \tag{5.1}$$

In this way, experimental data from neutron scattering measurements can be directly compared with results obtained from MD simulations.

Essentially, our comparison of MD simulations with neutron scattering data revealed that a good agreement with experiments is only obtained upon scaling charges of both Ca^{2+} and the acetate anion. Regardless of whether the charge on Ca^{2+} was scaled or not, our simulations with full charges on acetate showed strong clustering of ion pairs, which was not observed in experiments (Fig. 5.14). Only when the ECC correction was applied to both Ca^{2+} and acetate did the pair correlation function $g_{\mathrm{HsubHex}}(r)$ match the experimental result (Fig. 5.14).

This finding has important consequences for the modeling of interactions between Ca^{2+} and negatively charged amino acid residues. It indicates that, in order to correctly describe the strength of Ca^{2+} binding, the partial charges should be rescaled not only on Ca^{2+} but also on every charged amino acid residue. This is particularly relevant to future simulations of Ca^{2+} binding to EF hands of recoverin and other neuronal calcium sensors.

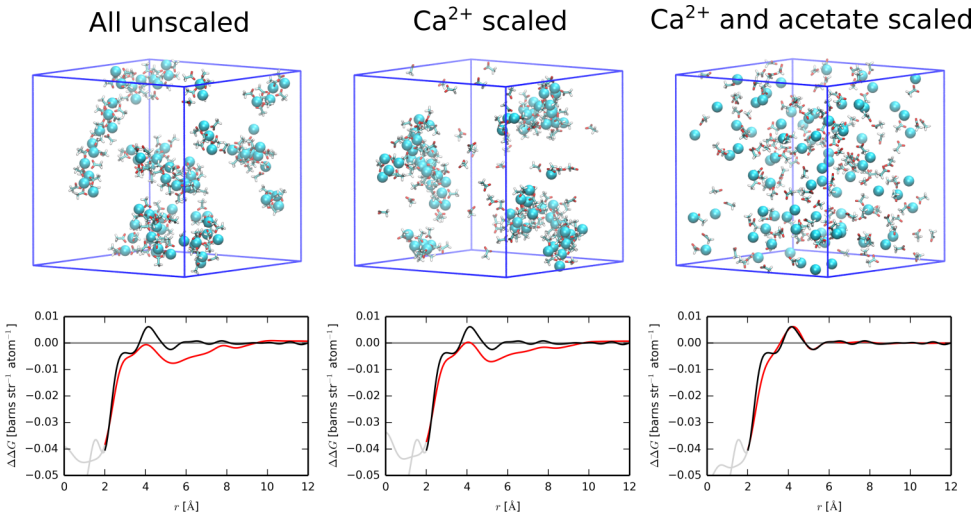

Figure 5.14: Scaling of charges on both Ca^{2+} and acetate is required to correctly reproduce structural data from neutron scattering measurements. Representative snapshots from MD trajectories of a 1 molal aqueous solution of calcium acetate **(top)** and a comparison of experimentally-measured second-order differences (black curves) with those calculated from MD (red curves) **(bottom)**.

Chapter 6

Further results

In the remaining part, we touch on two topics intrinsically connected with plasma membranes of (not only) mammalian cells: cholesterol and transmembrane voltage. We introduce simulations of cholesterol uptake by high-density lipoprotein (HDL) particles, described in paper III, as well as a comparison between two commonly used methods of modeling transmembrane voltage in MD simulations, being the subject of a detailed analysis in paper IV.

6.1 Cholesterol oxidation and HDL particles

Cholesterol is an essential constituent of mammalian plasma membranes, forming about 25–40 mol % of their lipid content (Ikonen, 2008). The presence of cholesterol modulates the fluidity and phase behavior of the plasma membrane, also making it more mechanically resistant and less permeable to small solutes (Róg et al., 2009). Moreover, cholesterol participates in the formation of lipid nanodomains (Simons and Sampaio, 2011) and regulates the function of numerous membrane proteins (Epand, 2006).

The amount of cholesterol in cells is regulated. Excess cholesterol is collected from plasma membranes by HDL particles, transporting it through bloodstream to the liver, where it is excreted or further metabolized. Mature HDL particles have about 9–11 nm in diameter and comprise an amphipathic phospholipid envelope surrounding a dense hydrophobic core which is rich in cholesteryl esters and triglycerides (Huang et al., 2011). The shape of the HDL particle is maintained by a cage-like structure formed by apolipoproteins, such as the apoA-I apolipoprotein. By removing cholesterol and other fats from macrophage cells in artery walls, HDL particles decrease accumulation of atherosclerosis, associated with the risk of cardiovascular disease (Rye et al., 2009).

Cholesterol is susceptible to oxidation, occurring *in vivo* via enzymatic reac-

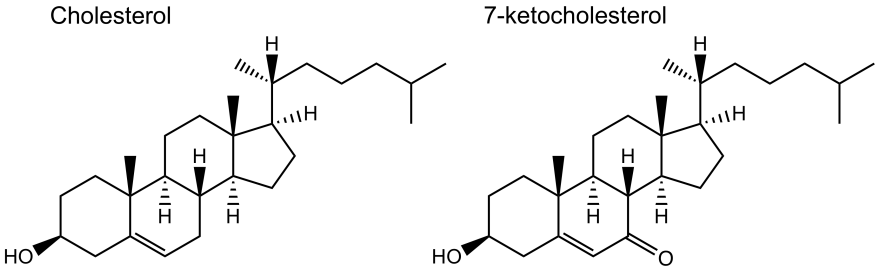

Figure 6.1: Sterols investigated in this study.

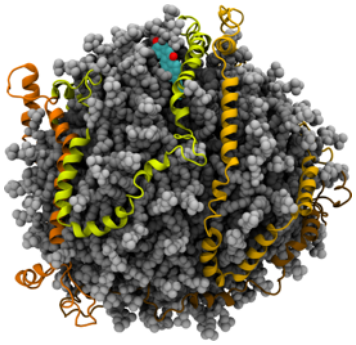

Figure 6.2: HDL particle simulated in this study.

tions or due to reactive oxygen species. Cholesterol oxidation affects the properties of lipid membranes and is linked to pathological conditions, such as chronic inflammation, cancer, or various neurodegenerative diseases (Kulig et al., 2015). Notably, increased levels of oxidized cholesterol are found in atherosclerotic plaques (Brown and W, 1999). In addition, products of cholesterol oxidation participate in cellular signaling (Schroepfer, 2000).

In paper III we investigated how cholesterol oxidation affects its uptake into HDL particles. For this purpose, we calculated free-energy profiles associated with the embedding of cholesterol and one of its commonly occurring oxidized analogs (7-ketocholesterol, see Fig. 6.1) into a model HDL particle. The HDL particle consisted of 133 POPC molecules, forming the surface phospholipid monolayer, 106 cholesteryl oleate molecules, comprising the hydrophobic core of the particle, and four apoA-I apolipoprotein chains in a twisted cage-like arrangement on the surface (see Fig. 6.2).

Initial umbrella sampling simulations along the center-of-mass distance from the center of the HDL particle revealed slow convergence of the free-energy profiles. Therefore, to accelerate sampling of orthogonal degrees of freedom and thus improve convergence, we employed the REUS method (see Section 2.8), coupling neighboring umbrella windows via random exchanges of geometries governed by the Metropolis criterion (2.26). To this end, we implemented the REUS algorithm in a customized version of the GROMACS 4.6.5 software (Hess et al., 2008).

For both cholesterol and 7-ketocholesterol, the use of the REUS method allowed us to achieve converged values of the free energy difference associated with moving the solute from water to the inside of the HDL particle. We found that these free-energy differences are similar irrespective of cholesterol oxidation, equaling -17 kcal mol^{-1} for cholesterol and -14 kcal mol^{-1} for 7-ketocholesterol. Moreover, we discovered that both unoxidized and oxidized cholesterol exhibit a preferential position in the phospholipid monolayer near the particle surface.

Our results indicate that cholesterol oxidation does not prevent its uptake into HDL particles. Therefore, if there is a difference between the efflux of cholesterol and 7-ketocholesterol from cells, it must be due to an additional selective mechanism. Moreover, our results suggest that since 7-ketocholesterol is preferentially located on the surface of the HDL particle, it can participate in signaling while carried by the HDL.

6.2 Modeling of transmembrane voltage

Most living cells maintain a difference in the electrostatic potential across their plasma membranes. This transmembrane voltage, ranging typically between -10 and -100 mV, arises mainly from differences in concentrations of ionic species such as K^+, Na^+, and Cl^- between the inside and the outside of a cell. Changes in the transmembrane voltage in neurons form the basis of brain activity, and transmembrane voltage also plays a role in the membrane transport of ions and various metabolites (Alberts et al., 2002).

An accurate representation of the transmembrane voltage is critical in MD simulations of diverse membrane-related molecules, such as voltage-gated ion channels (Delemotte et al., 2015) and fluorescent voltage indicators (Han et al., 2014), as well as in computational studies of membrane electroporation (Böckmann et al., 2008). Currently, two methods of transmembrane voltage modeling are used in MD simulations: the ion imbalance method (Sachs et al., 2004; Delemotte et al., 2008) and the constant electric field approach (Roux, 1997; Tieleman et al., 2001; Roux, 2008). The former method employs two disconnected compartments with different ion concentrations, giving rise to a voltage drop across a lipid bilayer placed in-between the two compartments. The latter method consists in applying a homogeneous external electric field parallel with the membrane normal to all charges of the system. While the former approach mimics more closely the actual situation in the cell, it has some practical disadvantages, such as the need for two separated bulk solutions and the inability to fine-tune the value of the transmembrane voltage in the size-limited *in-silico* system.

In paper IV, we conducted a benchmark study of the two methods of transmembrane voltage modeling to assess potential differences between them. The MD simulations used a double-bilayer setup, with two POPC bilayers being immersed in a NaCl or KCl salt solution. We monitored quantities such as the transmembrane potential, the electric field intensity, and the charge density across the simulation box. Furthermore, we examined effects of the transmembrane voltage on ionic densities as well as on the ordering of water and lipid head group dipoles. Overall, we found that, within the statistical error, the two methods yielded indistinguishable results in terms of all the observed quantities. This allowed us to conclude that both methods are equivalent, at least for systems containing the same monovalent ionic species on both sides of the membrane.

Chapter 7

Conclusion

This thesis deals with computational modeling of molecules associated with biological membranes. From the enormous variety of natural and synthetic molecular species binding to membranes of living cells, we chose to focus primarily on two categories of "sensor" molecules: membrane-embedded synthetic fluorescent probes and peripherally associated calcium-sensing proteins. By making use of the detailed spatial and temporal resolution provided by molecular simulations, we aimed at elucidating important characteristics of these molecules in the membrane environment. Such atomistic insights are essential for the development of new experimental approaches such as the 2PPM technique as well as for acquiring a detailed mechanistic understanding of physiological processes in living cells.

In the first part of this thesis, we presented MD simulations and TD-DFT calculations of membrane fluorescent probes performed in concert with fluorescence microscopy experiments. Our goal was to independently verify by computational means that FDLD measurements can provide accurate information on the orientational distributions of fluorescent molecules associated with membranes. Such a comparison between simulations and experiments was already the focus of our previous work (Timr, 2013; Timr et al., 2014), which, however, was limited to a single fluorescent probe and which used simplified assumptions on the behavior of the 2P absorption cross section. Here we extended the comparison to another structurally different fluorescent probe, and, importantly, we analyzed in detail the anisotropy of 2P absorption for ensembles of geometries sampled in MD trajectories. For both fluorescent probes, this analysis revealed a tendency of the 2P absorption cross section to exhibit a directional behavior, allowing for a simplified vectorial description using the TDM vector. The validity of this approximation was further supported by a good agreement between computationally-determined orientational distributions and the results of our analysis of FDLD data, which were measured on GUVs labeled with the two fluorescent probes. Altogether, our

results point to a broad applicability of the vectorial description of 2P absorption cross section, which leads to a simplified analysis of experimental data and allows for interpreting FDLD measurements in terms of molecular orientations. Thus, our findings make an important contribution toward turning the 2PPM technique into a tool of structural biology.

In the second part of this thesis, we investigated the mechanism of reversible membrane binding of recoverin, a protein which belongs to the family of neuronal calcium sensors and which possesses a calcium-induced myristoyl switch. Our MD simulations allowed us to observe the process of a spontaneous membrane insertion of the myristoyl moiety. This enabled us to confirm the role of the myristoyl group as a membrane anchor penetrating into the hydrophobic core of the membrane, as was suggested previously by measurements of membrane binding affinities and NMR order parameters. At the same time, the simulations pointed to an inherent tendency of the hydrophobic myristoyl moiety to minimize its exposure to the aqueous environment and to move back in-between hydrophobic side chains of recoverin. This indicates that even in the calcium-loaded open state of recoverin, the myristoyl anchor is not permanently available for membrane binding. We showed that the exposure of the myristoyl group and, therefore, also its ability to anchor recoverin to the membrane, is preconditioned by sufficient stability of the N-terminal domain. We propose that the stability of this domain may be enhanced by binding of rhodopsin kinase and/or possibly by the disordered C-terminal segment of recoverin, which may also transiently fill the binding site. Furthermore, we examined the role of electrostatics in the membrane binding of recoverin. We demonstrated that while the electrostatic interactions of positively charged protein residues with negatively charged lipids are alone not sufficient to keep recoverin stably attached to the membrane, they promote such orientations of the protein that are compatible with its physiological function.

Apart from the process of membrane binding and the subsequent orientation of recoverin on the membrane, we also examined the mechanism of calcium-induced myristoyl extrusion, preceding the membrane association. Previous NMR experiments revealed the existence of an intermediate state along the transition pathway from the closed myristoyl-sequestering state to the open myristoyl-exposing state. Moreover, the intermediate state was suggested to be the most likely target of calcium binding. To look into a possible conformation of this hidden intermediate state and to evaluate how the conformation is altered by calcium binding, we performed direct MD and REST2 simulations relying on the experimentally supported assumption that the intermediate state is structurally similar to the known structure of the E85Q recoverin mutant. Our results indicate that without

Ca^{2+}, the intermediate state exhibits a relatively broad range of conformations and domain orientations. Ca^{2+} binding to the EF hand 3 then stabilizes conformations similar to the structure of the E85Q mutant, which are expected to be more susceptible to binding of another Ca^{2+} to the EF hand 2, ultimately inducing myristoyl extrusion. We note that a full computational characterization of the calcium-induced myristoyl switch will require further extensive simulations and a careful evaluation of Ca^{2+} binding affinities for different conformations of recoverin along the transition path. To this end, we presented our results on the interaction between Ca^{2+} and carboxyl groups, with MD simulations benchmarked against neutron scattering experiments. We found that an accurate description of this interaction requires inclusion of electronic polarization effects via rescaling the charges on both Ca^{2+} and the carboxyl group in line with the ECC approach (Leontyev and Stuchebrukhov, 2011; Kohagen et al., 2014b, 2015).

In addition, our work contributed to clarifying the effect of cholesterol oxidation on its uptake into HDL particles. REUS simulations, the algorithm for which we implemented in a customized version of the GROMACS software, revealed that both cholesterol and the oxidized 7-ketocholesterol are readily absorbed by HDL particles and tend to be positioned near their surfaces, which may have implications for the participation of 7-ketocholesterol in signaling. Finally, we also contributed to a computational study comparing two common ways of representing transmembrane voltage in MD simulations: the ion imbalance method and the constant electric field method. We arrived at the conclusion that both methods provide essentially identical results in terms of all quantities analyzed in the study.

Taken together, the selected membrane-related topics investigated in this thesis illustrate the extraordinary diversity of molecules and processes which can be associated with biological membranes. Importantly, the work presented in this thesis demonstrates that classical MD simulations, potentially coupled with *ab initio* electronic structure calculations, have the ability to elucidate atomistic details of various membrane-related processes and that in this way simulations can also assist in the development of new experimental techniques.

Appendix A

Structural interpretation of FDLD data

To derive quantitative information on the orientations of membrane-bound fluorescent probes from measurement of the dichroic ratio (3.1), we employed a geometrical model presented in this appendix. This model assumes that the absorption anisotropy of the fluorescent probe can be described with a single vector (see Section 3.2), here denoted as $\boldsymbol{\mu}$. The local orientation of $\boldsymbol{\mu}$ with respect to the membrane surface is expressed in terms of two angles: the tilt angle α of $\boldsymbol{\mu}$ relative to the bilayer normal and the angle ρ, corresponding to the rotation of the $\boldsymbol{\mu}$ around the bilayer normal. The direction of the bilayer normal with respect to a reference coordinate system is given by angles θ and ϕ. The definition of the set of angles is illustrated in Figure A.1.

The direction of the vector $\boldsymbol{\mu}$ can be expressed in the reference coordinate system as

$$\boldsymbol{\mu}(\alpha, \rho, \theta, \phi) = \mathbf{R}_3\,(\theta)\,\mathbf{R}_2(-\phi)\,\mathbf{R}_1(\rho)\,\mathbf{R}_2(-\alpha)\begin{pmatrix}1\\0\\0\end{pmatrix} \tag{A.1}$$

where $\mathbf{R}_1(\tau)$, $\mathbf{R}_2(\tau)$, and $\mathbf{R}_3(\tau)$ are rotation matrices defined as

$$\mathbf{R}_1(\tau) = \begin{pmatrix}1 & 0 & 0\\ 0 & \cos\tau & -\sin\tau\\ 0 & \sin\tau & \cos\tau\end{pmatrix}, \quad \mathbf{R}_2(\tau) = \begin{pmatrix}\cos\tau & 0 & \sin\tau\\ 0 & 1 & 0\\ -\sin\tau & 0 & \cos\tau\end{pmatrix}, \tag{A.2}$$

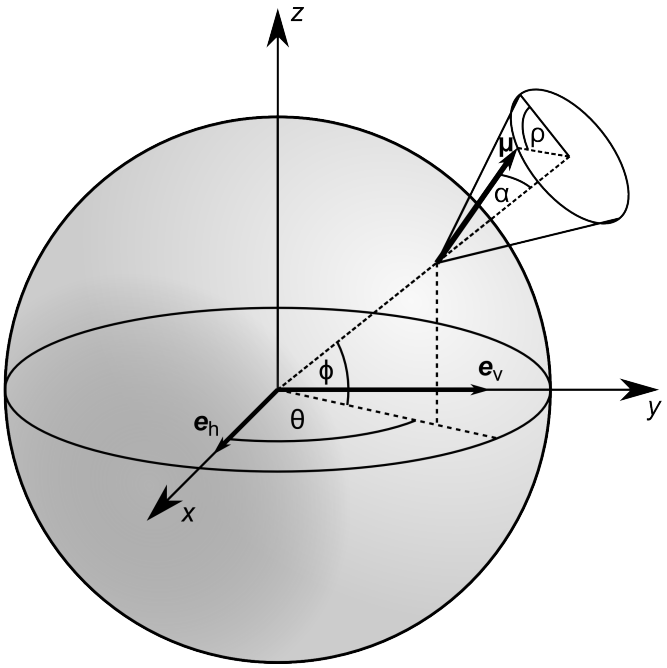

Figure A.1: Geometrical model of the TDM orientation of a fluorescent probe embedded in a membrane (Timr et al., 2014).

and

$$\mathbf{R}_3(\tau) = \begin{pmatrix} \cos\tau & -\sin\tau & 0 \\ \sin\tau & \cos\tau & 0 \\ 0 & 0 & 1 \end{pmatrix} \tag{A.3}$$

We assume that $\boldsymbol{\mu}$ adopts a whole range of the angles α, characterized by a distribution $F(\alpha)$ of the tilts relative to the membrane normal. At the same time, rotation around the membrane normal can be regarded as isotropic; therefore, we can integrate over ρ. Upon illumination with light linearly polarized in the direction $\boldsymbol{e}$, the expected fluorescence intensity in the case of 1P absorption is given by

$$I_{\mathbf{e}}^{1\mathrm{P}}(\theta,\phi) = \frac{I_0}{2\pi}\int_0^{2\pi} \mathrm{d}\rho \int_0^{\pi/2} \mathrm{d}\alpha\, F(\alpha)\,(\boldsymbol{\mu}(\alpha,\rho,\theta,\phi)\cdot\boldsymbol{e})^2 \tag{A.4}$$

In the case of 2P absorption, the predicted fluorescence intensity is equal to

$$I_{\mathbf{e}}^{2\mathrm{P}}(\theta,\phi) = \frac{I_0'}{2\pi}\int_0^{2\pi} \mathrm{d}\rho \int_0^{\pi/2} \mathrm{d}\alpha\, F(\alpha)\,(\boldsymbol{\mu}(\alpha,\rho,\theta,\phi)\cdot\boldsymbol{e})^4 \tag{A.5}$$

Since cells or GUVs are typically imaged with the focal plane of the objective set close to their equatorial planes, we can assume ϕ to be equal to zero, which greatly simplifies the resulting formulas.

Let us orient the reference coordinate system in such a way that the z axis

points in the direction of the excitation laser beam, while the x and y axes are aligned with the two directions of light polarization used for FDLD measurements. The x axis is identified with the polarization that appears horizontal in GUV images and the y axis with that appearing vertical. Furthermore, let $\langle g(\alpha)\rangle$ represent the expectation value of a function $g(\alpha)$,

$$\langle g(\alpha)\rangle = \int_0^{\pi/2} \mathrm{d}\alpha\, F(\alpha)\, g(\alpha) \tag{A.6}$$

By evaluating (A.4), we obtain formulas for the intensities of fluorescence excited with horizontally and vertically polarized light in the case of 1P absorption:

$$I_h^{1\mathrm{P}}(\theta) = I_0 \left(\langle \cos^2\alpha\rangle \cos^2\theta + \frac{1}{2}\langle \sin^2\alpha\rangle \sin^2\theta \right) \tag{A.7}$$

$$I_v^{1\mathrm{P}}(\theta) = I_0 \left(\langle \cos^2\alpha\rangle \sin^2\theta + \frac{1}{2}\langle \sin^2\alpha\rangle \cos^2\theta \right) \tag{A.8}$$

Similarly, for 2P absorption we obtain from (A.5):

$$I_h^{2\mathrm{P}}(\theta) = I_0' \left(\langle \cos^4\alpha\rangle \cos^4\theta + \frac{3}{16}\langle \sin^2 2\alpha\rangle \sin^2 2\theta + \frac{3}{8}\langle \sin^4\alpha\rangle \sin^4\theta \right) \tag{A.9}$$

$$I_v^{2\mathrm{P}}(\theta) = I_0' \left(\langle \cos^4\alpha\rangle \sin^4\theta + \frac{3}{16}\langle \sin^2 2\alpha\rangle \sin^2 2\theta + \frac{3}{8}\langle \sin^4\alpha\rangle \cos^4\theta \right) \tag{A.10}$$

The ratio of (A.7) and (A.8) and the ratio of (A.9) and (A.10) represent a prediction of the dichroic ratio r for 1P and 2P absorption, respectively, at a spot along the membrane where the bilayer normal is oriented at an angle θ relative to the horizontal polarization.

The formulas (A.7)–(A.10) contain only two independent parameters determining how the 1P or 2P dichroic ratio r depends on θ, namely, $\langle \cos^2\alpha\rangle$ and $\langle \cos^4\alpha\rangle$. The remaining expectation values in (A.7)–(A.10) can be written as a combination of these two parameters. The values of $\langle \cos^2\alpha\rangle$ and $\langle \cos^4\alpha\rangle$ can be obtained by fitting the experimentally-determined dependence of r on θ with a theoretical prediction based on (A.7)–(A.10). Thus, $\langle \cos^2\alpha\rangle$ and $\langle \cos^4\alpha\rangle$ present the actual information on the distribution function $F(\alpha)$ that can be obtained from a combination of 1P and 2P FDLD measurements.

The orientational distribution of α can be derived from the knowledge of the expectation values $\langle \cos^2\alpha\rangle$ and $\langle \cos^4\alpha\rangle$ providing that a functional form of the distribution function is assumed. The distribution function $F(\alpha)$ can be written as

$$F(\alpha) = \sin\alpha\, f(\alpha) \tag{A.11}$$

where the $\sin\alpha$ term reflects the changing density of states with changing α, and

$f(\alpha)$ is a function satisfying a normalization condition

$$1 = \int_0^{\pi/2} \mathrm{d}\alpha \, \sin\alpha \, f(\alpha) \tag{A.12}$$

In addition, we require that $f(\alpha) = f(\pi - \alpha)$ for all α in $(0, \pi)$ since it is not possible to distinguish between α and $\pi - \alpha$ on the basis of optical experiments.

The first approximation to the actual $f(\alpha)$ is a Gaussian function with a peak at α_0 and a width determined by σ, modified to comply with the symmetry condition:

$$f(\alpha) \approx f_{\mathrm{Gauss}}(\alpha) = A \left[\exp\left(-\frac{(\alpha - \alpha_0)^2}{2\sigma^2} \right) + \exp\left(-\frac{(\pi - \alpha - \alpha_0)^2}{2\sigma^2} \right) \right] \tag{A.13}$$

where A is a normalization factor.

Another approximation of $f(\alpha)$ relies on a truncated expansion of $f(\alpha)$ in the basis of Legendre polynomials. The function $f(\alpha)$ can be expanded on $(0, \pi)$ as (Castanho et al., 2003; Fraňová et al., 2010)

$$f(\alpha) = \sum_{L=0}^{\infty} \frac{1}{2}(2L+1)\langle P_L \rangle P_L(\cos\alpha) \tag{A.14}$$

where

$$\langle P_L \rangle = \int_0^{\pi} \mathrm{d}\alpha \, \sin\alpha \, f(\alpha) \, P_L(\cos\alpha) \tag{A.15}$$

Legendre polynomials are defined as (Reed and Simon, 1979)

$$P_L(x) = \frac{1}{L!} \left(\frac{\mathrm{d}}{\mathrm{d}t} \right)^L (1 - 2xt + t^2)^{-1/2} \Big|_{t=0} \tag{A.16}$$

and satisfy for all non-negative integers L and M (Reed and Simon, 1979)

$$\int_{-1}^{1} \mathrm{d}x \, P_L(x) \, P_M(x) = \frac{2}{2L+1} \delta_{LM} \tag{A.17}$$

As a consequence of the requirement that $f(\alpha) = f(\pi - \alpha)$ for all α in $(0, \pi)$, all terms with an odd L vanish from (A.14), and the integration domain can be restricted to $(0, \pi/2)$. After the restriction of the integration domain in (A.15) to $(0, \pi/2)$, i.e.,

$$\langle P_L \rangle = \int_0^{\pi/2} \mathrm{d}\alpha \, \sin\alpha \, f(\alpha) \, P_L(\cos\alpha) \tag{A.18}$$

(A.14) becomes

$$f(\alpha) = \sum_{L=0;\, L \text{ even}}^{\infty} (2L+1)\langle P_L \rangle P_L(\cos\alpha) \tag{A.19}$$

The first term in (A.19) is trivial since $P_0(\cos\alpha)$ is identically equal to 1, and $\langle P_0\rangle = 1$ because of the normalization condition (A.12). The second and the third term can be obtained from 1P and 2P FDLD measurements as $\langle P_2\rangle$ and $\langle P_4\rangle$ can be expressed using $\langle\cos^2\alpha\rangle$ and $\langle\cos^4\alpha\rangle$,

$$\langle P_2\rangle = \frac{1}{2}\left(3\langle\cos^2\alpha\rangle - 1\right) \tag{A.20}$$

$$\langle P_4\rangle = \frac{1}{8}\left(35\langle\cos^4\alpha\rangle - 30\langle\cos^2\alpha\rangle + 3\right) \tag{A.21}$$

Therefore, the combination of 1P and 2P LD experiments provides an estimate of the actual $f(\alpha)$ based on the first three terms of the Legendre expansion (A.19),

$$f(\alpha) \approx f_{\mathrm{Leg}}(\alpha) = 1 + 5\,\langle P_2\rangle\,P_2(\cos\alpha) + 9\,\langle P_4\rangle\,P_4(\cos\alpha) \tag{A.22}$$

Yet another approach (Castanho et al., 2003) searches $f(\alpha)$ as a function $f_S(\alpha)$ which maximizes the entropy functional

$$S(f_S(\alpha)) = \int_0^{\pi/2} \mathrm{d}\alpha\,\sin\alpha\,f_S(\alpha)\,\ln f_S(\alpha) \tag{A.23}$$

and, at the same time, satisfies the following constraints:

$$\langle P_2\rangle = \int_0^{\pi/2} \mathrm{d}\alpha\,\sin\alpha\,f_S(\alpha)\,P_2(\cos\alpha) \tag{A.24}$$

$$\langle P_4\rangle = \int_0^{\pi/2} \mathrm{d}\alpha\,\sin\alpha\,f_S(\alpha)\,P_4(\cos\alpha) \tag{A.25}$$

This problem can be solved by using the technique of Lagrange multipliers with a result

$$f_S(\alpha) = \frac{\exp(\lambda_2 P_2(\cos\alpha) + \lambda_4 P_4(\cos\alpha))}{\int_0^{\pi/2}\mathrm{d}\alpha\,\sin\alpha\,\exp(\lambda_2 P_2(\cos\alpha) + \lambda_4 P_4(\cos\alpha))} \tag{A.26}$$

Here, λ_2 and λ_4 are Lagrange multipliers associated with $\langle P_2\rangle$ and $\langle P_4\rangle$, respectively. They are calculated by substituting (A.26) into (A.24) and (A.25) and solving the resulting system of two nonlinear equations.

Finally, an estimate of the orientational distribution can be obtained from an expansion of the 2P-induced fluorescence intensity into a Fourier series, without calculating $\langle\cos^2\alpha\rangle$ and $\langle\cos^4\alpha\rangle$, as proposed by Ferrand et al. (2014):

$$I_h(\theta) \propto 1 + \frac{2S_2}{3}\cos[2(\theta-\varphi_2)] + \frac{S_4}{6}\cos[4(\theta-\varphi_4)] \tag{A.27}$$

The resulting four parameters S_2, S_4, φ_2, and φ_4 can be inserted into a formula

for the estimate of $f(\alpha)$:

$$f(\alpha) = A\left[1 + S_2\cos[2(\theta - \varphi_2)] + S_4\cos[4(\theta - \varphi_4)]\right] \tag{A.28}$$

where A is a normalization constant.

Appendix B

Structural data for recoverin

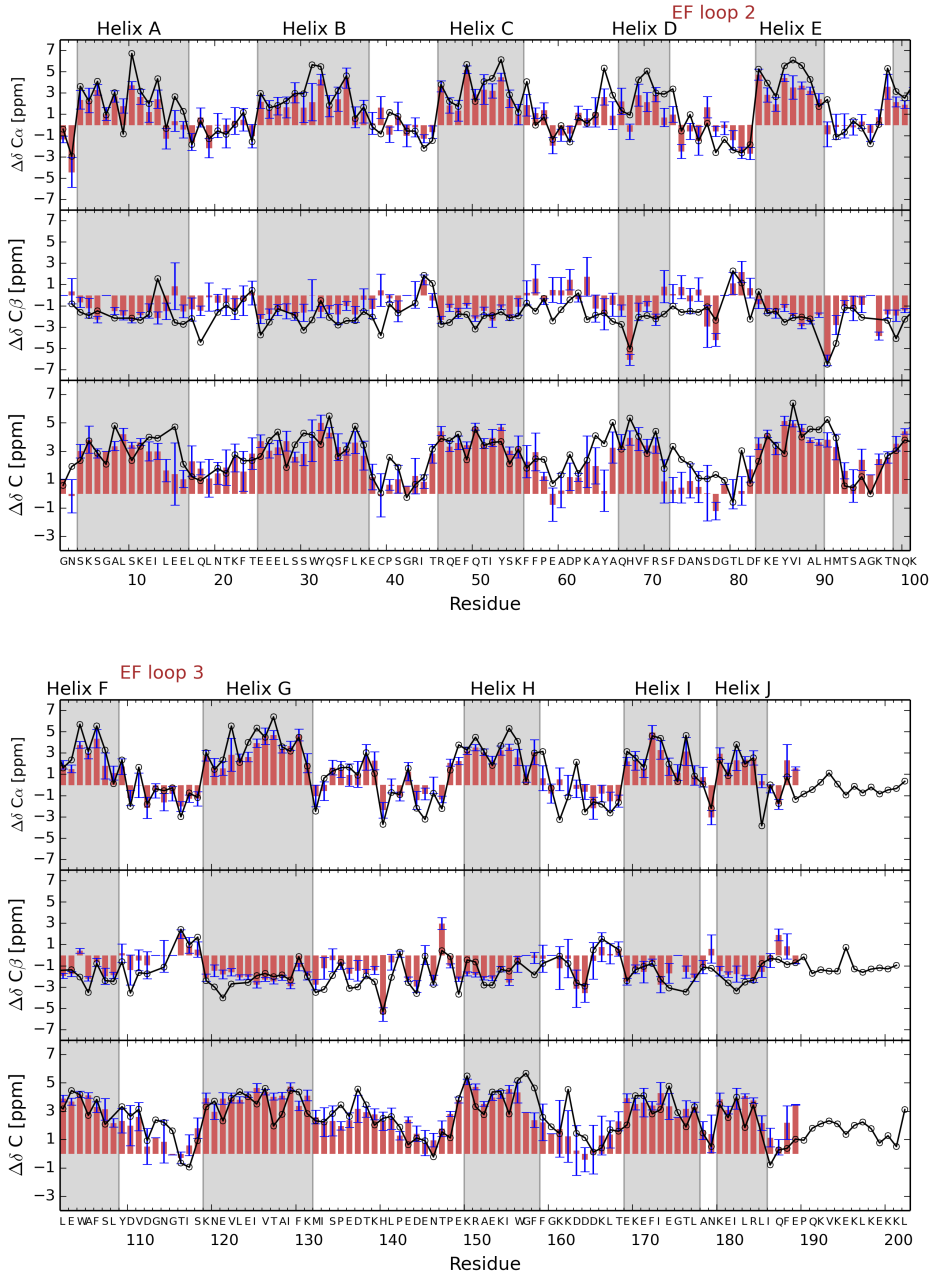

Figure B.1: Secondary chemical shifts of the Ca^{2+}-free closed state of recoverin: A comparison between the simulation and the experiment. The predicted values of Cα, Cβ, and C atom ^{13}C chemical shifts were calculated using the SHIFTX program (Neal et al., 2003) from 1000 snapshots extracted from a 1 µs trajectory. The experimental data come from (Tanaka et al., 1998). All chemical shifts are expressed relative to random coil chemical shifts calculated using an online script (Maltsev, 2017) for the amino acid sequence of recoverin at a temperature of 37 °C and at pH = 7.

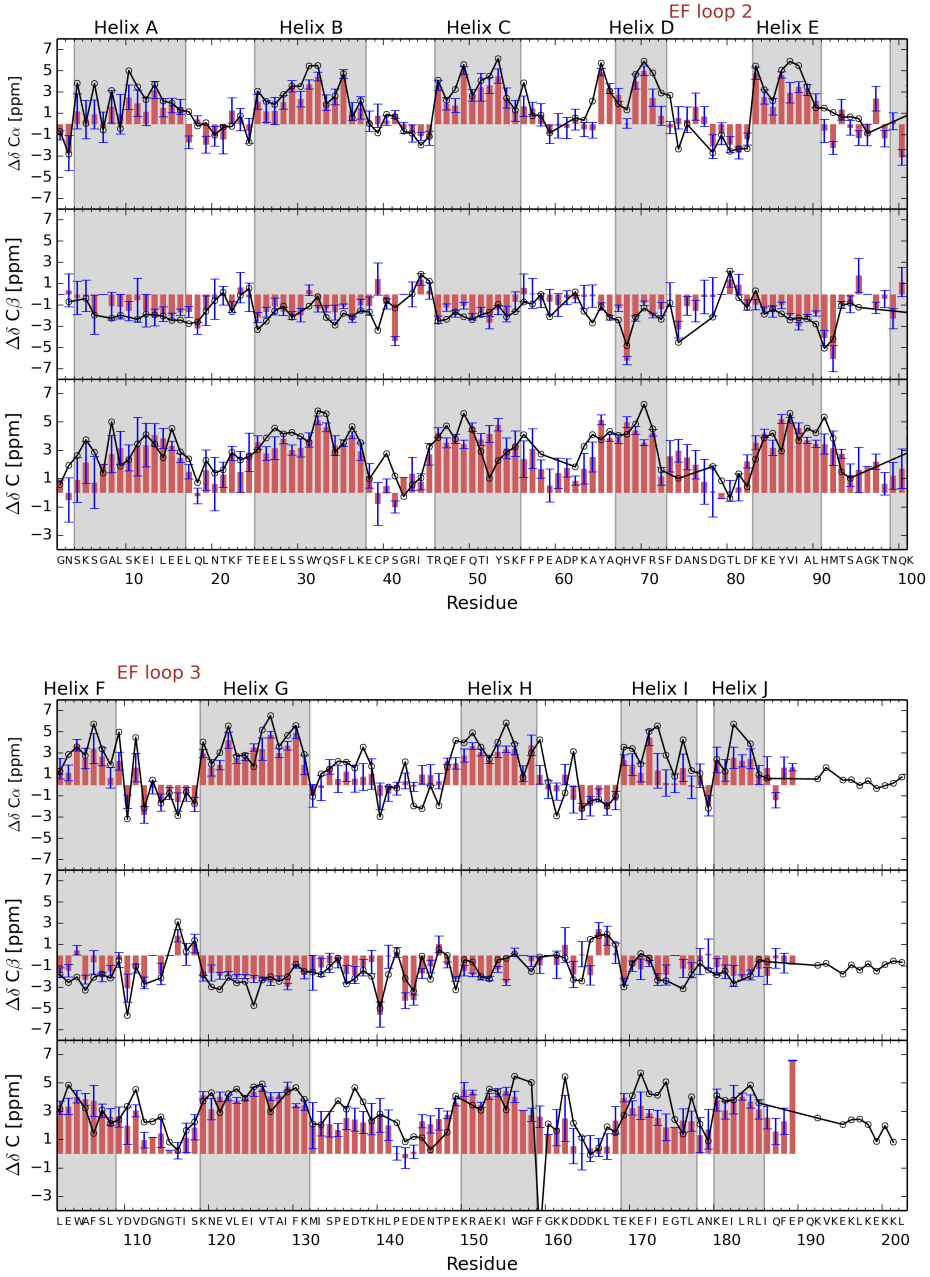

Figure B.2: Secondary chemical shifts of a semi-open state of recoverin binding a single Ca^{2+} ion: A comparison between the simulation and the experiment. The predicted values of Cα, Cβ, and C atom ^{13}C chemical shifts were calculated using the SHIFTX program (Neal et al., 2003) from 1000 snapshots extracted from a 1 µs trajectory (see Section 5.3). The experimental data were measured for the E85Q recoverin mutant (Ames et al., 2002). All chemical shifts are expressed relative to random coil chemical shifts calculated using an online script (Maltsev, 2017) for the amino acid sequence of recoverin at a temperature of 37 °C and at pH = 7.

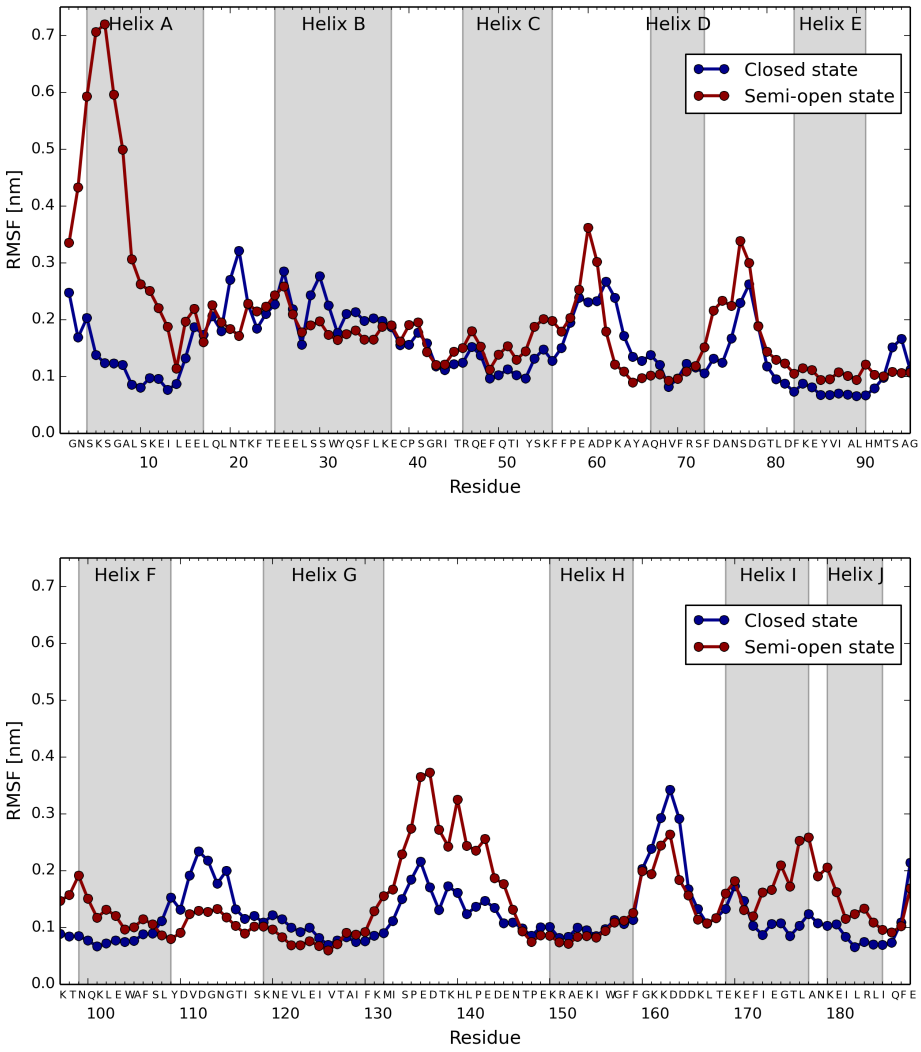

Figure B.3: A comparison of the Cα RMSF values calculated from a 1 µs trajectory of the closed Ca^{2+}-free state of recoverin and from a 1 µs trajectory of a semi-open state binding one Ca^{2+} ion (see Section 5.3). The initial 100 ns of each trajectory were not used for the analysis.

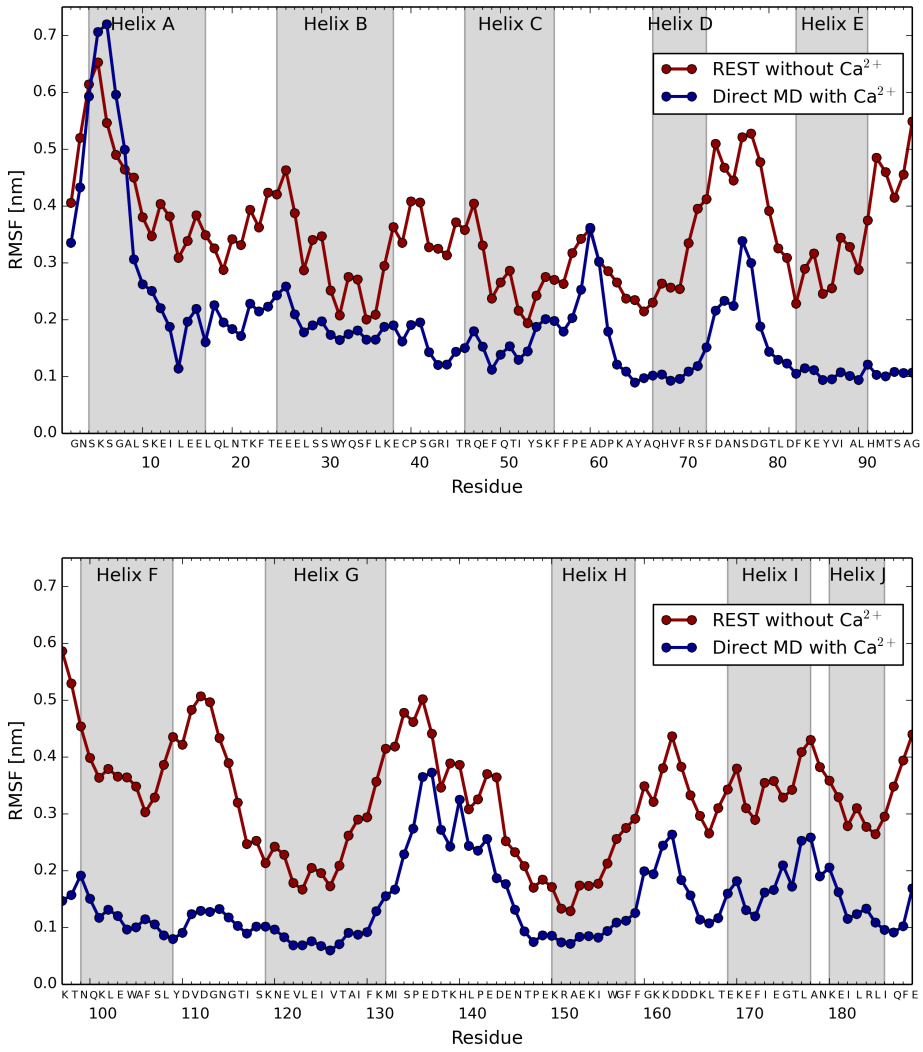

Figure B.4: A comparison of the Cα RMSF values calculated from a 1 µs trajectory of a semi-open state binding one Ca^{2+} ion and from a 560 ns REST2 simulation of a semi-open state without Ca^{2+} (see Sections 5.3 and 5.4). The initial 100 ns of each trajectory were not used for the analysis.

Bibliography

M. Abraham, D. van der Spoel, E. Lindahl, B. Hess, and the GROMACS development team. GROMACS user manual version 5.1.2, 2016. URL `www.gromacs.org`.

M. J. Abraham, T. Murtola, R. Schulz, S. Páll, J. C. Smith, B. Hess, and E. Lindahl. GROMACS: High performance molecular simulations through multi-level parallelism from laptops to supercomputers. *SoftwareX*, 1-2:19–25, 2015.

G. Adam and M. Delbruck. Reduction of dimensionality in biological diffusion processes. In A. Rich and N. Davidson, editors, *Structural chemistry and molecular biology*, pages 198–215. W. H. Freeman and Co, San Francisco, 1968.

K. Aidas, C. Angeli, K. L. Bak, V. Bakken, R. Bast, L. Boman, O. Christiansen, R. Cimiraglia, S. Coriani, P. Dahle, E. K. Dalskov, U. Ekström, T. Enevoldsen, J. J. Eriksen, P. Ettenhuber, B. Fernández, L. Ferrighi, H. Fliegl, L. Frediani, K. Hald, A. Halkier, C. Hättig, H. Heiberg, T. Helgaker, A. C. Hennum, H. Hettema, E. Hjertenæs, S. Høst, I.-M. Høyvik, M. F. Iozzi, B. Jansík, H. J. A. Jensen, D. Jonsson, P. Jørgensen, J. Kauczor, S. Kirpekar, T. Kjærgaard, W. Klopper, S. Knecht, R. Kobayashi, H. Koch, J. Kongsted, A. Krapp, K. Kristensen, A. Ligabue, O. B. Lutnæs, J. I. Melo, K. V. Mikkelsen, R. H. Myhre, C. Neiss, C. B. Nielsen, P. Norman, J. Olsen, J. M. H. Olsen, A. Osted, M. J. Packer, F. Pawlowski, T. B. Pedersen, P. F. Provasi, S. Reine, Z. Rinkevicius, T. A. Ruden, K. Ruud, V. V. Rybkin, P. Sałek, C. C. M. Samson, A. S. de Merás, T. Saue, S. P. A. Sauer, B. Schimmelpfennig, K. Sneskov, A. H. Steindal, K. O. Sylvester-Hvid, P. R. Taylor, A. M. Teale, E. I. Tellgren, D. P. Tew, A. J. Thorvaldsen, L. Thøgersen, O. Vahtras, M. A. Watson, D. J. D. Wilson, M. Ziolkowski, and H. Ågren. The Dalton quantum chemistry program system. *Wiley Interdisciplinary Reviews: Computational Molecular Science*, 4 (3):269–284, 2014.

B. Alberts, A. Johnson, J. Lewis, M. Raff, K. Roberts, and P. Walter. *Molecular Biology of the Cell*. Garland Science, New York, 4th edition, 2002.

B. J. Alder and T. E. Wainwright. Phase transition for a hard sphere system. *Journal of Chemical Physics*, 27:1208, 1957.

B. J. Alder and T. E. Wainwright. Studies in Molecular Dynamics. I. General Method. *Journal of Chemical Physics*, 31:459, 1959.

M. P. Allen and D. J. Tildesley. *Computer Simulation of Liquids*. Oxford science publications. Clarendon Press; Oxford University Press, Oxford, 1989.

J. B. Ames and S. Lim. Molecular structure and target recognition of neuronal calcium sensor proteins. *Biochimica et Biophysica Acta*, 1820(8):1205–1213, 2012.

J. B. Ames, T. Tanaka, M. Ikura, and L. Stryer. Nuclear magnetic resonance evidence for Ca^{2+}-induced extrusion of the myristoyl group of recoverin. *Journal of Biological Chemistry*, 270(52):30909–30913, 1995.

J. B. Ames, R. Ishima, and T. Tanaka. Molecular mechanics of calcium–myristoyl switches. *Nature*, 389(6647):198–202, 1997.

J. B. Ames, N. Hamasaki, and T. Molchanova. Structure and calcium-binding studies of a recoverin mutant (E85Q) in an allosteric intermediate state. *Biochemistry*, 41(18):5776–87, 2002.

J. B. Ames, K. Levay, J. N. Wingard, J. D. Lusin, and V. Z. Slepak. Structural basis for calcium-induced inhibition of rhodopsin kinase by recoverin. *Journal of Biological Chemistry*, 281(48):37237–37245, 2006.

C. Arnarez, J. J. Uusitalo, M. F. Masman, H. I. Ingólfsson, D. H. de Jong, M. N. Melo, X. Periole, A. H. de Vries, and S. J. Marrink. Dry Martini, a Coarse-Grained Force Field for Lipid Membrane Simulations with Implicit Solvent. *Journal of Chemical Theory and Computation*, 11(1):260–275, 2015.

D. Axelrod. Carbocyanine dye orientation in red-cell membrane studied by microscopic fluorescence polarization. *Biophysical Journal*, 26(3):557–573, 1979.

N. A. Baker, D. Sept, S. Joseph, M. J. Holst, and J. A. McCammon. Electrostatics of nanosystems: Application to microtubules and the ribosome. *Proceedings of the National Academy of Sciences, USA*, 98(18):10037–10041, 2001.

A. Baldwin and J. Ames. Core mutations that promote the calcium-induced allosteric transition of bovine recoverin. *Biochemistry*, 37(50):17408–17419, 1998.

A. Barducci, M. Bonomi, and M. Parrinello. Metadynamics. *Wiley Interdisciplinary Reviews: Computational Molecular Science*, 1(5):826–843, 2011.

M. Barros, F. Heinrich, S. A. K. Datta, A. Rein, I. Karageorgos, H. Nanda, and M. Lösche. Membrane Binding of HIV-1 Matrix Protein: Dependence on Bilayer Composition and Protein Lipidation. *Journal of Virology*, 90(9):4544–4555, 2016.

A. D. Becke. Density-functional thermochemistry. III. The role of exact exchange. *Journal of Chemical Physics*, 98(7):5648–5652, 1993.

R. K. P. Benninger, B. Onfelt, M. A. A. Neil, D. M. Davis, and P. M. W. French. Fluorescence imaging of two-photon linear dichroism: cholesterol depletion disrupts molecular orientation in cell membranes. *Biophysical Journal*, 88(1): 609–622, 2005.

H. Berendsen, J. Grigera, and T. Straatsma. The missing term in effective pair potentials. *Journal of Physical Chemistry*, 91(24):6269–6271, 1987.

H. J. C. Berendsen, J. P. M. Postma, W. F. van Gunsteren, and J. Hermans. *Interaction Models for Water in Relation to Protein Hydration*, pages 331–342. D. Reidel Publishing Company, Dordrecht, 1981.

H. J. C. Berendsen, J. P. M. Postma, W. F. van Gunsteren, A. Dinola, and J. R. Haak. Molecular dynamics with coupling to an external bath. *Journal of Chemical Physics*, 81(8):3684–3690, 1984.

O. Berger, O. Edholm, and F. Jahnig. Molecular dynamics simulations of a fluid bilayer of dipalmitoylphosphatidylcholine at full hydration, constant pressure, and constant temperature. *Biophysical Journal*, 72(5):2002–2013, 1997.

H. Berman, K. Henrick, and H. Nakamura. Announcing the worldwide Protein Data Bank. *Nature Structural Biology*, 10(12):980, 2003.

H. M. Berman, J. Westbrook, Z. Feng, G. Gilliland, T. Bhat, H. Weissig, I. Shindyalov, and P. Bourne. The Protein Data Bank. *Nucleic Acids Research*, 28:235–242, 2000.

R. A. Böckmann, B. L. de Groot, S. Kakorin, E. Neumann, and H. Grubmüller. Kinetics, Statistics, and Energetics of Lipid Membrane Electroporation Studied by Molecular Dynamics Simulations. *Biophysical Journal*, 95(4):1837–1850, 2008.

A. Bondar and J. Lazar. Dissociated Gα(GTP) and G$\beta\gamma$ Protein Subunits Are the Major Activated Form of Heterotrimeric Gi/o Proteins. *Journal of Biological Chemistry*, 289(3):1271–1281, 2014.

A. Botan, F. Favela-Rosales, P. F. J. Fuchs, M. Javanainen, M. Kanduc, W. Kulig, A. Lamber, C. Loison, A. Lyubartsev, M. S. Miettinen, L. Monticelli, J. Maatta, O. H. S. Ollila, M. Retegan, T. Rog, H. Santuz, and J. Tynkkynen. Toward Atomistic Resolution Structure of Phosphatidylcholine Headgroup and Glycerol Backbone at Different Ambient Conditions. *Journal of Physical Chemistry B*, 119(49):15075–15088, 2015.

R. W. Boyd. *Nonlinear Optics*. Academic Press, Amsterdam, 3rd edition, 2008.

S. Brasselet. Polarization-resolved nonlinear microscopy: application to structural molecular and biological imaging. *Advances in Optics and Photonics*, 3(3):205, 2011.

A. J. Brown and J. W. Oxysterols and atherosclerosis. *Atherosclerosis*, 142(1): 1–28, 1999.

R. D. Burgoyne. Neuronal calcium sensor proteins: generating diversity in neuronal Ca^{2+} signalling. *Nature Reviews: Neuroscience*, 8(3):182–193, 2007.

R. D. Burgoyne, D. W. O. Callaghan, B. Hasdemir, L. P. Haynes, and A. V. Tepikin. Neuronal Ca^{2+}-sensor proteins: multitalented regulators of neuronal function. *TRENDS in Neurosciences*, 27(4):203–209, 2004.

G. Bussi, D. Donadio, and M. Parrinello. Canonical sampling through velocity rescaling. *Journal of Chemical Physics*, 126(1):7, 2007.

P. Calvez, T. F. Schmidt, L. Cantin, K. Klinker, and C. Salesse. Phosphatidylserine allows observation of the calcium-myristoyl switch of recoverin and its preferential binding. *Journal of the American Chemical Society*, 138(41):13533–13540, 2016.

M. Cascella and S. Vanni. Toward accurate coarse-graining approaches for protein and membrane simulations. In *Chemical Modelling*, volume 12, pages 1–52. Royal Society of Chemistry, 2015.

M. Castanho, S. Lopes, and M. Fernandes. Using UV-Vis. linear dichroism to study the orientation of molecular probes and biomolecules in lipidic membranes. *Spectroscopy*, 17(2-3):377–398, 2003.

I. Chandrasekhar, M. Kastenholz, R. D. Lins, C. Oostenbrink, L. D. Schuler, D. P. Tieleman, and W. F. van Gunsteren. A consistent potential energy parameter set for lipids: dipalmitoylphosphatidylcholine as a benchmark of the GROMOS96 45A3 force field. *European Biophysics Journal with Biophysics Letters*, 32(1):67–77, 2003.

A. Czogalla, M. Grzybek, W. Jones, and U. Coskun. Validity and applicability of membrane model systems for studying interactions of peripheral membrane proteins with lipids. *Biochimica et Biophysica Acta-Molecular and Cell Biology of Lipids*, 1841(8):1049–1059, 2014.

T. Darden, D. York, and L. Pedersen. Particle mesh Ewald: an N.log(N) method for Ewald sums in large systems. *Journal of Chemical Physics*, 98(12):10089–10092, 1993.

L. Darré, M. R. Machado, A. F. Brandner, H. C. González, S. Ferreira, and S. Pantano. SIRAH: A structurally unbiased coarse-grained force field for proteins with aqueous solvation and long-range electrostatics. *Journal of Chemical Theory and Computation*, 11(2):723–739, 2015.

D. H. de Jong, G. Singh, W. F. D. Bennett, C. Arnarez, T. A. Wassenaar, L. V. Schäfer, X. Periole, D. P. Tieleman, and S. J. Marrink. Improved Parameters for the Martini Coarse-Grained Protein Force Field. *Journal of Chemical Theory and Computation*, 9(1):687–697, 2013.

L. Delemotte, F. Dehez, W. Treptow, and M. Tarek. Modeling membranes under a transmembrane potential. *Journal of Physical Chemistry B*, 112(18):5547–5550, 2008.

L. Delemotte, M. A. Kasimova, M. L. Klein, M. Tarek, and V. Carnevale. Free-energy landscape of ion-channel voltage-sensor–domain activation. *Proceedings of the National Academy of Sciences*, 112(1):124–129, 2015.

B. Desbat, C. Salesse, and P. Desmeules. Determination of the contribution of the myristoyl group and hydrophobic amino acids of recoverin on its dynamics of binding to lipid monolayers. *Biophysical Journal*, 93(6):2069–2082, 2007.

P. Desmeules, M. Grandbois, V. A. Bondarenko, A. Yamazaki, and C. Salesse. Measurement of membrane binding between recoverin, a calcium-myristoyl switch protein, and lipid bilayers by AFM-based force spectroscopy. *Biophysical Journal*, 82(6):3343–3350, 2002.

W. Dowhan and M. Bogdanov. Lipid-Dependent Membrane Protein Topogenesis. *Annual Review of Biochemistry*, 78:515–540, 2009.

M. Drobizhev, F. Q. Meng, A. Rebane, Y. Stepanenko, E. Nickel, and C. W. Spangler. Strong two-photon absorption in new asymmetrically substituted porphyrins: interference between charge-transfer and intermediate-resonance pathways. *Journal of Physical Chemistry B*, 110(20):9802–9814, 2006.

T. H. Dunning. Gaussian basis sets for use in correlated molecular calculations. I. The atoms boron through neon and hydrogen. *Journal of Chemical Physics*, 90(2):1007–1023, 1989.

R. M. Epand. Cholesterol and the interaction of proteins with membrane domains. *Progress in Lipid Research*, 45(4):279–294, 2006.

E. R. Farkas and W. W. Webb. Multiphoton polarization imaging of steady-state molecular order in ternary lipid vesicles for the purpose of lipid phase assignment. *Journal of Physical Chemistry B*, 114(47):15512–15522, 2010.

K. A. Feenstra, B. Hess, and H. J. C. Berendsen. Improving efficiency of large time-scale molecular dynamics simulations of hydrogen-rich systems. *Journal of Computational Chemistry*, 20(8):786–798, 1999.

P. Ferrand, P. Gasecka, A. Kress, X. Wang, F.-Z. Bioud, J. Duboisset, and S. Brasselet. Ultimate use of two-photon fluorescence microscopy to map orientational behavior of fluorophores. *Biophysical Journal*, 106(11), 2014.

A. J. Fliesler and R. E. Anderson. Chemistry and metabolism of lipids in the vertebrate retina. *Progress in Lipid Research*, 22(2):79–131, 1983.

M. Fraňová, J. Repáková, P. Čapková, J. M. Holopainen, and I. Vattulainen. Effects of DPH on DPPC-cholesterol membranes with varying concentrations of cholesterol: from local perturbations to limitations in fluorescence anisotropy experiments. *Journal of Physical Chemistry B*, 114(8):2704–2711, 2010.

L. Frediani, Z. Rinkevicius, and H. Agren. Two-photon absorption in solution by means of time-dependent density-functional theory and the polarizable continuum model. *Journal of Chemical Physics*, 122:244104, 2005.

D. Frenkel and B. Smith. *Understanding Molecular Simulations*. Academic Press, New York, 2nd edition, 2002.

M. J. Frisch, G. W. Trucks, H. B. Schlegel, G. E. Scuseria, M. A. Robb, J. R. Cheeseman, G. Scalmani, V. Barone, B. Mennucci, G. A. Petersson, H. Nakatsuji, M. Caricato, X. Li, H. P. Hratchian, A. F. Izmaylov, J. Bloino, G. Zheng, J. L. Sonnenberg, M. Hada, M. Ehara, K. Toyota, R. Fukuda, J. Hasegawa, M. Ishida, T. Nakajima, Y. Honda, O. Kitao, H. Nakai, T. Vreven, J. A. Montgomery, Jr., J. E. Peralta, F. Ogliaro, M. Bearpark, J. J. Heyd, E. Brothers, K. N. Kudin, V. N. Staroverov, R. Kobayashi, J. Normand, K. Raghavachari, A. Rendell, J. C. Burant, S. S. Iyengar, J. Tomasi, M. Cossi, N. Rega, J. M. Millam, M. Klene, J. E. Knox, J. B. Cross, V. Bakken, C. Adamo, J. Jaramillo, R. Gomperts, R. E. Stratmann, O. Yazyev, A. J. Austin, R. Cammi, C. Pomelli, J. W. Ochterski, R. L. Martin, K. Morokuma, V. G. Zakrzewski, G. A. Voth, P. Salvador, J. J. Dannenberg, S. Dapprich, A. D. Daniels, O. Farkas, J. B. Foresman, J. V. Ortiz, J. Cioslowski, and D. J. Fox. Gaussian 09, revision a.02, 2009.

Z. Han, L. Jin, F. Chen, J. J. Loturco, L. B. Cohen, A. Bondar, J. Lazar, and V. A. Pieribone. Mechanistic Studies of the Genetically Encoded Fluorescent Protein Voltage Probe ArcLight. *PLOS ONE*, 9(11):1–21, 2014.

B. Hess, H. Bekker, H. J. C. Berendsen, and J. Fraaije. LINCS: a linear constraint solver for molecular simulations. *Journal of Computational Chemistry*, 18(12): 1463–1472, 1997.

B. Hess, C. Kutzner, D. van der Spoel, and E. Lindahl. GROMACS 4: Algorithms for highly efficient, load-balanced, and scalable molecular simulation. *Journal of Chemical Theory and Computation*, 4(3):435–447, 2008.

R. W. Hockney, S. P. Goel, and J. W. Eastwood. Quiet high-resolution computer models of a plasma. *Journal of Computational Physics*, 14(2):148–158, 1974.

W. G. Hoover. Canonical dynamics: equilibrium phase-space distributions. *Physical Review A*, 31(3):1695–1697, 1985.

http://daltonprogram.org. DALTON, a molecular electronic structure program, release DALTON2013.2, 2013. URL `http://daltonprogram.org`.

K. Huang and A. E. Garcia. Acceleration of Lateral Equilibration in Mixed Lipid Bilayers Using Replica Exchange with Solute Tempering. *Journal of Chemical Theory and Computation*, 10(10):4264–4272, 2014.

R. Huang, R. A. G. D. Silva, W. G. Jerome, A. Kontush, M. J. Chapman, L. K. Curtiss, T. J. Hodges, and W. S. Davidson. Apolipoprotein A-I structural

organization in high-density lipoproteins isolated from human plasma. *Nature Structural & Molecular Biology*, 18(4):416–422, 2011.

W. Humphrey, A. Dalke, and K. Schulten. VMD: Visual molecular dynamics. *Journal of Molecular Graphics and Modelling*, 14(1):33–38, 1996.

E. Ikonen. Cellular cholesterol trafficking and compartmentalization. *Nature Reviews Molecular Cell Biology*, 9:125–138, 2008.

W. Im, M. Feig, and C. L. I. Brooks. An Implicit Membrane Generalized Born Theory for the Study of Structure, Stability, and Interactions of Membrane Proteins. *Biophysical Journal*, 85:2900–2918, 2003.

H. I. Ingolfsson, M. N. Melo, F. J. van Eerden, C. Arnarez, C. A. Lopez, T. A. Wassenaar, X. Periole, A. H. de Vries, D. P. Tieleman, and S. J. Marrink. Lipid organization of the plasma membrane. *Journal of the American Chemical Society*, 136(41):14554–14559, 2014.

H. I. Ingólfsson, C. A. Lopez, J. J. Uusitalo, D. H. de Jong, S. M. Gopal, X. Periole, and S. J. Marrink. The power of coarse graining in biomolecular simulations. *Wiley Interdisciplinary Reviews: Computational Molecular Science*, 4(3):225–248, 2014.

J. P. M. Jambeck and A. P. Lyubartsev. Derivation and systematic validation of a refined all-atom force field for phosphatidylcholine lipids. *Journal of Physical Chemistry B*, 116(10):3164–3179, 2012a.

J. P. M. Jambeck and A. P. Lyubartsev. An extension and further validation of an all-atomistic force field for biological membranes. *Journal of Chemical Theory and Computation*, 8(8):2938–2948, 2012b.

J. P. M. Jambeck and A. P. Lyubartsev. Another Piece of the Membrane Puzzle: Extending Slipids Further. *Journal of Chemical Theory and Computation*, 9 (1):774–784, 2013.

W. L. Jorgensen, J. Chandrasekhar, J. D. Madura, R. W. Impey, and M. L. Klein. Comparison of simple potential functions for simulating liquid water. *Journal of Chemical Physics*, 79(2):926–935, 1983.

I. Kabelka and R. Vacha. Optimal conditions for opening of membrane pore by amphiphilic peptides. *Journal of Chemical Physics*, 143:243115, 2016.

G. A. Kaminski and R. A. Friesner. Evaluation and reparametrization of the OPLS-AA force field for proteins via comparison with accurate quantum chemical calculations on peptides. *Journal of Physical Chemistry B*, 105(28):6474–6487, 2001.

A. Karotki. Simultaneous two-photon absorption of tetrapyrrolic molecules: from femtosecond coherence experiments to photodynamic therapy. Ph.D. thesis, Montana State University, Bozeman, Montana, 2003. URL `etd.lib.montana.edu/etd/2003/karotki/KarotkiA03.pdf`.

J. B. Klauda, R. M. Venable, J. A. Freites, J. W. O'Connor, D. J. Tobias, C. Mondragon-Ramirez, I. Vorobyov, A. D. MacKerell, and R. W. Pastor. Update of the CHARMM all-atom additive force field for lipids: Validation on six lipid types. *Journal of Physical Chemistry B*, 114(23):7830–7843, 2010.

M. Kohagen, M. Lepsik, and P. Jungwirth. Calcium binding to calmodulin by molecular dynamics with effective polarization. *Journal of Physical Chemistry Letters*, 5(22):3964–3969, 2014a.

M. Kohagen, P. E. Mason, and P. Jungwirth. Accurate description of calcium solvation in concentrated aqueous solutions. *Journal of Physical Chemistry B*, 118(28):7902–7909, 2014b.

M. Kohagen, E. Pluharova, P. E. Mason, and P. Jungwirth. Exploring ion-ion interactions in aqueous solutions by a combination of molecular dynamics and neutron scattering. *Journal of Physical Chemistry Letters*, 6(9):1563–1567, 2015.

A. Kress, P. Ferrand, H. Rigneault, T. Trombik, H.-T. He, D. Marguet, and S. Brasselet. Probing orientational behavior of MHC class I protein and lipid probes in cell membranes by fluorescence polarization-resolved imaging. *Biophysical Journal*, 101(2):468–76, 2011.

P. Krupa, A. K. Sieradzan, S. Rackovsky, M. Baranowski, S. Ołdziej, H. A. Scheraga, A. Liwo, and C. Czaplewski. Improvement of the treatment of loop structures in the UNRES force field by inclusion of coupling between backbone- and side-chain-local conformational states. *Journal of Chemical Theory and Computation*, 9(10):4620–4632, 2013.

W. Kulig, A. Olzynska, P. Jurkiewicz, A. M. Kantola, S. Komulainen, M. Manna, M. Pourmousa, M. Vazdar, L. Cwiklik, T. Rog, G. Khelashvili, D. Harries, V.-V. Telkki, M. Hof, I. Vattulainen, and P. Jungwirth. Cholesterol under oxidative

stress: How lipid membranes sense oxidation as cholesterol is being replaced by oxysterols. *Free Radical Biology and Medicine*, 84:30–41, 2015.

J. R. Lakowicz. *Principles of Fluorescence Spectroscopy*. Springer, New York, 3rd edition, 2006.

J. Lazar, A. Bondar, S. Timr, and S. J. Firestein. Two-photon polarization microscopy reveals protein structure and function. *Nature Methods*, 8(8):684–690, 2011.

I. Leontyev and A. Stuchebrukhov. Accounting for electronic polarization in non-polarizable force fields. *Physical Chemistry Chemical Physics*, 13(7):2613–2626, 2011.

K. Lindorff-Larsen, S. Piana, K. Palmo, P. Maragakis, J. L. Klepeis, R. O. Dror, and D. E. Shaw. Improved side-chain torsion potentials for the Amber ff99SB protein force field. *Proteins: Structure, Function & Bioinformatics*, 78(8):1950–1958, 2010.

P. Liu, B. Kim, R. Friesner, and B. J. Berne. Replica exchange with solute tempering: A method for sampling biological systems in explicit water. *Proceedings of the National Academy of Sciences of the United States of America*, 102(39): 13749–13754, 2005.

A. D. MacKerell, D. Bashford, M. Bellott, R. L. Dunbrack, J. D. Evanseck, M. J. Field, S. Fischer, J. Gao, H. Guo, S. Ha, D. Joseph-McCarthy, L. Kuchnir, K. Kuczera, F. T. K. Lau, C. Mattos, S. Michnick, T. Ngo, D. T. Nguyen, B. Prodhom, W. E. Reiher, B. Roux, M. Schlenkrich, J. C. Smith, R. Stote, J. Straub, M. Watanabe, J. Wiorkiewicz-Kuczera, D. Yin, and M. Karplus. All-atom empirical potential for molecular modeling and dynamics studies of proteins. *Journal of Physical Chemistry B*, 102(18):3586–3616, 1998.

A. D. MacKerell, M. Feig, and C. L. Brooks. Extending the treatment of backbone energetics in protein force fields: Limitations of gas-phase quantum mechanics in reproducing protein conformational distributions in molecular dynamics simulations. *Journal of Computational Chemistry*, 25(11):1400–1415, 2004.

A. Maltsev. Random coil chemical shifts for intrinsically disordered proteins, 2017. URL `http://www1.bio.ku.dk/english/research/bms/research/sbinlab/groups/mak/randomcoil/script/`.

A. E. Mark, S. P. van Helden, P. E. Smith, L. H. M. Janssen, and W. F. van Gunsteren. Convergence properties of free energy calculations: alpha-cyclodextrin

complexes as a case study. *Journal of American Chemical Society*, 116(14): 6293–6302, 1994.

P. R. L. Markwick and J. A. McCammon. Studying functional dynamics in biomolecules using accelerated molecular dynamics. *Physical Chemistry Chemical Physics*, 13(45):20053–65, 2011.

S. J. Marrink, H. J. Risselada, S. Yefimov, D. P. Tieleman, and A. H. de Vries. The MARTINI force field: coarse grained model for biomolecular simulations. *Journal of Physical Chemistry B*, 111(27):7812–7824, 2007.

S. Matsuda, O. Hisatomi, and F. Tokunaga. Role of Carboxyl-Terminal Charges on S-Modulin Membrane Affinity and Inhibition of Rhodopsin Phosphorylation. *Biochemistry*, 38(4):1310–1315, 1999.

S. McLaughlin. The electrostatic properties of membranes. *Annual Review of Biophysics and Biophysical Chemistry*, 18:113–136, 1989.

S. Miyamoto and P. A. Kollman. SETTLE: an analytical version of the SHAKE and RATTLE algorithm for rigid water models. *Journal of Computational Chemistry*, 13(8):952–962, 1992.

L. Monticelli, S. K. Kandasamy, X. Periole, R. G. Larson, D. P. Tieleman, and S.-J. Marrink. The MARTINI coarse-grained force field: Extension to proteins. *Journal of Chemical Theory and Computation*, 4(5):819–834, 2008.

M. Moradi and E. Tajkhorshid. Computational Recipe for Efficient Description of Large-Scale Conformational Changes in Biomolecular Systems. *Journal of Chemical Theory and Computation*, 10(7):2866–2880, 2014.

T. Mori, J. Jung, and Y. Sugita. Surface-tension replica-exchange molecular dynamics method for enhanced sampling of biological membrane systems. *Journal of Chemical Theory and Computation*, 9(12):5629–5640, 2013.

T. Mori, N. Miyashita, W. Im, M. Feig, and Y. Sugita. Molecular dynamics simulations of biological membranes and membrane proteins using enhanced conformational sampling algorithms. *Biochimica et Biophysica Acta - Biomembranes*, 1858:1635–1651, 2016.

D. Murray, N. Ben-Tal, B. Honig, and S. McLaughlin. Calculating total electrostatic energies with the nonlinear Poisson-Boltzmann equation. *Journal of Physical Chemistry*, 94:7684–7692, 1990.

D. Murray, N. Ben-Tal, B. Honig, and S. McLaughlin. Electrostatic interaction of myristoylated proteins with membranes: simple physics, complicated biology. *Structure*, 5:985–989, 1997.

D. Murray, A. Arbuzova, H. B., and M. S. The role of electrostatic and nonpolar interactions in the association of peripheral proteins with membranes. *Current Topics in Membranes*, 52:277–307, 2002.

W. K. Myers, X. Xu, C. Li, J. O. Lagerstedt, M. S. Budamagunta, J. C. Voss, R. D. Britt, and J. B. Ames. Double Electron-Electron Resonance Probes Ca^{2+}-Induced Conformational Changes and Dimerization of Recoverin. *Biochemistry*, 52:5800–5808, 2013.

H. Nanda, S. A. K. Datta, F. Heinrich, M. Lösche, A. Rein, S. Krueger, and J. E. Curtis. Electrostatic interactions and binding orientation of HIV-1 matrix studied by neutron reflectivity. *Biophysical Journal*, 99(8):2516–2524, 2010.

S. Neal, A. M. Nip, H. Zhang, and D. S. Wishart. Rapid and accurate calculation of protein 1H, 13C and 15N chemical shifts. *Journal of Biomolecular NMR*, 26 (3):215–240, 2003.

C. Neale, C. Madill, S. Rauscher, and R. Pomes. Accelerating Convergence in Molecular Dynamics Simulations of Solutes in Lipid Membranes by Conducting a Random Walk along the Bilayer Normal. *Journal of Chemical Theory and Computation*, 9(8):3686–3703, 2013.

G. W. Neilson, P. E. Mason, S. Ramos, and D. Sullivan. Neutron and X-ray scattering studies of hydration in aqueous solutions. *Philosophical Transactions of the Royal Society of London A: Mathematical, Physical and Engineering Sciences*, 359(1785):1575–1591, 2001.

W. G. Noid. Perspective: Coarse-grained models for biomolecular systems. *Journal of Chemical Physics*, 139(9):090901, 2013.

Y. Okamoto. Generalized-ensemble algorithms: Enhanced sampling techniques for Monte Carlo and molecular dynamics simulations. *Journal of Molecular Graphics and Modelling*, 22:425–439, 2004.

J. Olsen and P. Jorgensen. Linear and nonlinear response functions for an exact state and for an MCSCF state. *Journal of Chemical Physics*, 82(7):3235–3264, 1985.

Online Mendelian Inheritance in Man. 258100, accessed June 4, 2017. URL `https://omim.org/entry/258100`.

C. Oostenbrink, A. Villa, A. E. Mark, and W. F. Van Gunsteren. A biomolecular force field based on the free enthalpy of hydration and solvation: The GROMOS force-field parameter sets 53A5 and 53A6. *Journal of Computational Chemistry*, 25(13):1656–1676, 2004.

M. Orsi and J. W. Essex. The ELBA force field for coarse-grain modeling of lipid membranes. *PLoS ONE*, 6:e28637, 2011.

M. Parrinello and A. Rahman. Polymorphic transitions in single-crystals: a new molecular dynamics method. *Journal of Applied Physics*, 52(12):7182–7190, 1981.

R. M. Peitzsch and S. McLaughlin. Binding of acylated peptides and fatty acids to phospholipid vesicles: Pertinence to myristoylated proteins. *Biochemistry*, 32:10436–10443, 1993.

X. Periole, M. Cavalli, S.-J. Marrink, and M. A. Ceruso. Combining an elastic network with a coarse-grained molecular force field: Structure, dynamics, and intermolecular recognition. *Journal of Chemical Theory and Computation*, 5 (9):2531–2543, 2009.

S. Permyakov, A. Cherskaya, I. Senin, A. Zargarov, S. Shulga-Morskoy, A. Alekseev, D. Zinchenko, V. Lipkin, P. Philippov, V. Uversky, and E. Permyakov. Effects of mutations in the calcium-binding sites of recoverin on its calcium affinity: evidence for successive filling of the calcium binding sites. *Protein Engineering*, 13(11):783–790, 2000.

G. Petersson and M. Allaham. A complete basis set model chemistry. II. open-shell systems and the total energies of the 1st-row atoms. *Journal of Chemical Physics*, 94(9):6081–6090, 1991.

D. C. Rapaport. *The Art of Molecular Dynamics Simulation*. Cambridge University Press, Cambridge, 2nd edition, 2004.

RCSB PDB Database. URL `www.rcsb.org`.

M. Reed and B. Simon. *Methods of Modern Mathematical Physics III: Scattering Theory*, pages 149–151. Academic Press, San Diego, 1st edition, 1979.

P. Ren, J. Chun, D. G. Thomas, M. J. Schnieders, M. Marucho, J. Zhang, and N. A. Baker. Biomolecular electrostatics and solvation: a computational perspective. *Quarterly Reviews of Biophysics*, 45(04):427–491, 2012.

M. D. Resh. Fatty acylation of proteins: new insights into membrane targeting of myristylated and palmitoylated proteins. *Biochimica et Biophysica Acta*, 1451: 1–16, 1999.

M. D. Resh. Trafficking and signaling by fatty-acylated and prenylated proteins. *Nature Chemical Biology*, 2:584–590, 2006.

B. Roux. The calculation of the potential of mean force using computer simulations. *Computer Physics Communications*, 91(1-3):275–282, 1995.

B. Roux. Influence of the Membrane Potential on the Free Energy of an Intrinsic Protein. *Biophysical Journal*, 73(11):2980–2989, 1997.

B. Roux. The Membrane Potential and its Representation by a Constant Electric Field in Computer Simulations. *Biophysical Journal*, 95(9):4205–4216, 2008.

K.-A. Rye, C. A. Bursill, G. Lambert, F. Tabet, and P. J. Barter. The metabolism and anti-atherogenic properties of HDL. *Journal of Lipid Research*, 50:S195–S200, 2009.

T. Róg, M. Pasenkiewicz-Gierula, I. Vattulainen, and M. Karttunen. Ordering effects of cholesterol and its analogues. *Biochimica et Biophysica Acta (BBA) - Biomembranes*, 1788(1):97–121, 2009.

J. N. Sachs, P. S. Crozier, and T. B. Woolf. Atomistic simulations of biologically realistic transmembrane potential gradients. *Journal of Chemical Physics*, 121 (22):10847–51, 2004.

P. Salek, O. Vahtras, J. D. Guo, Y. Luo, T. Helgaker, and H. Agren. Calculations of two-photon absorption cross sections by means of density-functional theory. *Chemical Physics Letters*, 374(5-6):446–452, 2003.

M. Schmick and P. I. H. Bastiaens. The interdependence of membrane shape and cellular signal processing. *Cell*, 156:1132–1138, 2014.

G. Schroepfer. Oxysterols: Modulators of cholesterol metabolism and other processes. *Physiological Reviews*, 80(1):361–554, 2000.

J. P. Schrum, T. F. Zhu, and S. J. W. The origins of cellular life. *Cold Spring Harbor Perspectives in Biology*, 2:a002212, 2010.

I. I. Senin, V. A. Churumova, P. P. Philippov, and K.-W. Koch. Membrane binding of the neuronal calcium sensor recoverin – modulatory role of the charged carboxy-terminus. *BMC Biochemistry*, 8(24), 2007.

W. Shinoda, R. DeVane, and M. L. Klein. Zwitterionic lipid assemblies: Molecular dynamics studies of monolayers, bilayers, and vesicles using a new coarse grain force field. *Journal of Physical Chemistry B*, 114:6836–6849, 2010.

C. T. Sigal, W. Zhou, C. A. Buser, S. McLaughlin, and M. D. Resh. Amino-terminal basic residues of Src mediate membrane binding through electrostatic interaction with acidic phospholipids. *Proceedings of the National Academy of Sciences*, 91(25):12253–12257, 1994.

K. Simons and J. L. Sampaio. Membrane organization and lipid rafts. *Cold Spring Harbor Perspectives in Biology*, 3(10):a004697, 2011.

S. J. Singer and G. L. Nicolson. Fluid mosaic model of structure of cell-membranes. *Science*, 175(4023):720–731, 1972.

U. C. Singh and P. A. Kollman. An approach to computing electrostatic charges for molecules. *Journal of Computational Chemistry*, 5(2):129–145, 1984.

A. Srivastava and G. A. Voth. Hybrid approach for highly coarse-grained lipid bilayer models. *Journal of Chemical Theory and Computation*, 9(1):750–765, 2013.

A. Srivastava and G. A. Voth. Solvent-free, highly coarse-grained models for charged lipid systems. *Journal of Chemical Theory and Computation*, 10(10): 4730–4744, 2014.

A. H. Steindal, J. M. H. Olsen, K. Ruud, L. Frediani, and J. Kongsted. A combined quantum mechanics/molecular mechanics study of the one- and two-photon absorption in the green fluorescent protein. *Physical Chemistry Chemical Physics*, 14(16):5440–51, 2012.

F. Sterpone, S. Melchionna, P. Tuffery, S. Pasquali, N. Mousseau, T. Cragnolini, Y. Chebaro, J.-F. St-Pierre, M. Kalimeri, A. Barducci, Y. Laurin, A. Tek, M. Baaden, P. H. Nguyen, and P. Derreumaux. The OPEP protein model: from single molecules, amyloid formation, crowding and hydrodynamics to DNA/RNA systems. *Chemical Society Reviews*, 43(13):4871–4893, 2014.

W. Stillwell. *An Introduction to Biological Membranes*. Elsevier Science, New York, 2nd edition, 2016.

G. Stirnemann and F. Sterpone. Recovering protein thermal stability using all-atom Hamiltonian replica-exchange simulations in explicit solvent. *Journal of Chemical Theory and Computation*, 11(12):5573–5577, 2015.

M. B. Stone, S. A. Shelby, and S. L. Veatch. Super-resolution microscopy: Shedding light on the cellular plasma membrane. *Chemical Reviews*, 2017. doi: 10.1021/acs.chemrev.6b00716.

Y. Sugita and Y. Okamoto. Replica-exchange molecular dynamics method for protein folding. *Chemical Physics Letters*, 314(1):141–151, 1999.

Y. Sugita, A. Kitao, and Y. Okamoto. Multidimensional replica-exchange method for free-energy calculations. *Journal of Chemical Physics*, 113(15):6042, 2000.

T. Tanaka, J. B. Ames, T. S. Harvey, L. Stryer, and M. Ikura. Sequestration of the membrane-targeting myristoyl group of recoverin in the calcium-free state. *Nature*, 376(6539):444–447, 1995.

T. Tanaka, J. B. Ames, M. Kainosho, L. Stryer, and M. Ikura. Differential isotype labeling strategy for determining the structure of myristoylated recoverin by NMR spectroscopy. *Journal of Biomolecular NMR*, 11(2):135–152, 1998.

D. P. Tieleman, H. J. C. Berendsen, and M. S. P. Sansom. Voltage-Dependent Insertion of Alamethicin at Phospholipid/Water and Octane/Water Interfaces. *Biophysical Journal*, 80(1):331–346, 2001.

S. Timr. Simulation of processes in cellular membranes. M.Sc. thesis, Charles University in Prague, 2013. URL `https://is.cuni.cz/webapps/zzp/detail/113685/`.

S. Timr, A. Bondar, L. Cwiklik, M. Stefl, M. Vazdar, J. Lazar, and P. Jungwirth. Accurate determination of the orientational distribution of a fluorescent molecule in a phospholipid membrane. *Journal of Physical Chemistry B*, 118: 855–863, 2014.

G. A. Tribello, M. Bonomi, D. Branduardi, C. Camilloni, and G. Bussi. PLUMED 2: New feathers for an old bird. *Computer Physics Communications*, 185(2): 604–613, 2014.

K. G. Valentine, M. F. Mesleh, S. J. Opella, M. Ikura, and J. B. Ames. Structure, topology, and dynamics of myristoylated recoverin bound to phospholipid bilayers. *Biochemistry*, 42(21):6333–6340, 2003.

A. R. van Buuren, S. J. Marrink, and H. J. C. Berendsen. A molecular dynamics study of the decane water interface. *Journal of Physical Chemistry*, 97(36): 9206–9212, 1993.

W. F. van Gunsteren and H. J. C. Berendsen. *GROMOS-87 Manual*. Biomos BV, Nijenborgh 4, 9747 AG Groningen, The Netherlands, 1987.

L. Verlet. Computer experiments on classical fluids. I. Thermodynamical properties of Lennard-Jones molecules. *Physical Review*, 159(1):98–103, 1967.

J. Wang, P. Cieplak, and P. Kollman. How well does a restrained electrostatic potential (RESP) model perform in calculating conformational energies of organic and biological molecules? *Journal of Computational Chemistry*, 21(12): 1049–1074, 2000.

L. Wang, R. A. Friesner, and B. J. Berne. Replica exchange with solute scaling: A more efficient version of replica exchange with solute tempering (REST). *Journal of Physical Chemistry B*, 115(30):9431–9438, 2011.

T. A. Wassenaar, K. Pluhackova, R. A. Böckmann, S. J. Marrink, and D. P. Tieleman. Going backward: A flexible geometric approach to reverse transformation from coarse grained to atomistic models. *Journal of Chemical Theory and Computation*, 10(2):676–690, 2014.

O. H. Weiergraber, I. I. Senin, P. P. Philippov, J. Granzin, and K. W. Koch. Impact of N-terminal myristoylation on the Ca^{2+}-dependent conformational transition in recoverin. *Journal of Biological Chemistry*, 278(25):22972–22979, 2003.

O. H. Weiergraber, I. I. Senin, E. Y. Zernii, V. A. Churumova, N. A. Kovaleva, A. A. Nazipova, S. E. Permyakov, E. A. Permyakov, P. P. Philippov, J. Granzin, and K. W. Koch. Tuning of a neuronal calcium sensor. *Journal of Biological Chemistry*, 281(49):37594–37602, 2006.

G. Wu and W. L. Hubbell. Phospholipid asymmetry and transmembrane diffusion in photoreceptor disc membranes. *Biochemistry*, 32(3):879–888, 1993.

X. Xu, R. Ishima, and J. B. Ames. Conformational dynamics of recoverin's Ca^{2+}-myristoyl switch probed by ^{15}N NMR relaxation dispersion and chemical shift analysis. *Proteins*, 79:1910–1922, 2011.

T. Yanai, D. P. Tew, and N. C. Handy. A new hybrid exchange-correlation functional using the Coulomb-attenuating method (CAM-B3LYP). *Chemical Physics Letters*, 393(1-3):51–57, 2004.

S. O. Yesylevskyy, L. V. Schäfer, D. Sengupta, and S. J. Marrink. Polarizable water model for the coarse-grained MARTINI force field. *PLOS Computational Biology*, 6:1–17, 6 2010.

J. Zhou, I. F. Thorpe, S. Izvekov, and G. A. Voth. Coarse-grained peptide modeling using a systematic multiscale approach. *Biophysical Journal*, 92(12): 4289–4303, 2007.

List of Figures

List of Tables

List of Abbreviations

1P	one-photon
2P	two-photon
2PPM	two-photon polarization microscopy
AFM	atomic-force microscopy
DOPC	di-oleoylphosphatidylcholine
DOPG	di-oleoylphoshatidylglycerol
ECC	electronic continuum correction
EPR	electron paramagnetic resonance
GUV	giant unilamellar vesicle
H-REMD	Hamiltonian replica-exchange molecular dynamics
HDL	high-density lipoprotein
MD	molecular dynamics
NCS	neuronal calcium sensors (protein family)
NMR	nuclear magnetic resonance
NpT	isothermal–isobaric ensemble
NVT	isothermal ensemble
POPC	1-palmitoyl-2-oleoylphosphatidylcholine
QM	quantum mechanics
REMD	replica-exchange molecular dynamics
REST	replica exchange with solute tempering

REST2	replica exchange with solute tempering (updated version)
REUS	replica-exchange umbrella sampling
RMSD	root-mean-square deviation
RMSF	root-mean-square fluctuation
T-REMD	temperature replica-exchange molecular dynamics
TDM	transition dipole moment
WHAM	weighted histogram analysis method

List of Attached Papers

I S. Timr, J. Brabec, A. Bondar, T. Ryba, M. Zelezny, J. Lazar, and P. Jungwirth. Nonlinear Optical Properties of Fluorescent Dyes Allow for Accurate Determination of Their Molecular Orientations in Phospholipid Membranes. *Journal of Physical Chemistry B*, 119(30):9706-9716, 2015.

II S. Timr, R. Pleskot, J. Kadlec, M. Kohagen, A. Magarkar, and P. Jungwirth. Membrane Binding of Recoverin: From Mechanistic Understanding to Biological Functionality. *ACS Central Science*, submitted.

III T. Karilainen, S. Timr, I. Vattulainen, and P. Jungwirth. Oxidation of Cholesterol Does Not Alter Significantly Its Uptake into High-Density Lipoprotein Particles. *Journal of Physical Chemistry B*, 119(13):4594-4600, 2015.

IV J. Melcr, D. Bonhenry, S. Timr, and P. Jungwirth. Transmembrane Potential Modeling: Comparison between Methods of Constant Electric Field and Ion Imbalance. *Journal of Chemical Theory and Computation*, 12(5):2418-2425, 2016.